[redacted] N-62 60332 Copy 249

RM A50A03

NACA RM A50A03

RESEARCH MEMORANDUM

WIND-TUNNEL TESTS OF A 0.16-SCALE MODEL OF THE X-3 AIRPLANE AT HIGH SUBSONIC SPEEDS. - STABILITY AND CONTROL CHARACTERISTICS

By William T. Hamilton and Joseph W. Cleary

Ames Aeronautical Laboratory
Moffett Field, Calif.,

NATIONAL ADVISORY COMMITTEE FOR AERONAUTICS

WASHINGTON

April 21, 1950
Reclassified July 19, 1951

[redacted]

 [redacted]

NATIONAL ADVISORY COMMITTEE FOR AERONAUTICS

RESEARCH MEMORANDUM

WIND-TUNNEL TESTS OF A 0.16-SCALE MODEL OF THE X-3 AIRPLANE AT HIGH SUBSONIC SPEEDS. - STABILITY AND CONTROL CHARACTERISTICS

By William T. Hamilton and Joseph W. Cleary

SUMMARY

Static lateral- and longitudinal-stability tests were made of a 0.16-scale model of a projected, low-aspect-ratio, supersonic airplane at low and high subsonic Mach numbers. The wing of the model was equipped with leading-edge flaps and employed a modified double-wedge airfoil with sharp leading and trailing edges. An all-movable tail provided longitudinal control.

The results of the tests show a gradual increase in lift-curve slope for Mach numbers up to 0.925 and indicate no large decreases in the stalling lift coefficient throughout the Mach number range of the tests. Deflecting the leading-edge flaps increased the lift coefficient at the stall and at the lower Mach numbers improved the drag characteristics. Although a slight increase in drag coefficient occurred at a Mach number of 0.925, the Mach number for drag divergence was not reached within the Mach number range of the test.

The fins, which were intended to stabilize the fuselage nose when jettisoned for pilot escape, reduced the model stability to such an extent that their use was considered impractical. Without the nose fins, the static longitudinal stability was satisfactory and the most forward position of the neutral point was at approximately 19 percent of the mean aerodynamic chord at a Mach number of 0.80. The effectiveness of the tail for providing control was retained to a Mach number of 0.925.

Without the nose fins, the directional stability of the model was considered high although not excessive for Mach numbers of the test.

INTRODUCTION

This report presents the results of high-speed wind-tunnel tests of a 0.16-scale model of the projected X-3 (Air Force project MX-656)

[redacted]

airplane. This airplane has a low-aspect-ratio wing and tail with sharp leading and trailing edges and is designed for supersonic speeds.

The tests were conducted at the request of the U. S. Air Force to investigate the lateral- and longitudinal-stability and control characteristics in the low and high subsonic speed ranges, and were made in the Ames 16-foot high-speed wind tunnel.

During the tests, undesirable changes in the longitudinal stability near the stall were noted. Consequently, the testing was terminated and the model was transferred to one of the Ames 7- by 10-foot wind tunnels where the stability problem could be studied more economically.

COEFFICIENTS AND SYMBOLS

Pitching moments, yawing moments, and rolling moments were computed with respect to mutually perpendicular axes that passed through the center of gravity of the model. One axis coincided with the fuselage reference line while another was parallel to the wing 75-percent-chord line. The center of gravity was assumed to lie on the fuselage reference line and above the 15-percent point of the wing mean aerodynamic chord.

The horizontal-tail hinge moments were computed with respect to a lateral axis passing through the 25-percent point of the mean aerodynamic chord of the exposed tail.

The coefficients and symbols used in this report are defined as follows:

C_D drag coefficient $\left(\frac{\text{drag}}{qS}\right)$

C_{h_t} horizontal-tail hinge-moment coefficient $\left(\frac{\text{horizontal-tail hinge moment}}{qS_{t_e}\bar{c}_t}\right)$

C_L lift coefficient $\left(\frac{\text{lift}}{qS}\right)$

C_{L_t} tail lift coefficient $\left(\frac{\text{tail lift}}{qS_t}\right)$

C_m pitching-moment coefficient $\left(\frac{\text{pitching moment}}{qS\bar{c}}\right)$

ΔC_c increment of cross-wind-force coefficient $\left(\frac{\text{increment of cross-wind force}}{qS}\right)$

ΔC_D increment of drag coefficient $\left(\frac{\text{increment of drag}}{qS}\right)$

ΔC_L increment of lift coefficient $\left(\frac{\text{increment of lift}}{qS}\right)$

ΔC_l increment of rolling-moment coefficient $\left(\frac{\text{increment of rolling moment}}{qSb}\right)$

ΔC_m increment of pitching-moment coefficient $\left(\frac{\text{increment of pitching moment}}{qS\bar{c}}\right)$

ΔC_n increment of yawing-moment coefficient $\left(\frac{\text{increment of yawing moment}}{qSb}\right)$

α angle of attack of the fuselage reference line with respect to the wind axis, degrees

$\Delta\alpha$ increment of angle of attack, degrees

δ_{lf} leading-edge flap deflection, positive downward, degrees

δ_{tf} trailing-edge flap deflection, positive downward, degrees

ϵ effective downwash angle at the tail, degrees

ψ angle of yaw of the fuselage reference line with respect to the wind axis, degrees

η_t $\frac{q_t}{q}$

ρ mass density in the free stream, slugs per cubic foot

ρ_t mass density at the tail, slugs per cubic foot

A aspect ratio

b wing span, feet

b_t horizontal-tail span, feet

c wing chord, feet

$\bar{c}$ mean aerodynamic chord of the wing $\left(\dfrac{\int_0^{b/2} c^2\,dy}{\int_0^{b/2} c\,dy}\right)$, feet

c_t tail chord

$\overline{c_t}$ mean aerodynamic chord of the exposed horizontal tail

$$\left(\frac{\int_{0.045\,b_t}^{b_t/2} {c_t}^2 dy_t}{\int_{0.045\,b_t}^{b_t/2} c_t\,dy_t}\right), \text{ feet}$$

i_t horizontal tail incidence with respect to the fuselage reference line, positive with the trailing edge downward, degrees

M free-stream Mach number

q free-stream dynamic pressure $\left(\frac{1}{2}\rho V^2\right)$, pounds per square foot

q_t dynamic pressure at the tail $\left(\frac{1}{2}\rho_t {V_t}^2\right)$, pounds per square foot

R Reynolds number based on the mean aerodynamic chord of the wing

S wing area, square feet

S_t tail area, square feet

S_{t_e} exposed tail area, square feet

V free-stream velocity, feet per second

V_t velocity at the tail, feet per second

y perpendicular distance along the wing semispan from the model plane of symmetry, feet

y_t perpendicular distance along the horizontal-tail semispan from the model plane of symmetry, feet

MODEL AND APPARATUS

The 0.16-scale model of the X-3 airplane, shown in figure 1, was furnished by the Douglas Aircraft Company. The wing of the model had an aspect ratio of 3.01 and a thickness of 4.5 percent of the chord. The wing and vertical tail had symmetrical hexagonal sections with rounded corners at 30- and 70-percent chord and relatively sharp leading and trailing edges. Outboard of station 3.095 (inches model scale), the horizontal tail had the same section as the wing and vertical tail. Between stations 3.095 and 0.377 (the fuselage juncture), the section changed to a symmetrical diamond with rounded corners at 50-percent chord. The pertinent dimensions of the model are listed in table I.

The wing had plain full-span leading-edge flaps of constant chord (13.45 percent of the mean aerodynamic chord). Partial-span, split, trailing-edge flaps having a chord of 25 percent of the wing chord extended from the wing-fuselage juncture to the aileron (46.6 percent of the semispan). An aileron was provided on the left wing. The external brackets for the leading-edge flaps and ailerons of the full-scale airplane were simulated on the model. The all-movable horizontal tail was provided with an electric resistance-type strain gage for measuring hinge moments. The vertical tail had a movable rudder. The leading-edge flaps, aileron, and rudder had radius noses with unsealed gaps that could be considered negligible.

The stabilizing fins for the jettisonable nose had a circular-arc cross section with sharp leading and trailing edges. In the normal position, the fins were mounted at 4, 8, and 12 o'clock locations, while for the alternate position they were at the 2, 6, and 10 o'clock locations. The model was furnished with landing gear and landing-gear doors as shown in figure 2. Air scoops were not installed during the test program. The complete model as discussed in this report includes the fuselage, tail boom, canopy, wing and empennage, nose fins, and the external brackets for the leading-edge flaps and ailerons. Unless otherwise noted, the flaps and control surfaces were undeflected and the tail incidence was 0°.

The tests were conducted in the Ames 16-foot high-speed wind tunnel. The model was mounted on the sting-type support system as shown by figures 2, 3, and 4. Forces and moments on the model were measured by an electric resistance-type strain-gage balance enclosed within the model. This balance is capable of measuring four components of force and moment. With the model upright, normal force, chord force, pitching moment, and rolling moment were measured. With the wing in a vertical plane, the model could be yawed and the side force, yawing moment, and rolling moment determined. Figure 5 shows the position of the model during the yaw tests. The angles of attack or yaw of the model were measured visually with a protractor mounted outside of the tunnel test section.

PRECISION AND CORRECTIONS

The following values in coefficient form are the estimated maximum errors of measurement at Mach numbers of 0.40 and 0.90:

M	C_L	C_D	C_m	ΔC_l	ΔC_n	ΔC_c
0.40	±0.015	±0.0023	±0.003	±0.002	±0.002	±0.015
.90	±.009	±.0014	±.002	±.001	±.001	±.009

The angles of attack or yaw are believed to be correct within ±0.2°.

The results have been corrected for the effects of the wind-tunnel walls by the addition of the following (reference 1):

$$\Delta\alpha \text{ (deg)} = 0.164\, C_L$$

$$\Delta C_D = 0.0029\, C_L^2$$

$$\Delta C_m = 0.0019\, C_L$$

Corrections for the effect of the tunnel walls on the angle of yaw are considered negligible and have been omitted.

Interference effects of the sting support were determined at low speed by testing the model in the Ames 7- by 10-foot wind tunnel, with and without a dummy sting behind the fuselage (fig. 6). At a given angle of attack, the interference effects are believed not to vary with Mach number. Unpublished data on file at this Laboratory support this belief for Mach numbers up to 0.90. Interference tares, as applied to the data, are presented in figure 7.

Constriction corrections to account for the blocking effect of the model in the tunnel test section were applied according to the method of reference 2. The Mach number correction amounted to 0.40 percent at 0.70 Mach number and 1.45 percent at 0.90 Mach number.

Pressures were measured at five points on the flat base of the fuselage (the area occupied by the tail-pipe outlets of the airplane) and the drag data were corrected to correspond to free-stream static pressure over this area.

TESTS

Tests were made of the complete model with the nose fins in the normal and alternate positions and without the nose fins to evaluate their effect upon the longitudinal-stability characteristics. The complete model less the empennage and the nose fins was also investigated to determine the effect of the empennage on the stability and to estimate the downwash characteristics at the tail. The effectiveness of the horizontal tail was measured with the nose fins in the normal position.

The effect of the leading-edge flaps on the longitudinal-stability and lift characteristics of the model was evaluated from tests of several configurations with the leading-edge flaps deflected. The stability and lift characteristics of the complete model with and without the nose fins but with the landing gear extended and the leading- and trailing-edge flaps deflected were also obtained.

Tests were conducted of the complete model without the nose fins and with and without the empennage to evaluate the lateral- and directional-stability characteristics in yaw with the rudder undeflected.

The average Reynolds numbers of the test, shown in figure 8, increased from 2,120,000 to 4,920,000 as the Mach number was varied from 0.25 to 0.925.

DISCUSSION

Figures 7 through 43 represent practically all the data that were taken during the test. Although some of the figures are not discussed in detail, they have been included in the report as they are believed to be of interest and value to the manufacturer and to users of the airplane. An index of the figures giving aerodynamic data is presented in table II.

Lift Characteristics

Model without the nose fins.– The variation of lift coefficient with angle of attack (fig. 9(a)) was essentially linear up to the stall at all Mach numbers of the test. The slopes of the lift curves increased gradually as the Mach number was increased to 0.925 and are in reasonable agreement with the calculated theoretical values (fig. 33) using the method of reference 3 for a wing of aspect ratio 3.01 at Mach numbers below about 0.80. At Mach numbers above 0.80, the theoretical slopes are greater than the experimental. The large reduction in lift-curve slope that is characteristic of thicker wings of higher aspect ratio did not occur at any Mach number within the limit of the test.

With the leading-edge flaps undeflected, the model stalled at an angle of attack of about 12° at a Mach number of 0.25 and at slightly lower angles of attack at the higher Mach numbers. The lift coefficient at the stall varied from about 0.70 at a Mach number of 0.25 to 0.66 at a Mach number of 0.80. For Mach numbers above 0.85, the stall was not reached within the angle-of-attack range of the test, but the data indicate a marked increase in the lift coefficient at the stall as shown in figure 9(a). The lift beyond the stall, as indicated by unpublished data from the Ames 7- by 10-foot wind tunnels and from wing pressure distribution, was composed primarily of a combination of fuselage lift and increased pressure over the lower surface of the wing.

Deflecting the leading-edge flaps increased the lift coefficient at the stall for all Mach numbers of the test. (See figs. 10(a), 17(a), and 18(a).) A comparison of the lift curves of the model in various configurations (fig. 24) shows that, at 0.40 Mach number, deflecting the leading-edge flaps 30° delayed the stall from about 12° to 17° angle of attack and increased the lift coefficient at the stall from 0.71 to 1.03.

Model with the nose fins.- At 0.25 Mach number, the addition of the nose fins in the normal position (fig. 11(a)) caused the stall to be delayed to an angle of attack of approximately 19°. The maximum lift coefficient at the first stall was increased from 0.71 to 1.00 at a Mach number of 0.25. This increase in maximum lift coefficient is believed due primarily to the side nose fins turning the air downward as it approached the wing roots, thereby decreasing their effective angle of attack. Thus the separation of the flow from the wing was delayed until a higher angle of attack was reached. The addition of the nose fins caused only slight changes in the slopes of the lift curves and in the angles of attack for zero lift (figs. 9(a) and 11(a)).

Model in the landing configuration.- The lift curves of the model in the landing configuration (leading- and trailing-edge flaps deflected and the landing gear extended) with the nose fins in the normal position and without the nose fins are shown in figure 20(a). A maximum lift coefficient of approximately 1.38 was attained with or without the nose fins for the same flap and horizontal-tail settings. From wind-tunnel tests of a wing of similar section with an aspect ratio of 4, the effect of Reynolds number on the maximum lift coefficient appeared to be of little significance (references 4 and 5). Thus it seems that the value of maximum lift coefficient attained by the model would probably be close to that for the full-scale airplane if allowance is made for the tail lift necessary to balance the airplane.

Static Longitudinal Stability and Control

Model without the nose fins.- Figure 9(b) shows that the variation of pitching-moment coefficient with lift coefficient was not linear at any of the test Mach numbers, but indicates that the model was stable for lift coefficients below the stall. The static longitudinal stability $(-\partial C_m/\partial C_L)_{C_L}$ was, in general, less in the region of about 0.3 lift coefficient than above or below this region for Mach numbers below 0.85 (fig. 9(b)).

The variation of neutral point with Mach number shown in figure 33 for lift coefficients of 0 and 0.3 indicates that the most forward position of the neutral point was approximately 19 percent of the mean aerodynamic chord at a Mach number of about 0.80. Thus with the center of gravity at 15 percent of the mean aerodynamic chord, a minimum stability margin of about 4 percent was retained.

The pitching-moment characteristics of the model without the empennage (fig. 10(b)) show a marked increase in stability $(-\partial C_m/\partial C_L)_{C_L}$ at lift coefficients between about 0.35 and the stall. Since the fuselage alone without the nose fins is definitely unstable (fig. 23(a)), the positive stability in this region is believed to be due to the rapid rearward movement of the area of separated flow on the upper surface of the wing as the angle of attack was increased. (See photographs of tufts, fig. 37.)

Figure 31 shows the variation of the pitching-moment coefficient with Mach number for the model with and without the empennage. A pitching-down tendency developed at a Mach number of approximately 0.85 as indicated by the decrease in pitching-moment coefficient for constant lift coefficients.

A comparison of the tail-on and tail-off pitching-moment characteristics (fig. 23) indicates that the tail was destabilizing for angles of attack between 14° and 18°. It is believed that this destabilizing action was due to a changing downwash pattern over the tail in the angle-of-attack region beyond the wing stall. The downwash over the tail (fig. 35) calculated from tail-on and tail-off pitching-moment data shows that the rate of change of downwash with angle of attack was approximately 1.0 at 14° angle of attack and the rate was increasing with angle of attack. Whenever the effective downwash increases faster than the angle of attack $[(d\epsilon/d\alpha)>1.0]$ the tail action is destabilizing.

Model with the nose fins.– The pitching-moment characteristics of the model with the jettisonable-nose fins in the normal position are presented in figures 11(b) and 12(b). Instability occurred at a lift coefficient of approximately 0.6 for Mach numbers of 0.80 and lower. The effect of the nose fins on the pitching-moment characteristics of the model is shown in figures 22 and 23. A greater destabilizing effect occurred with the fins in the alternate position than in the normal position at 0.40 Mach number for lift coefficients less than approximately 0.6.

Figure 34 shows the effectiveness of the tail $\eta_t(\partial C_{L_t}/\partial i_t)_\alpha$ for several Mach numbers. The general decrease of tail effectiveness with angle of attack is presumed to be caused by the tail entering a region of lower-energy air. The tail effectiveness generally increased with increasing Mach number to a value of 0.073 per degree at 0.90 Mach number and 0° angle of attack.

Effect of the leading-edge flaps.– Figures 13(b), 14(b), and 15(b) present data for leading-edge flap angles of 10°, 20°, and 30°, respectively, for the model with the nose fins in the normal position. Deflecting the leading-edge flaps did not alleviate the instability that occurred at a lift coefficient of approximately 0.6. A pitching-down tendency that occurred at approximately 0.85 Mach number was not changed significantly by deflecting the leading-edge flaps 30° (fig. 32).

The pitching-moment characteristics of the model with the leading-edge flaps deflected but without the nose fins are presented in figure 25. Although deflecting the flaps 30° produced only small changes in the longitudinal stability, the lift coefficient for balance was reduced significantly.

Model in the landing configuration.– The longitudinal-stability characteristics (fig. 20(b)) show that the model with the nose fins in the normal position and with a tail incidence of –5° became highly unstable for lift coefficients between about 0.8 and the stall. Without the nose fins, the model became neutrally stable at a lift coefficient of about 0.8 and only slightly unstable at the stall. The destabilizing effects of the nose fins for this configuration appear to make their use impractical. Unpublished low-speed wind-tunnel data indicate that by modifying the landing-gear doors and moving the center of gravity slightly forward, satisfactory static longitudinal stability for landing can be obtained for the model without the nose fins.

Horizontal-tail hinge moments.– Although only slight variations of hinge-moment coefficient with lift coefficient occurred below the stall for the model without the nose fins (fig. 9(d)), a large decrease in hinge-moment coefficient followed the stall. This decrease was probably caused by a change in the downwash pattern at the tail. The negative hinge moments that occurred at lift coefficients below the stall, although increasing with Mach number, could be significantly reduced by a fixed tab.

From the limited data available (fig. 36), deflecting the leading-edge flaps did not significantly change the horizontal-tail hinge-moment characteristics below the stall, nor did decreasing the tail incidence from 0° to –5° increase the hinge moments significantly. Thus, it appears that the tail was well-balanced aerodynamically in the region of 0° to –5° incidence of the tail.

Lateral and Directional Stability

Model without the nose fins.– The lateral and directional stability characteristics of the model with the empennage on and off and the rudder undeflected are shown in figure 21. Adding the empennage increased the side force on the model approximately 100 percent for angles of yaw less than 10°. The directional stability of the model $(-\partial C_n/\partial\psi)_\alpha$ had a value of about 0.008 between 0.40 and 0.85 Mach numbers and increased to 0.010 at 0.925 Mach number. Although these values are considered high, they might be less for the full-scale airplane because of the elastic deflection of the tail boom. The model was directionally unstable with the empennage off at all Mach numbers. The rolling-moment coefficient due to yaw $(\partial C_l/\partial\psi)_\alpha$ had a constant value of approximately 0.0022 for all Mach numbers below 0.925 (fig. 21(c)). This rolling-moment coefficient was primarily due to the action of the vertical-tail surface. Thus it appears that with the rudder deflected there is a possibility that the rolling-moment characteristics would be unfavorable.

Drag Characteristics

Model without the nose fins.- Although a slight increase in drag coefficient is apparent at a Mach number of 0.925 (fig. 9(c)), the Mach number for drag divergence, as indicated by a marked increase in drag coefficient, was not reached within the Mach number range of the test. The minimum drag coefficient was approximately 0.022. From the variation of drag coefficient with lift coefficient, it appears that the increment of drag coefficient with increasing lift was approximately $2C_L^2/\pi A$ or twice the induced drag coefficient predicted by simple airfoil theory.

The drag characteristics with the leading-edge flaps deflected (fig. 27) show that, at 0.40 Mach number, a reduction in drag occurred at the higher lift coefficients when the flap angle was increased to 30°. For Mach numbers of 0.40 to 0.80 and between lift coefficients of 0.1 and at least 0.7, the drag was reduced by deflecting the leading-edge flaps 10° (fig. 27). Thus it appears that, for cruising at high subsonic Mach numbers, deflecting the leading-edge flaps in the neighborhood of 10° would be beneficial.

Model with the nose fins.- Figure 30 presents data showing the effect of several changes in configuration on the variation of drag coefficient with lift coefficient. At 0.40 Mach number with the leading-edge flaps deflected 30°, adding the nose fins in the normal position increased the drag coefficient over most of the lift-coefficient range. However, at 0.80 and 0.90 Mach numbers the data indicate that the drag was slightly reduced by adding the nose fins.

Figure 30(a) shows that, at 0.40 Mach number, the optimum flap angle for reducing the drag at lift coefficients between 0.25 and 0.88 was approximately 20°. At the higher Mach numbers (figs. 30(b) and 30(c)), increasing the deflection of the leading-edge flaps increased the drag at most lift coefficients.

Wing and Fuselage Tuft Studies

Model without the nose fins.- Photographs of tufts indicating the flow over the upper surface of the model in pitch (figs. 37 to 40) indicate two distinct stall patterns on the wing. At Mach numbers below 0.80, the flow became rough or separated near the leading edge at an angle of attack of approximately 4°. This roughness or separation progressed toward the trailing edge as the angle of attack was increased. At an angle of attack of 12° the upper surface was completely stalled. For Mach numbers of 0.90 and 0.925, the separation began at the trailing edge at an angle of attack of approximately 5° and progressed toward the leading edge.

With the model at an angle of attack of 6.2° and between Mach numbers of 0.40 and 0.80, roughness or separation of the flow increased over the trailing wing as the angle of yaw increased (figs. 41 to 43). This roughness or separation originated from the leading edge near the tip and progressed inboard and aft. The amount of roughness or separation of the flow over the leading wing did not appear to increase with angle of yaw.

CONCLUDING REMARKS

The results of lateral- and longitudinal-stability tests of the 0.16-scale X-3 (MX-656) model show a gradual increase in lift-curve slope for Mach numbers up to 0.925 and indicate no large decreases in the stalling lift coefficient throughout the Mach number range of the tests. Deflecting the leading-edge flaps increased the lift coefficient at the stall and at the lower Mach numbers improved the drag characteristics. Although a slight increase in drag coefficient occurred at a Mach number of 0.925, the Mach number for drag divergence was not reached within the range of the test.

Adding the jettisonable-nose fins affected the stability characteristics to such an extent that their use was considered impractical. For the model without the nose fins, the static longitudinal stability was satisfactory and the most forward position of the neutral point was at approximately 19 percent of the mean aerodynamic chord at a Mach number of 0.80. The effectiveness of the tail for providing control was retained to a Mach number of 0.925.

Without the nose fins, the directional stability of the model was considered high, although not excessive for Mach numbers of the test.

Ames Aeronautical Laboratory,
National Advisory Committee for Aeronautics,
Moffett Field, Calif.

REFERENCES

1. Silverstein, Abe, and White, James A.: Wind-Tunnel Interference with Particular Reference to Off-Center Positions of the Wing and to the Downwash at the Tail. NACA Rep. 547, 1935.

2. Herriot, John G.: Blockage Corrections for Three-Dimensional-Flow Closed-Throat Wind Tunnels, with Consideration of the Effect of Compressibility. NACA RM A7B28, 1947.

3. Young, A. D.: Note on the Effect of Compressibility on the Lift-Curve Slope of a Wing of Finite Span. TN No. Aero. 1250, R.A.E., Aug. 1943.

4. Johnson, Ben H., Jr.: Investigation of a Thin Wing of Aspect Ratio 4 in the Ames 12-Foot Pressure Wind Tunnel. I - Characteristics of a Plain Wing. NACA RM A8D07, 1948.

5. Johnson, Ben H., Jr., and Bandettini, Angelo: Investigation of a Thin Wing of Aspect Ratio 4 in the Ames 12-Foot Pressure Wind Tunnel. II - The Effect of Constant-Chord Leading- and Trailing-Edge Flaps on the Low-Speed Characteristics of the Wing. NACA RM A8F15, 1948.

TABLE I.— MODEL DIMENSIONS

Wing	
Area, sq ft	4.094
Aspect ratio	3.01
Taper ratio	0.4
Span, ft	3.51
Root section (at plane of symmetry) chord, ft	1.666
Thickness, percent of chord	4.5
Dihedral (wing reference plane), deg	0
Incidence, deg	0
Mean aerodynamic chord, ft	1.238
Sweepback (75-percent-chord line), deg	0
Aileron	
Span, ft	0.526
Wing station at inner end, ft	1.227
Wing station at outer end, ft	1.753
Chord at inner end, ft	0.241
Chord at outer end, ft	0.167
Horizontal tail	
Area, sq ft	0.794
Area, exposed, sq ft	0.701
Aspect ratio	3.01
Taper ratio	0.4
Span, ft	1.547
Tail length (center of gravity to one-quarter mean aerodynamic chord of horizontal tail), ft	3.393
Section at spanwise station (fuselage juncture), 0.377 in.	
Chord, ft	0.752
Thickness, percent of chord	7.5
Section at spanwise station, 3.095 in.	
Chord, ft	0.587
Thickness, percent of chord	4.5
Tip section	
Chord, ft	0.294
Thickness, percent of chord	4.5
Dihedral, deg	0
Incidence	variable
Mean aerodynamic chord, ft	0.545
Mean aerodynamic chord, exposed, ft	0.521
Sweepback (50-percent-chord line), deg	23

NACA

TABLE I.– CONCLUDED

Vertical tail	
Area, sq ft	0.678
Aspect ratio	1.32
Taper ratio	0.25
Span, ft	0.947
Tail length (center of gravity to one-quarter mean aerodynamic chord of vertical tail), ft	3.410
Root section	
Chord, ft	1.147
Thickness, percent of chord	4.5
Tip section	
Chord, ft	0.287
Thickness, percent of chord	4.5
Mean aerodynamic chord, ft	0.802
Sweepback (90-percent-chord line), deg	0
Rudder	
Span, ft	0.705
Height of lower end above fuselage reference plane, ft	0.690
Height of upper end above fuselage reference plane, ft	1.395
Chord at inboard end, ft	0.227
Chord at outboard end, ft	0.162
Jettisonable-nose fins	
Area (each fin), sq ft	0.0845
Aspect ratio	0.75
Taper ratio	0.25
Span, ft	0.2535
Fin length (center of gravity to one-quarter mean aerodynamic chord of fin), ft	0.550
Root section	
Chord, ft	0.533
Thickness, percent of chord	3
Tip section	
Chord, ft	0.133
Thickness, percent of chord	3
Mean aerodynamic chord, ft	0.373
Sweepback (90-percent-chord line), deg	0

NACA

TABLE II.– FIGURE INDEX

Wing, fuselage, and boom							Figure number						
Tail	Nose fins	Canopy	Landing gear	i_t	δ_{lf}	δ_{tf}	C_L vs α	C_m vs C_L	C_D vs C_L	C_{h_t} vs C_L	ΔC_c vs ψ	ΔC_n vs ψ	ΔC_l vs ψ
on	off	on	off	0°	0°	0°	9(a)	9(b)	9(c)	9(d)	– –	– –	– –
off	off	on	off	– –	0°	0°	10(a)	10(b)	10(c)	– –	– –	– –	– –
on	normal	on	off	0°	0°	0°	11(a)	11(b)	– –	– –	– –	– –	– –
on	normal	on	off	−5°	0°	0°	12(a)	12(b)	12(c)	12(d)	– –	– –	– –
on	normal	on	off	0°	10°	0°	13(a)	13(b)	13(c)	13(d)	– –	– –	– –
on	normal	on	off	0°	20°	0°	14(a)	14(b)	14(c)	– –	– –	– –	– –
on	normal	on	off	0°	30°	0°	15(a)	15(b)	15(c)	– –	– –	– –	– –
on	off	on	off	0°	30°	0°	16(a)	16(b)	16(c)	– –	– –	– –	– –
off	off	on	off	– –	10°	0°	17(a)	17(b)	17(c)	– –	– –	– –	– –
off	off	on	off	– –	20°	0°	18(a)	18(b)	18(c)	– –	– –	– –	– –
on	off	on	off	−5°	30°	0°	19(a)	19(b)	19(c)	– –	– –	– –	– –
on	off	on	on	−5°	30°	50°	20(a)	20(b)	20(c)	– –	– –	– –	– –
on	normal	on	on	−5°	30°	50°	20(a)	20(b)	20(c)	– –	– –	– –	– –
on	normal	on	on	−10°	30°	50°	20(a)	20(b)	20(c)	– –	– –	– –	– –
on	normal	on	on	−15°	30°	50°	20(a)	20(b)	20(c)	– –	– –	– –	– –
on	off	on	off	0°	0°	0°	– –	– –	– –	– –	21(a)	21(b)	21(c)
off	off	on	off	– –	0°	0°	– –	– –	– –	– –	21(a)	21(b)	21(c)

Miscellaneous Aerodynamic Data

Wing, fuselage, and boom							Type of data	Fig. No.
Tail	Nose fins	Canopy	Landing gear	i_t	δ_{lf}	δ_{tf}		
on	off	on	off	0°	0°	0°	C_m vs M	31
off	off	on	off	– –	0°	0°	C_m vs M	31
on	normal	on	off	0°	0°	0°	C_m vs M	32
on	normal	on	off	0°	30°	0°	C_m vs M	32
on	off	on	off	0°	0°	0°	$(\partial C_L/\partial \alpha)_{C_L}$ vs M	33
on	off	on	off	0°	0°	0°	Neutral point vs M	33
on	normal	on	off	0°	0°	0°	$\eta_t(\partial C_{L_t}/\partial i_t)_\alpha$ vs α	34
– –	off	on	off	0°	0°	0°	ϵ vs M, ϵ vs α	35
on	off	off	off	0°	0°	0°	Tufts; ψ, 0°	37–40, incl.
on	off	off	off	0°	0°	0°	Tufts; α, 6.2°	40–43, incl.

Comparative Aerodynamic Data

Data show	Type of data	Fig. No.
Effect of nose fins	C_m vs C_L	22
Do.	C_m vs α	23
Effect of changes in configuration	C_L vs α	24
Do.	C_m vs C_L	28
Do.	C_m vs α	29
Do.	C_D vs C_L	30
Effect of leading-edge flaps	C_m vs α	26
Do.	C_m vs C_L	25
Do.	C_D vs C_L	27
Do.	C_{h_t} vs C_L	36

NACA

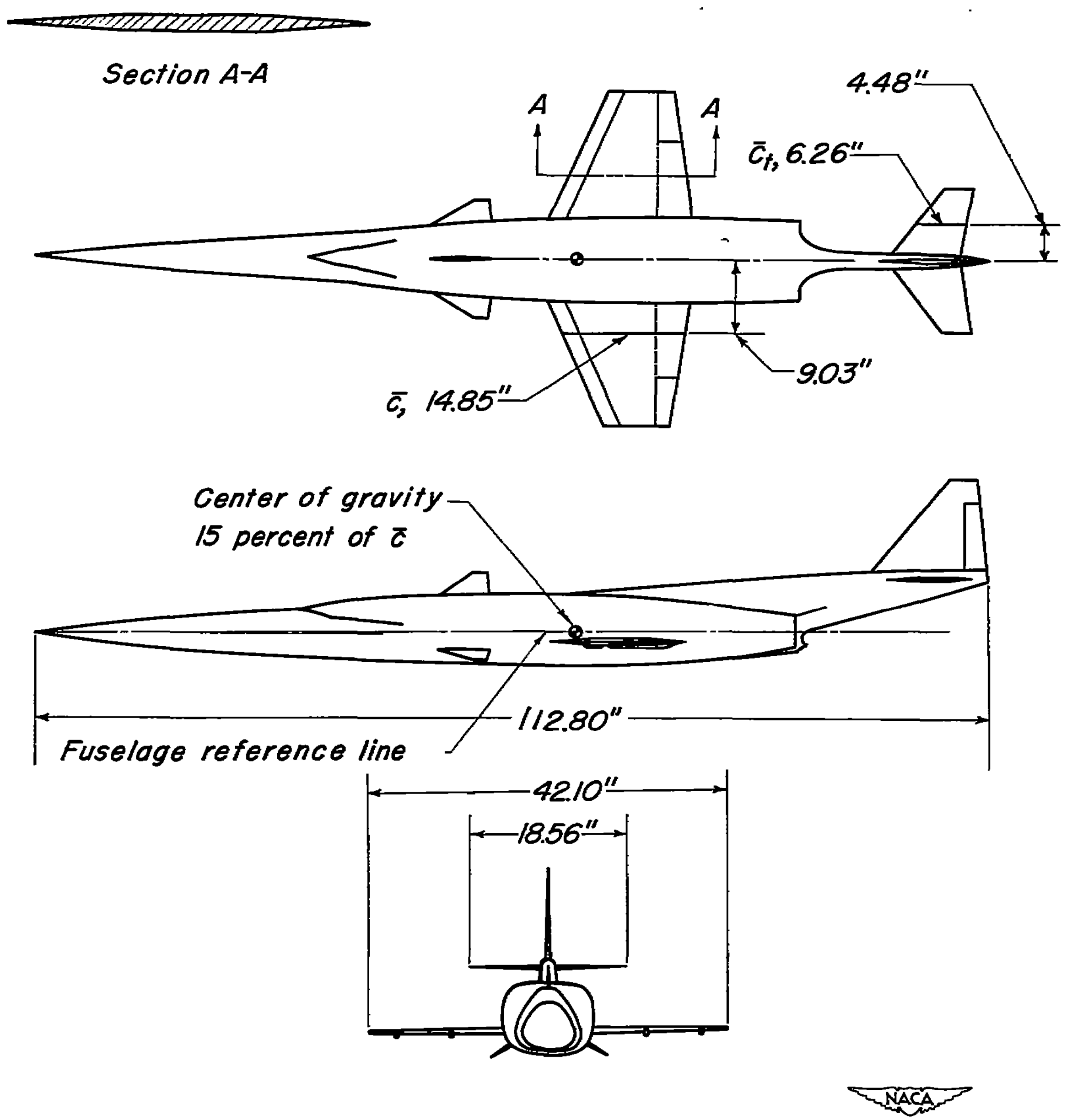

Figure 1.– The 0.16–scale model of the MX–656 airplane.

[redacted]

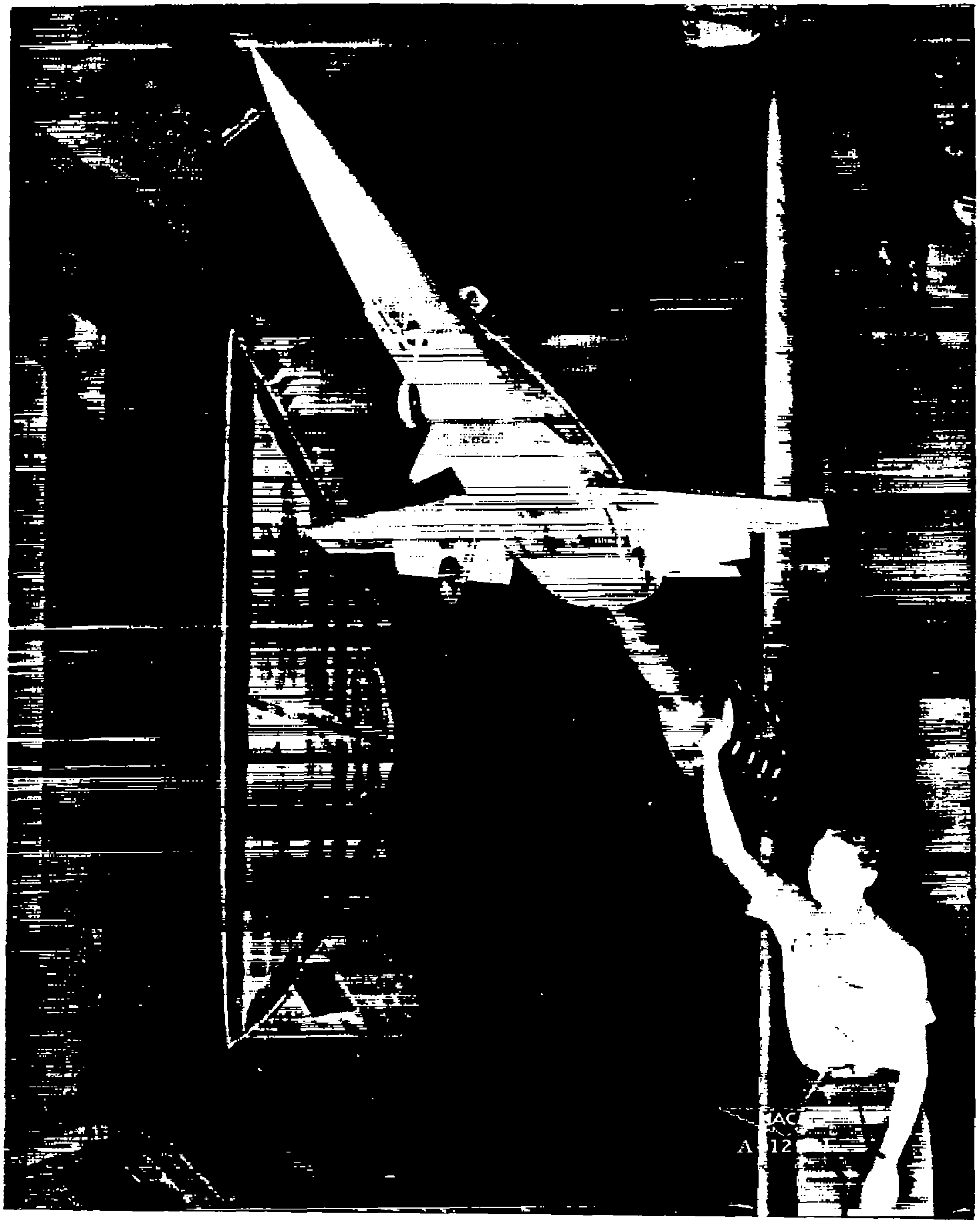

Figure 2.— A three-quarter front view of the MX-656 model with the landing gear extended, the flaps deflected, and the nose fins in the normal position.

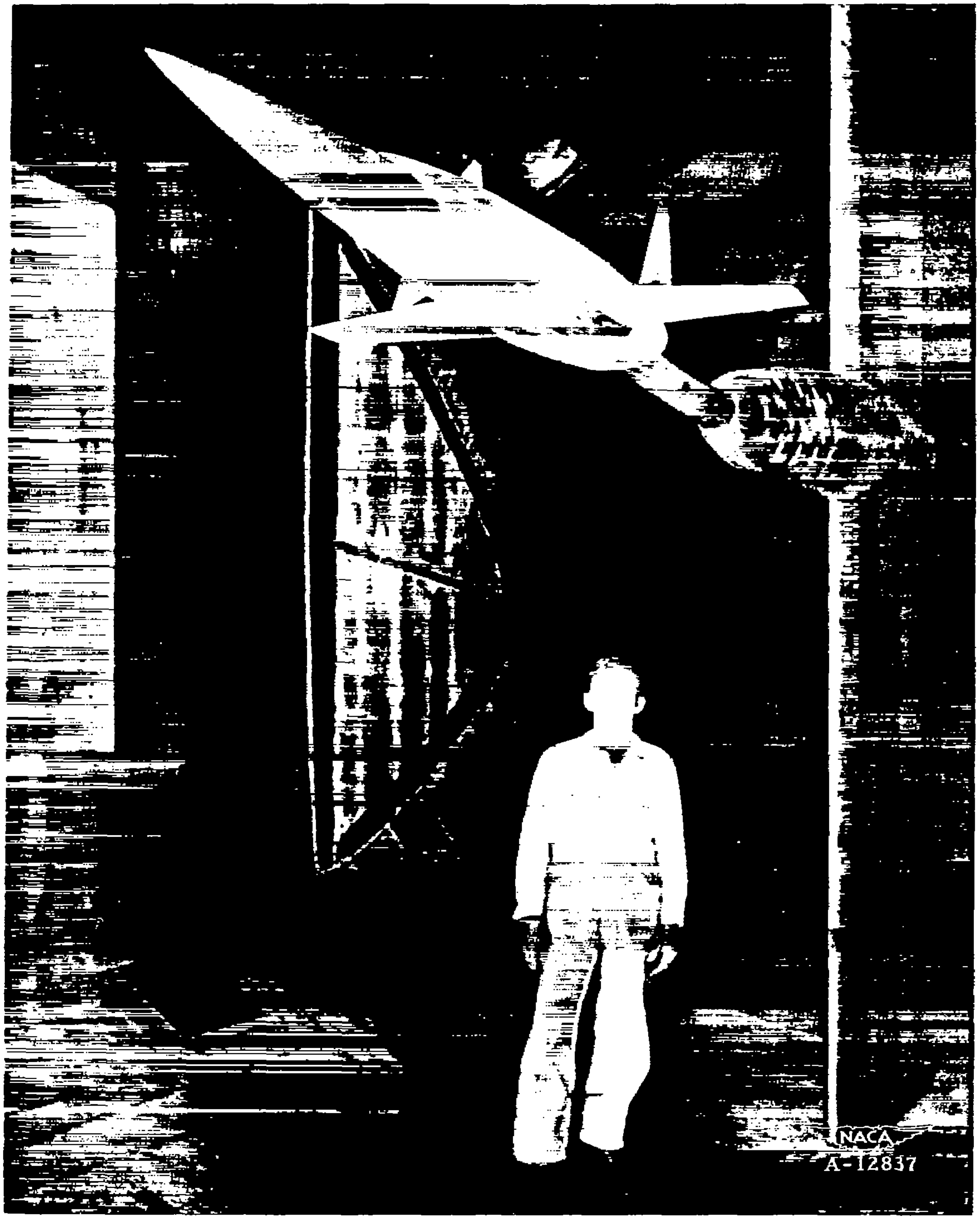

Figure 3.— A three-quarter front view of the MX-656 model with the nose fins in the normal position.

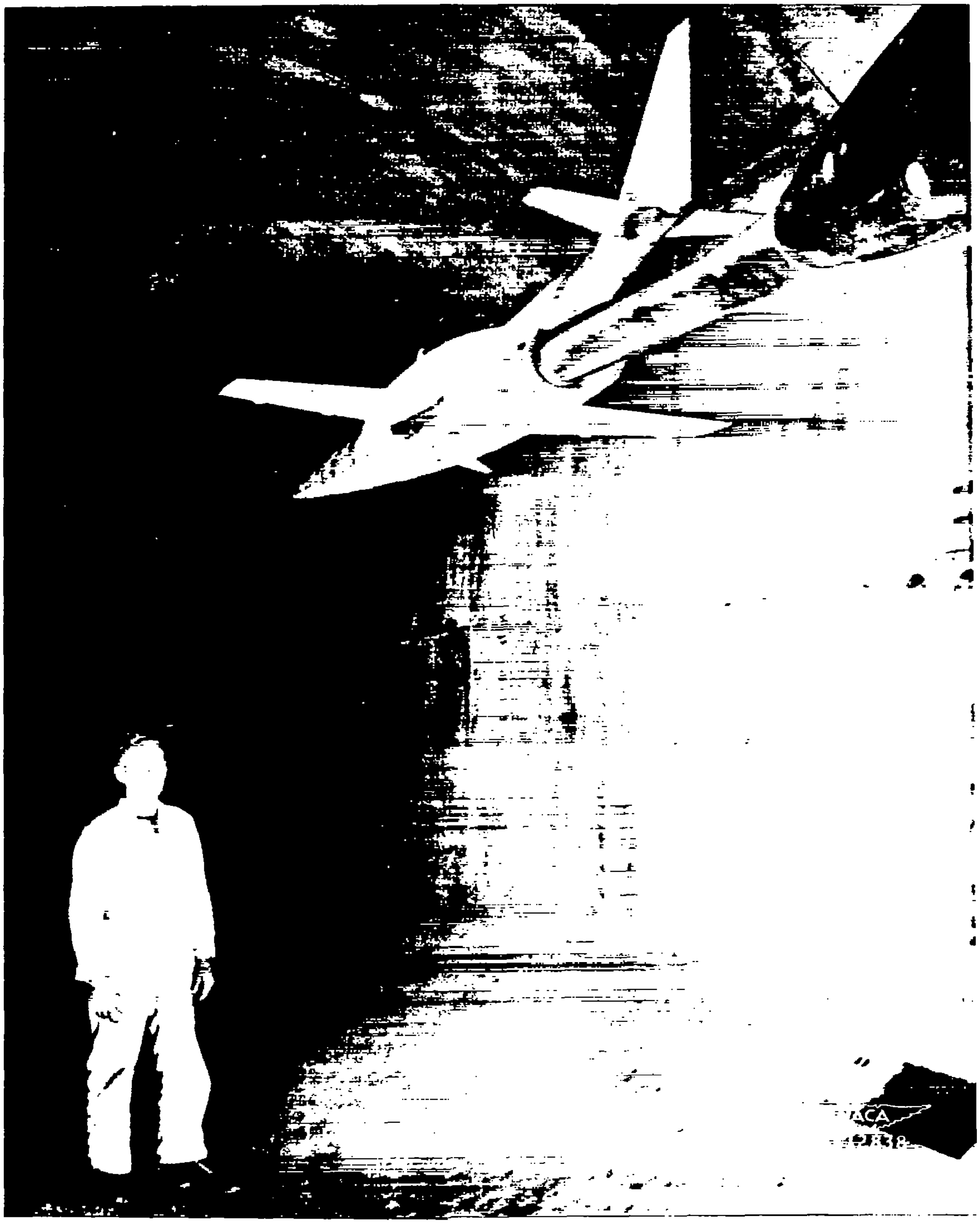

Figure 4.– A three-quarter rear view of the MX-656 model with the nose fins in the normal position.

[redacted]

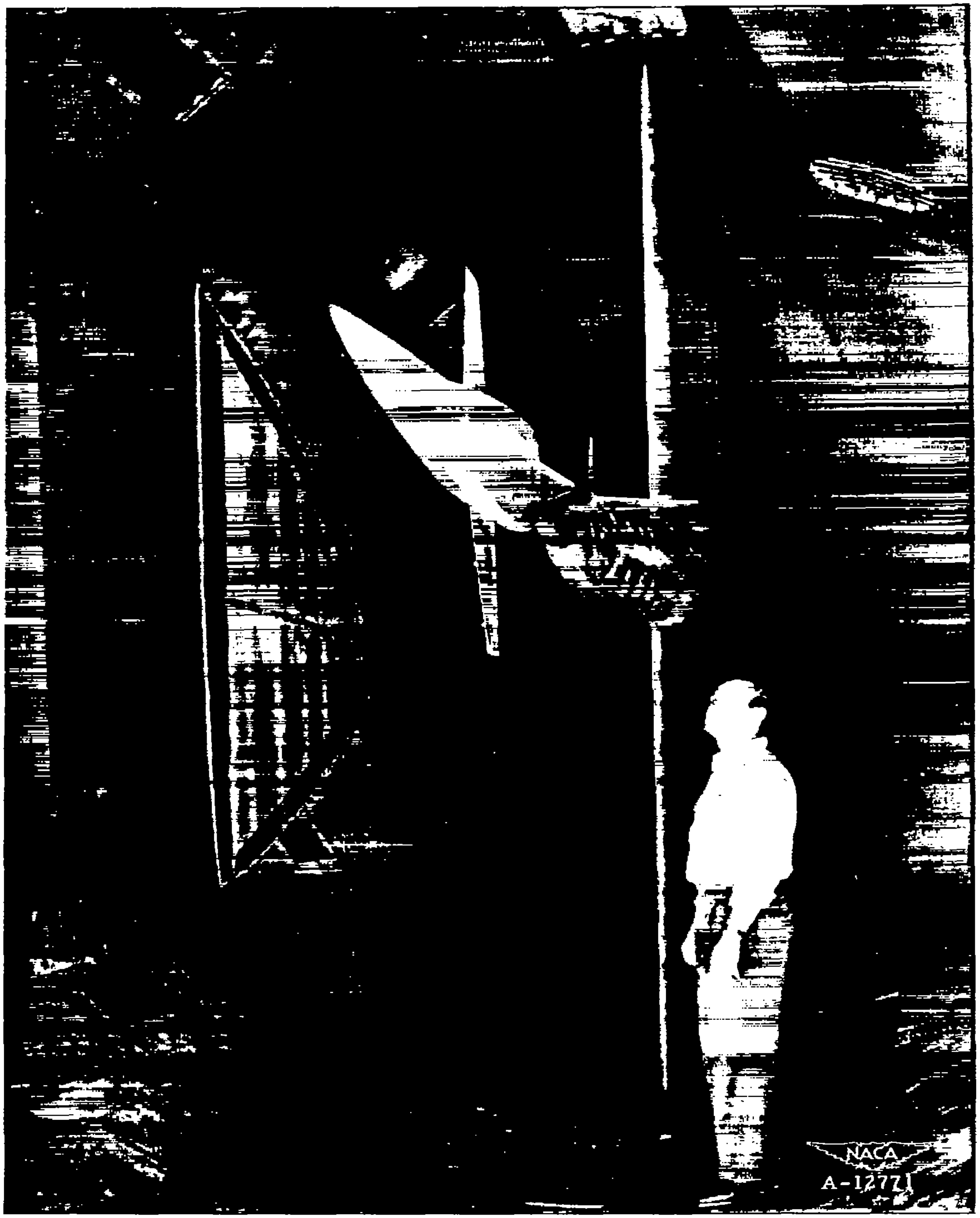

Figure 5.— A three-quarter front view of the MX-656 model mounted for yaw tests, without the nose fins.

Figure 6.– The MX-656 model mounted in the Ames 7- by 10-foot wind tunnel No. 2 for evaluation of the sting interference.

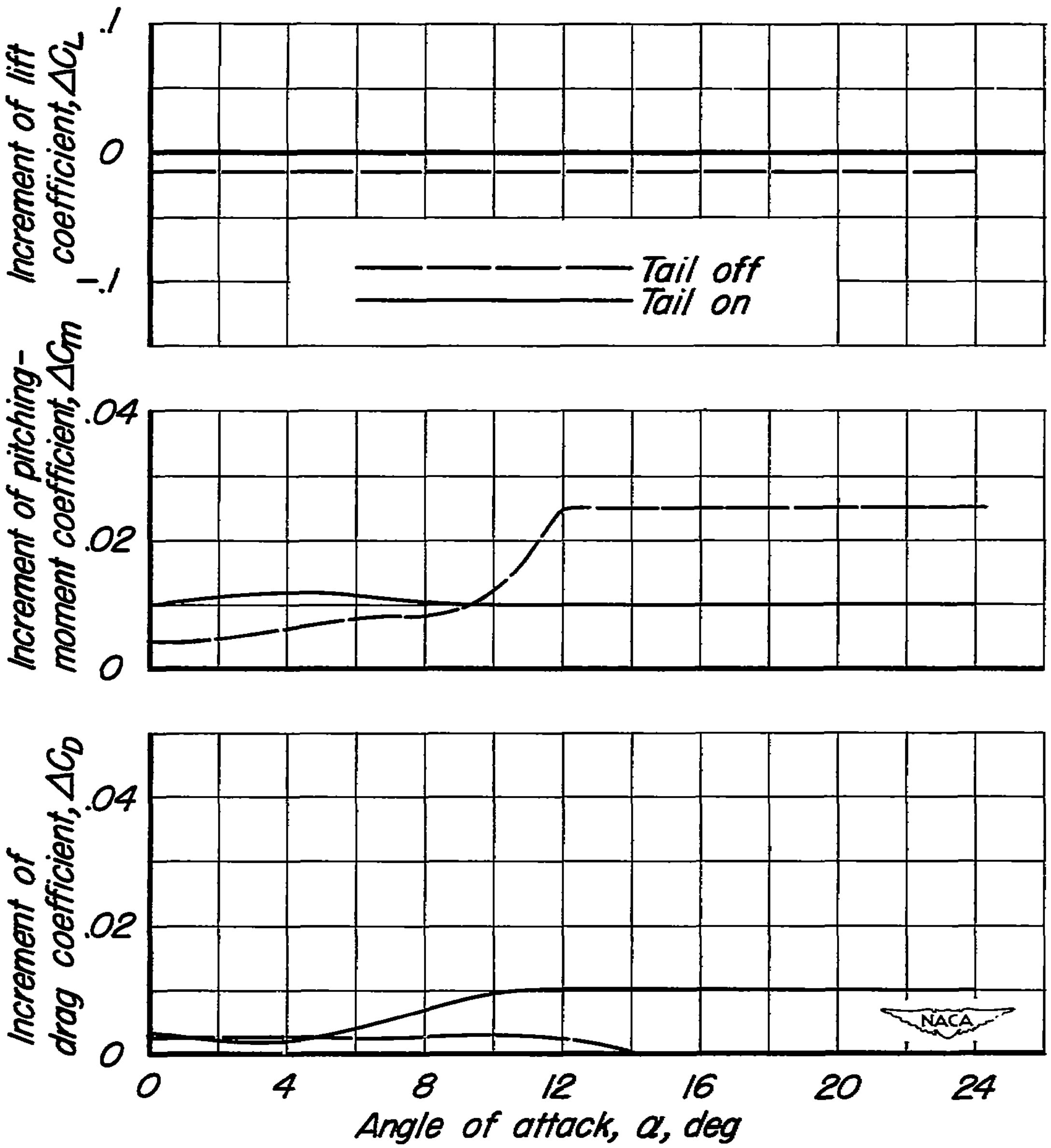

Figure 7.– The lift, drag, and pitching-moment tares for the MX-656 model in the Ames 16-foot high-speed wind tunnel.

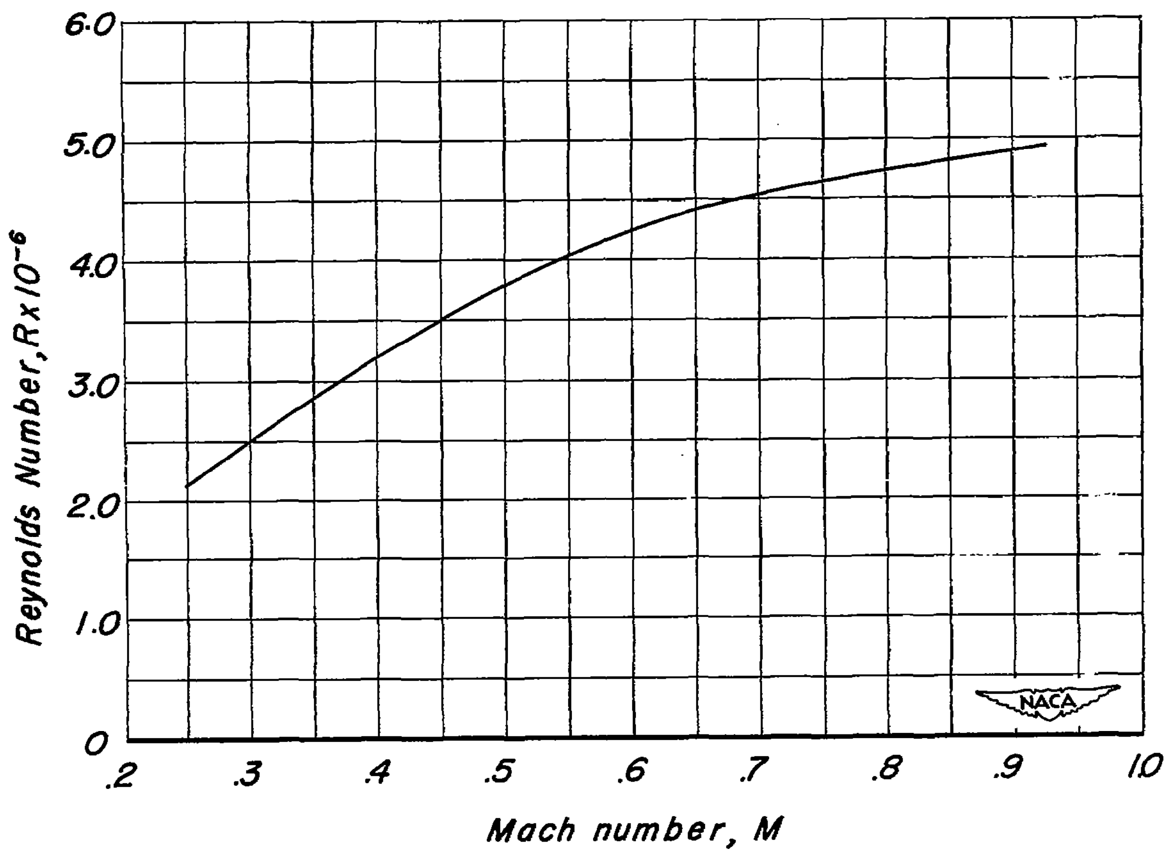

Figure 8.– The variation of Reynolds number with Mach number for the MX-656 model.

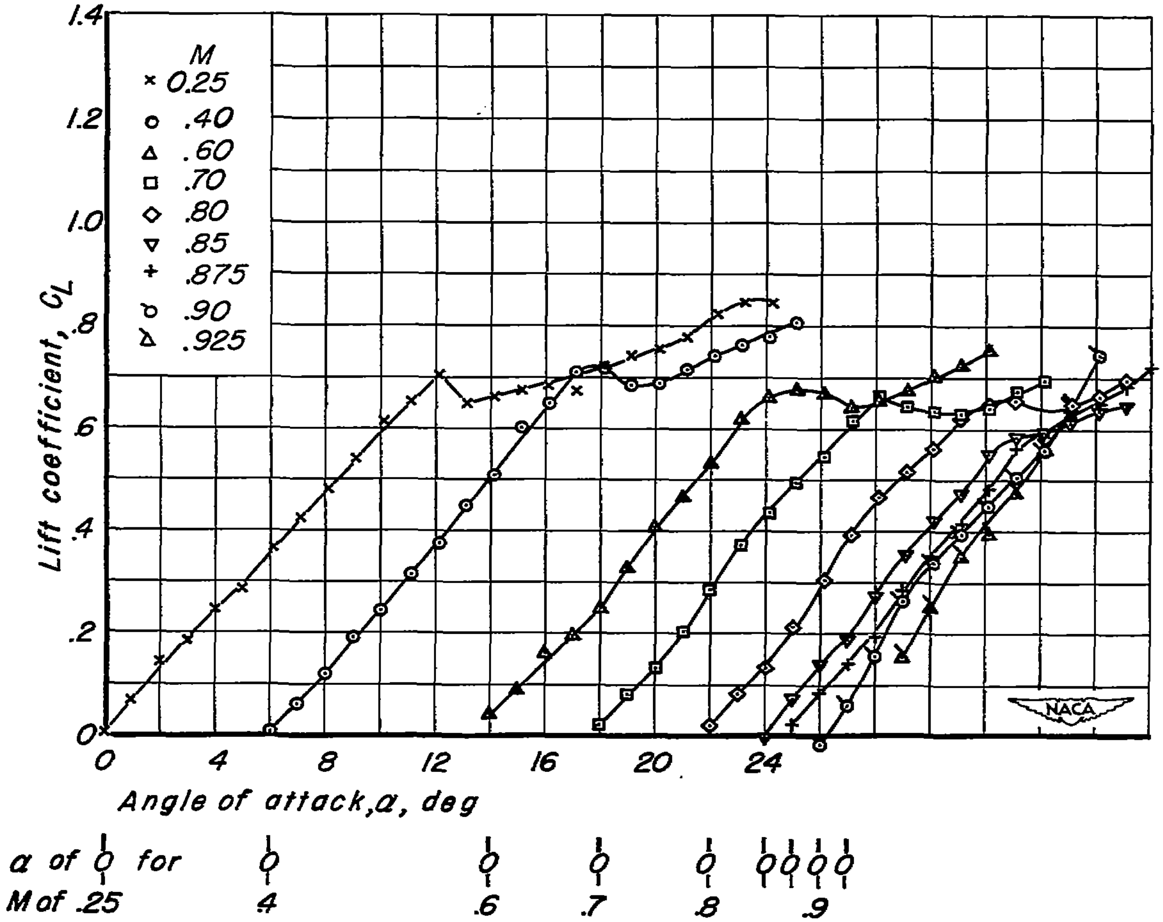

(a) Lift characteristics.

Figure 9.– The aerodynamic characteristics of the MX-656 model without the nose fins.

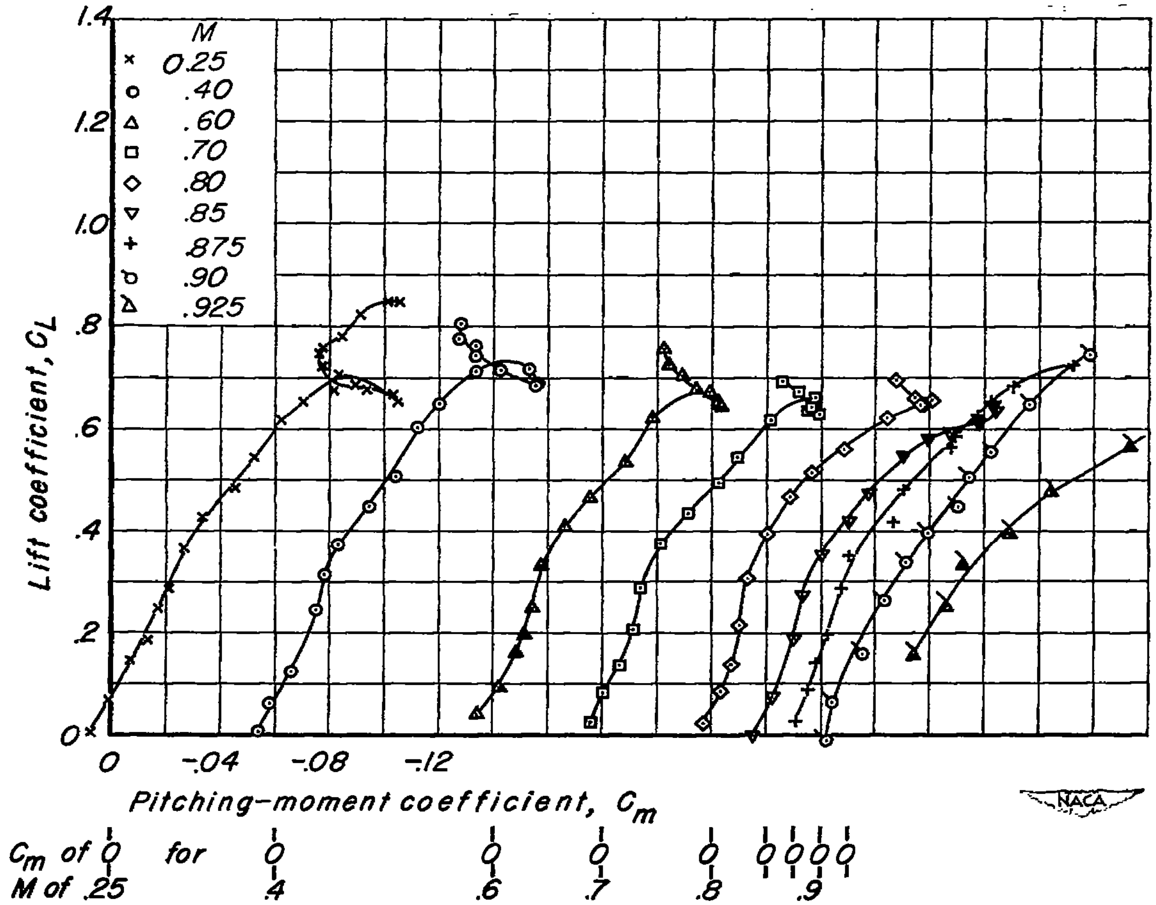

(b) Pitching-moment characteristics.

Figure 9.- Continued.

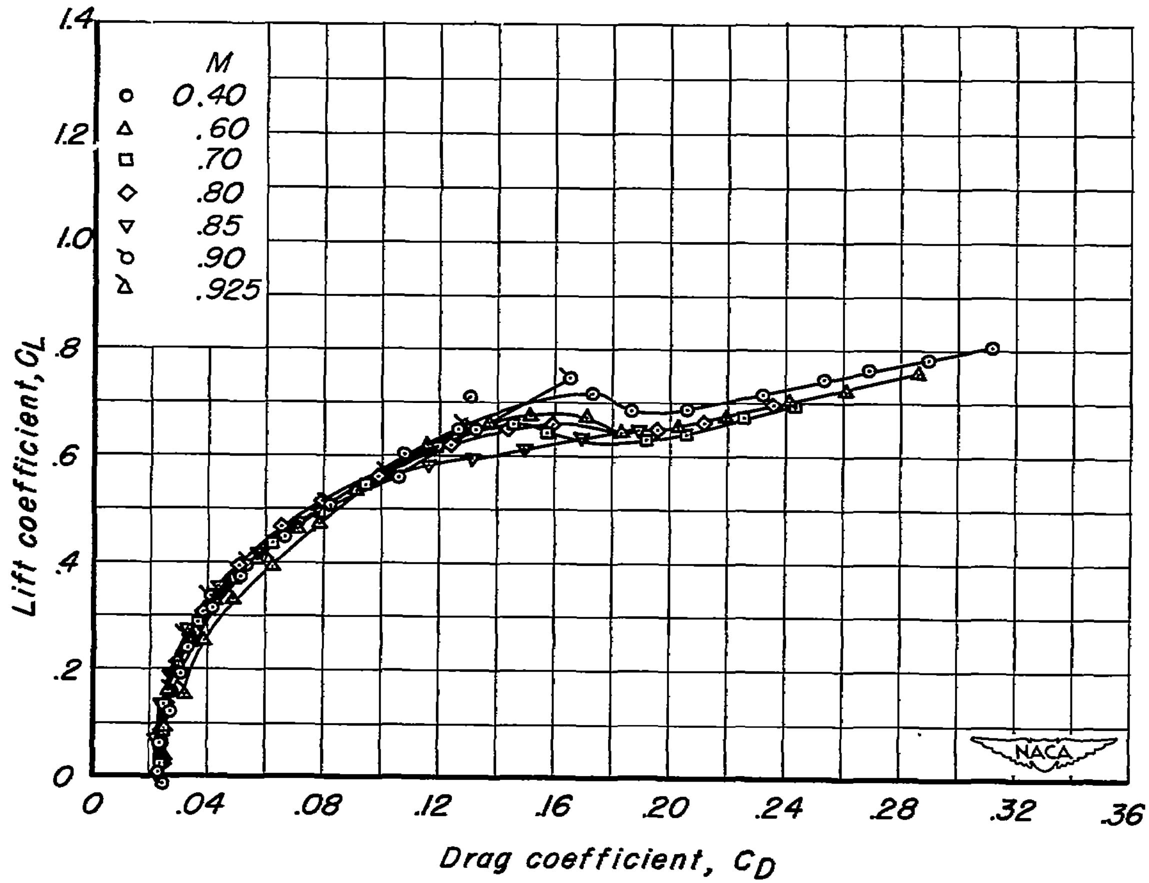

(c) Drag characteristics.

Figure 9.– Continued.

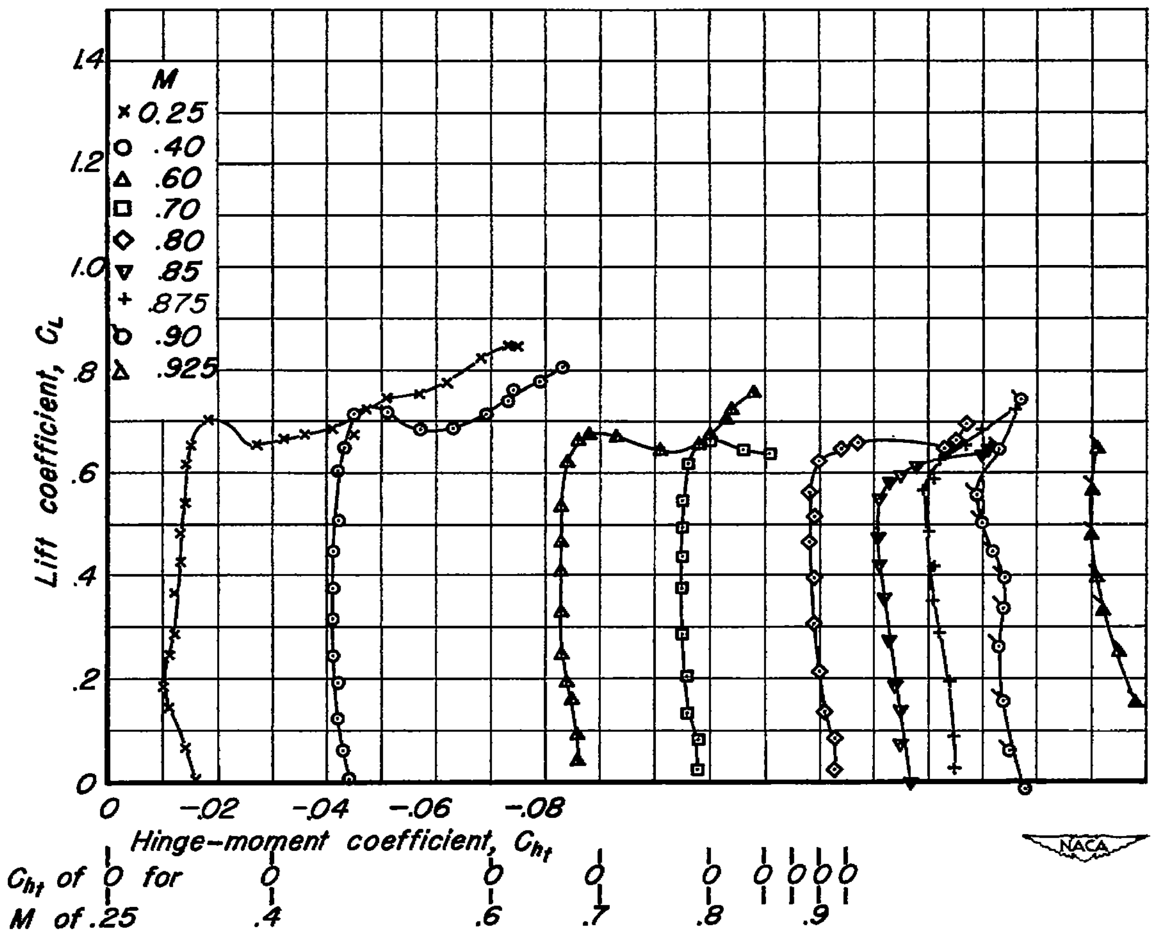

(d) Horizontal-tail hinge-moment characteristics.

Figure 9.— Concluded.

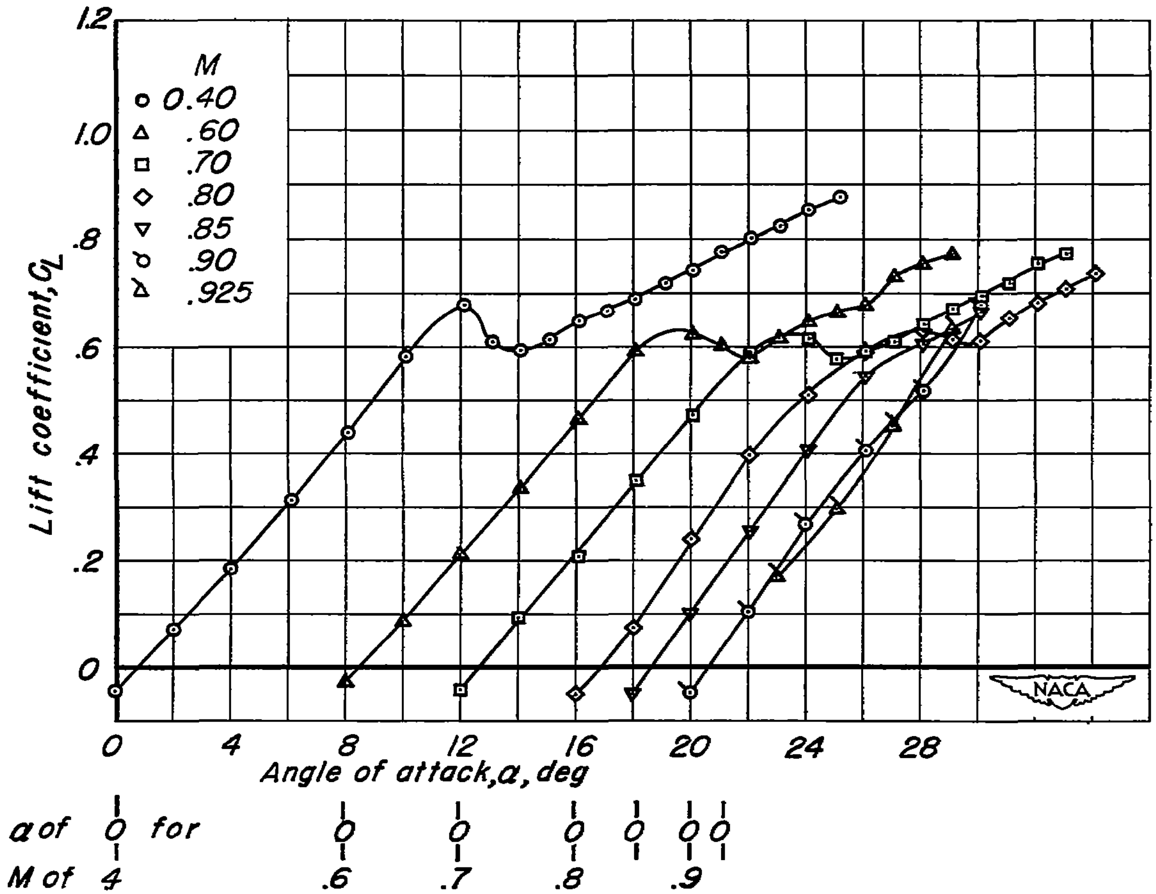

(a) Lift characteristics.

Figure 10.– The aerodynamic characteristics of the MX-656 model without the nose fins and the empennage.

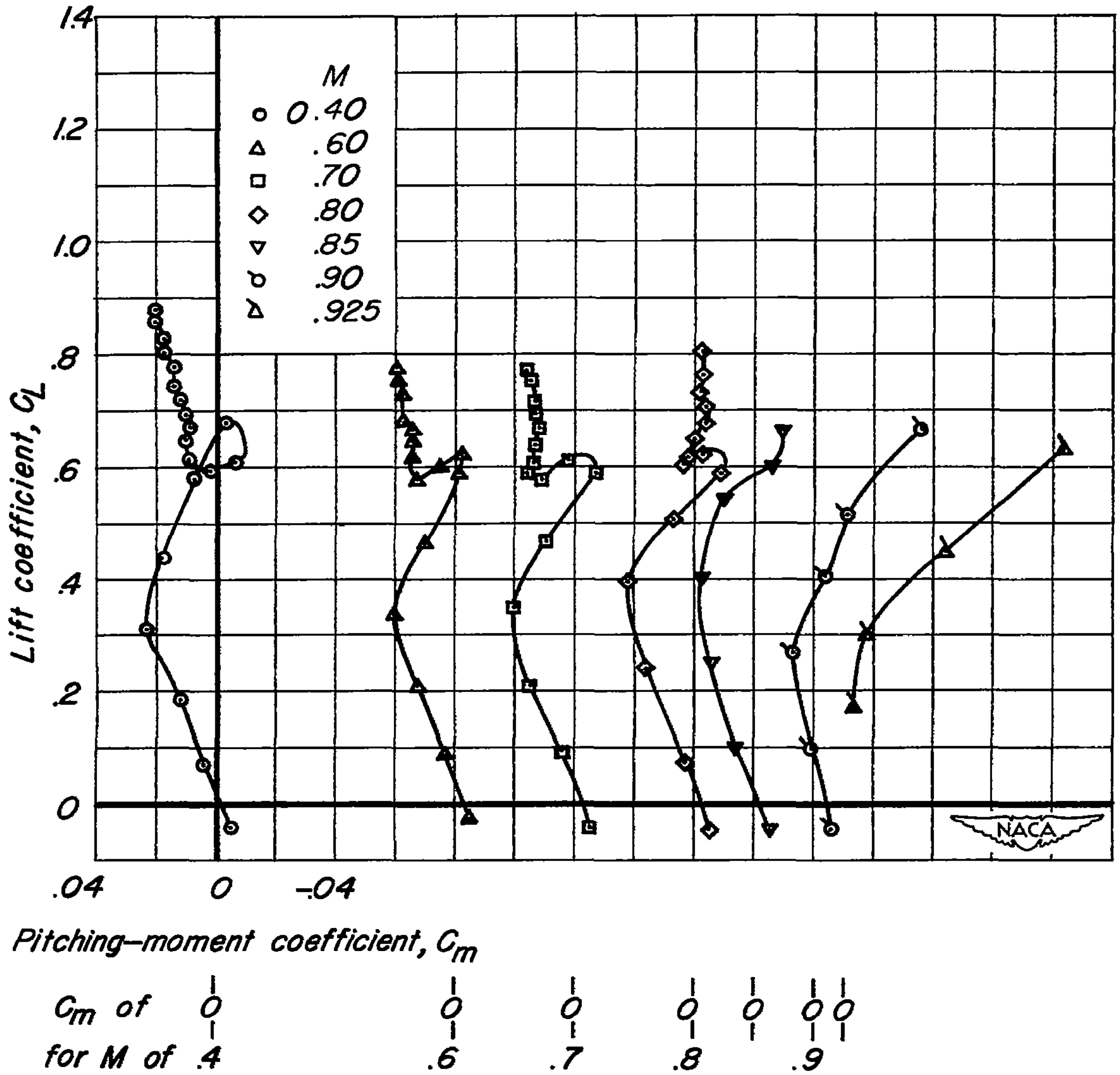

(b) Pitching-moment characteristics.

Figure 10.– Continued.

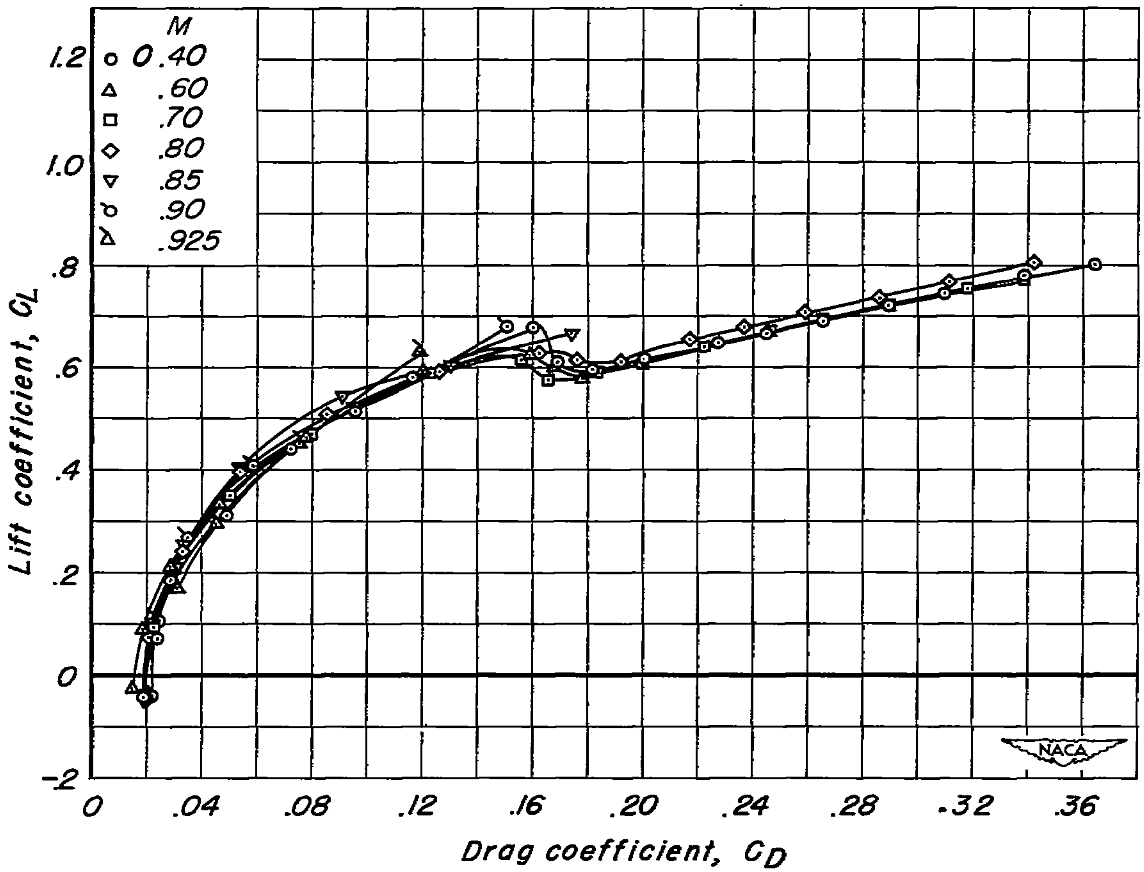

(c) Drag characteristics.

Figure 10.- Concluded.

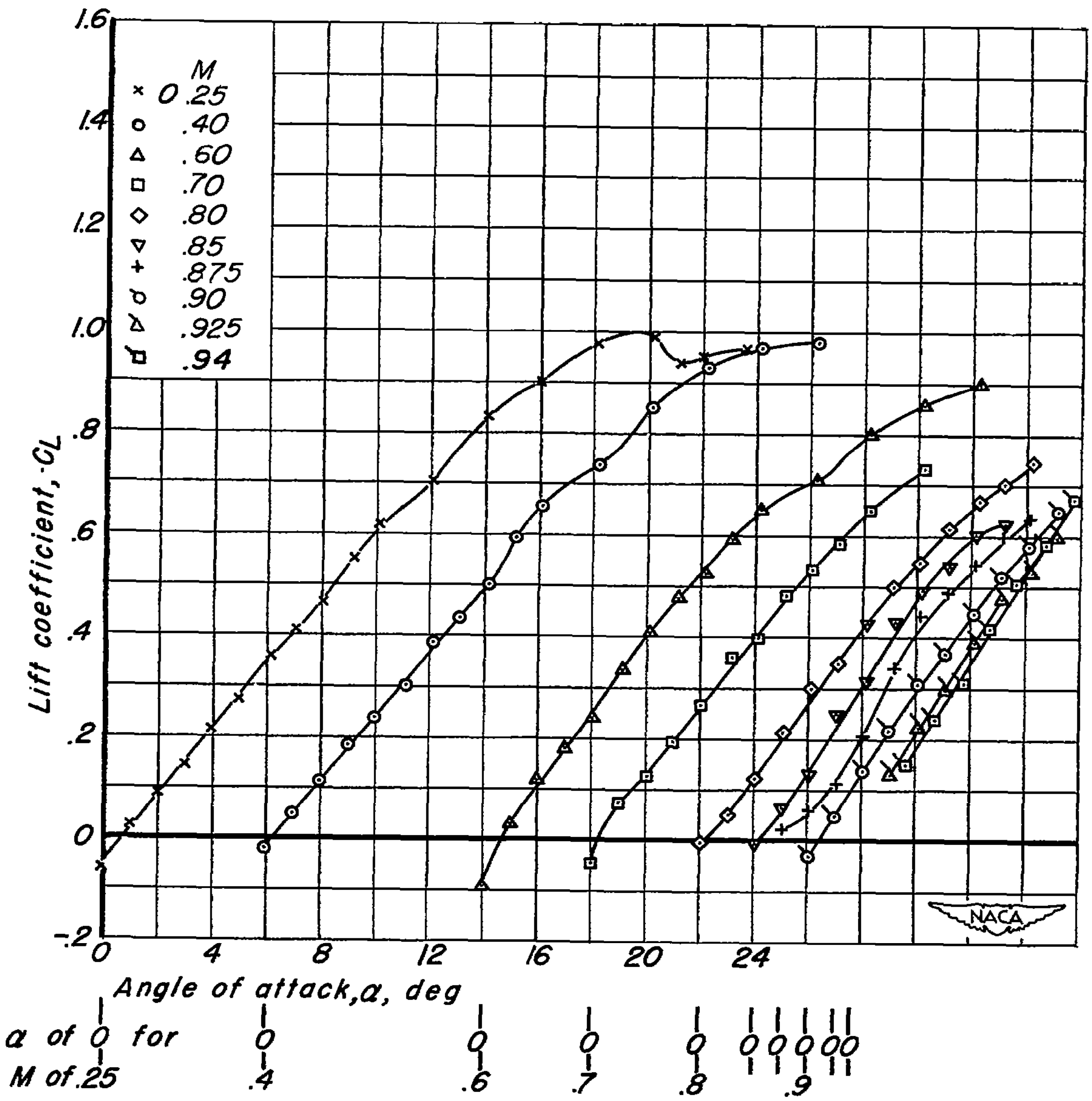

(a) Lift characteristics.

Figure 11.– The aerodynamic characteristics of the MX-656 model with the nose fins in the normal position. i_t, 0°.

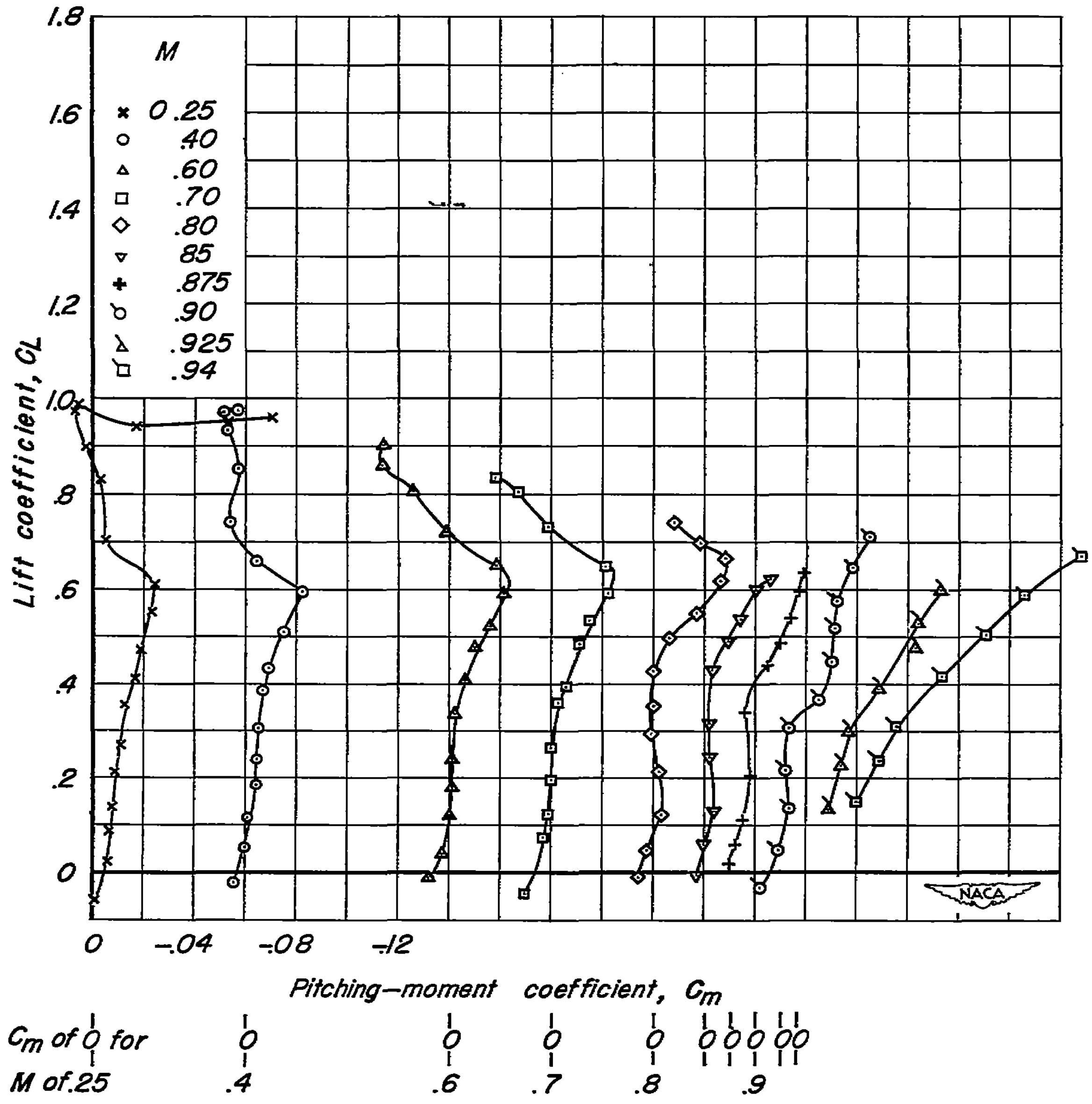

(b) Pitching-moment characteristics.

Figure 11.— Concluded.

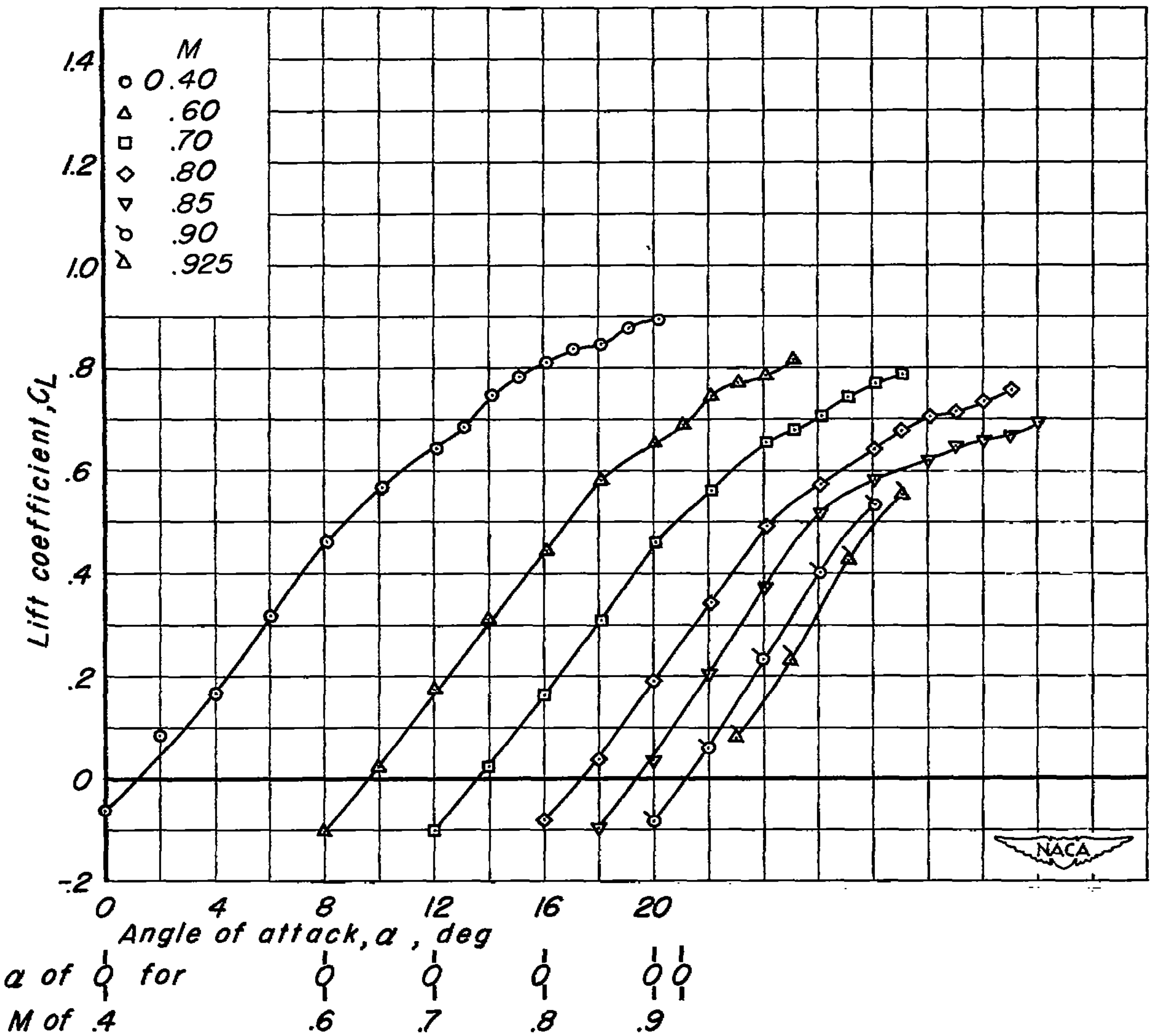

(a) Lift characteristics.

Figure 12.– The aerodynamic characteristics of the MX-656 model with the nose fins in the normal position. i_t, –5°.

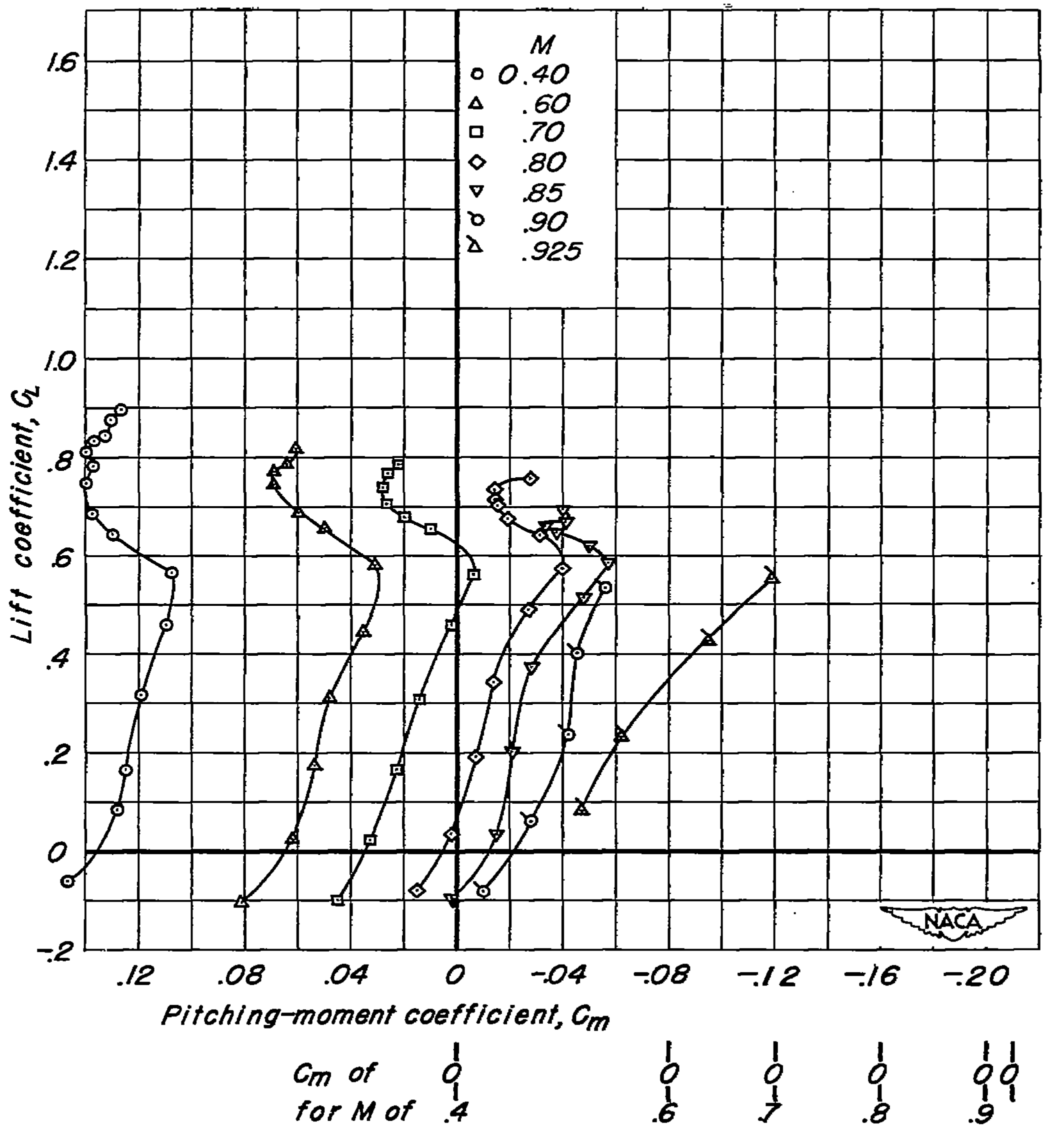

(b) Pitching-moment characteristics.

Figure 12.- Continued.

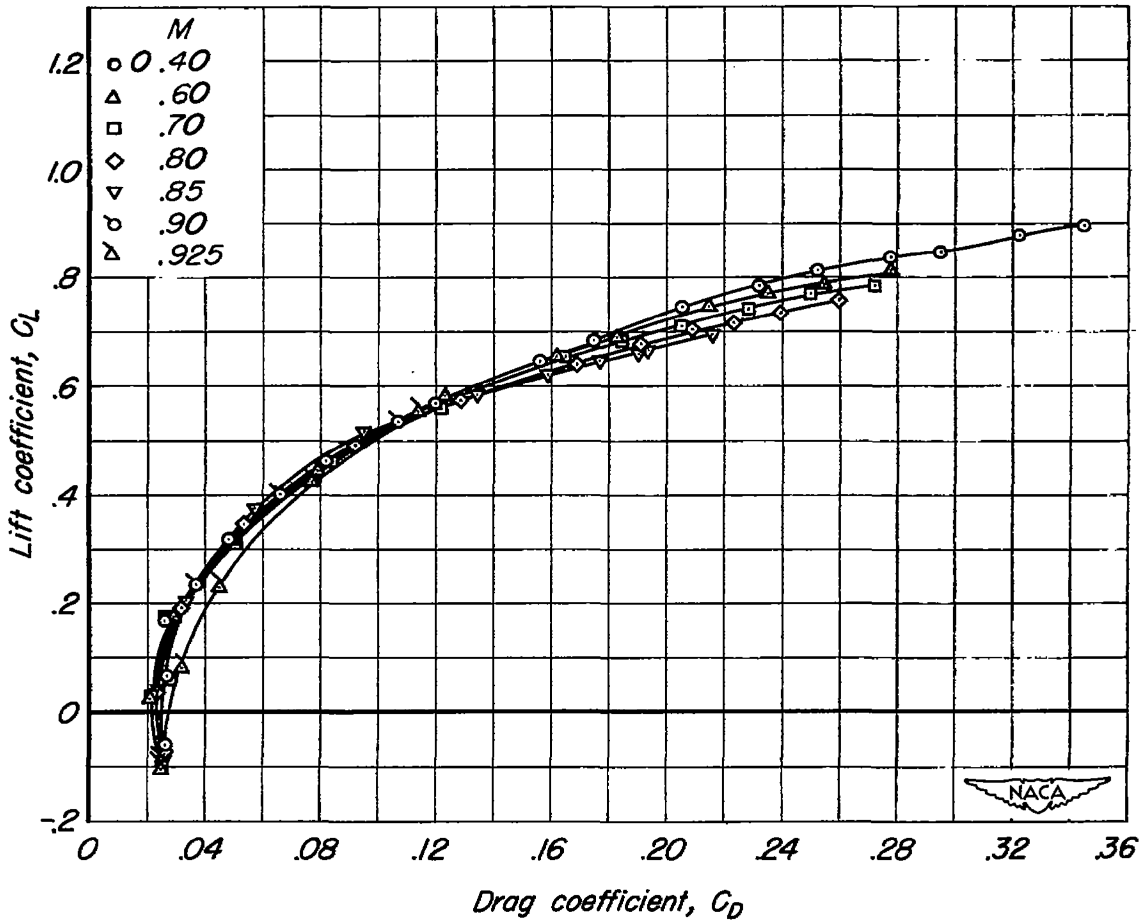

(c) Drag characteristics.

Figure 12.— Continued.

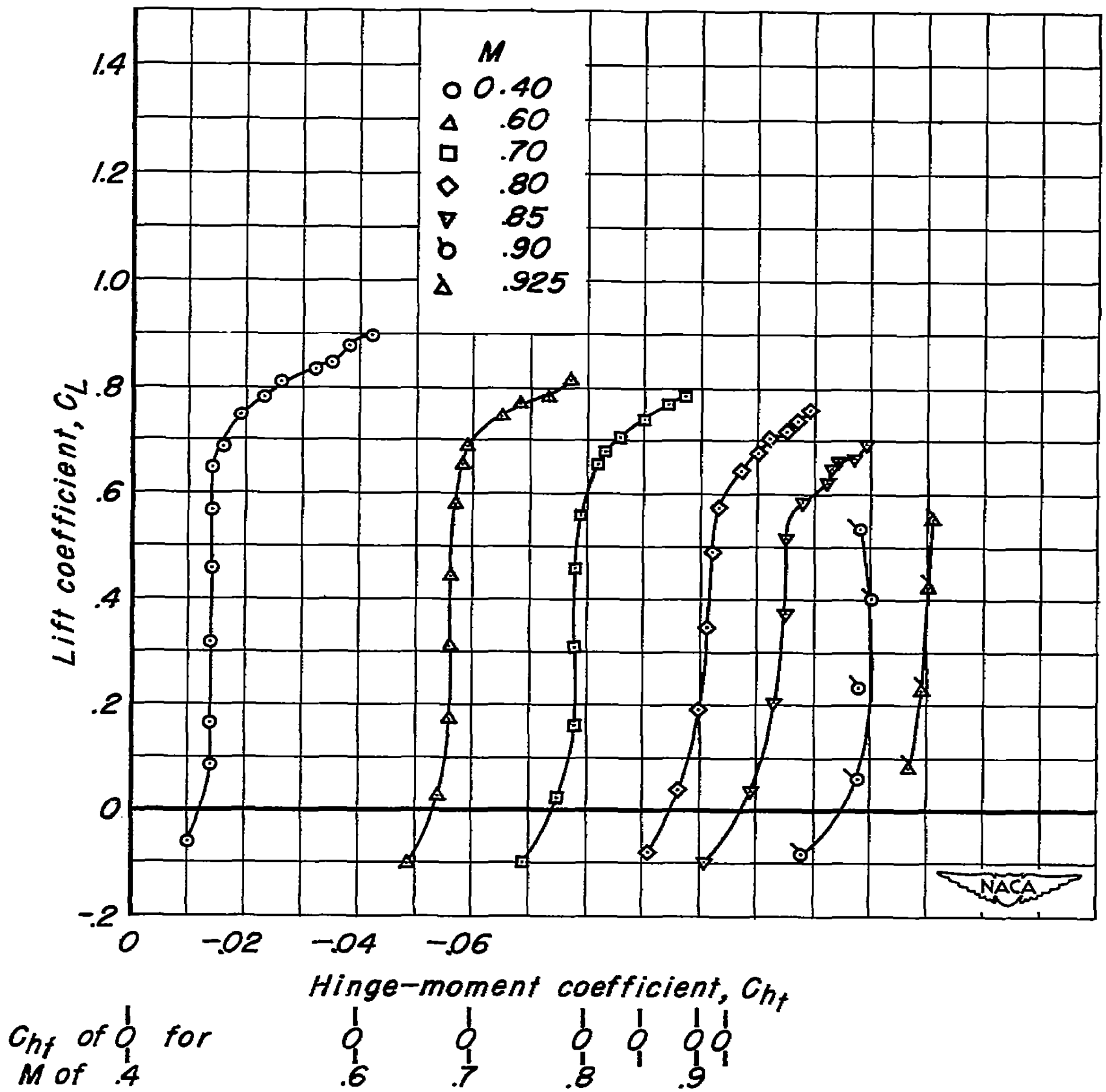

(d) Horizontal-tail hinge-moment characteristics.

Figure 12.– Concluded.

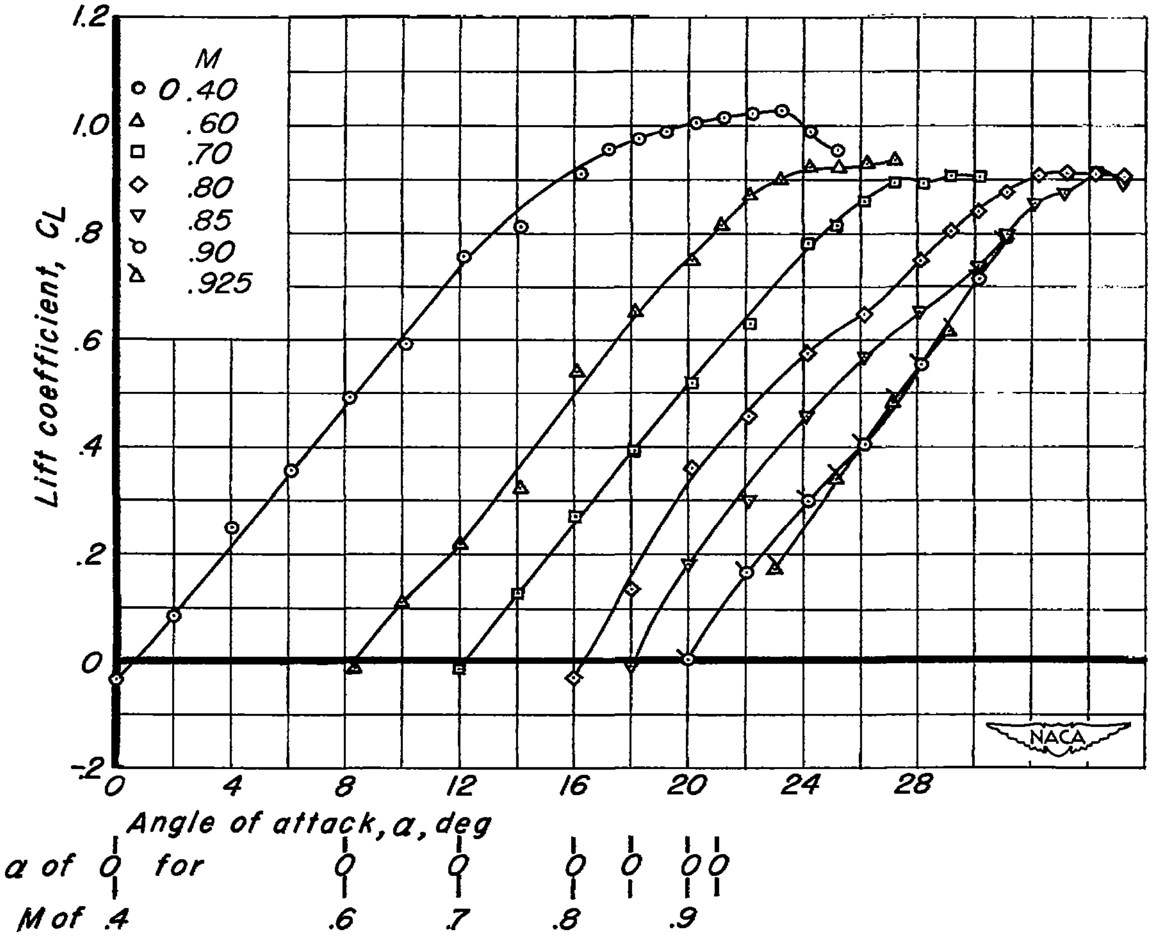

(a) Lift characteristics.

Figure 13.- The aerodynamic characteristics of the MX-656 model with the nose fins in the normal position. δ_{lf}, 10°.

[redacted]

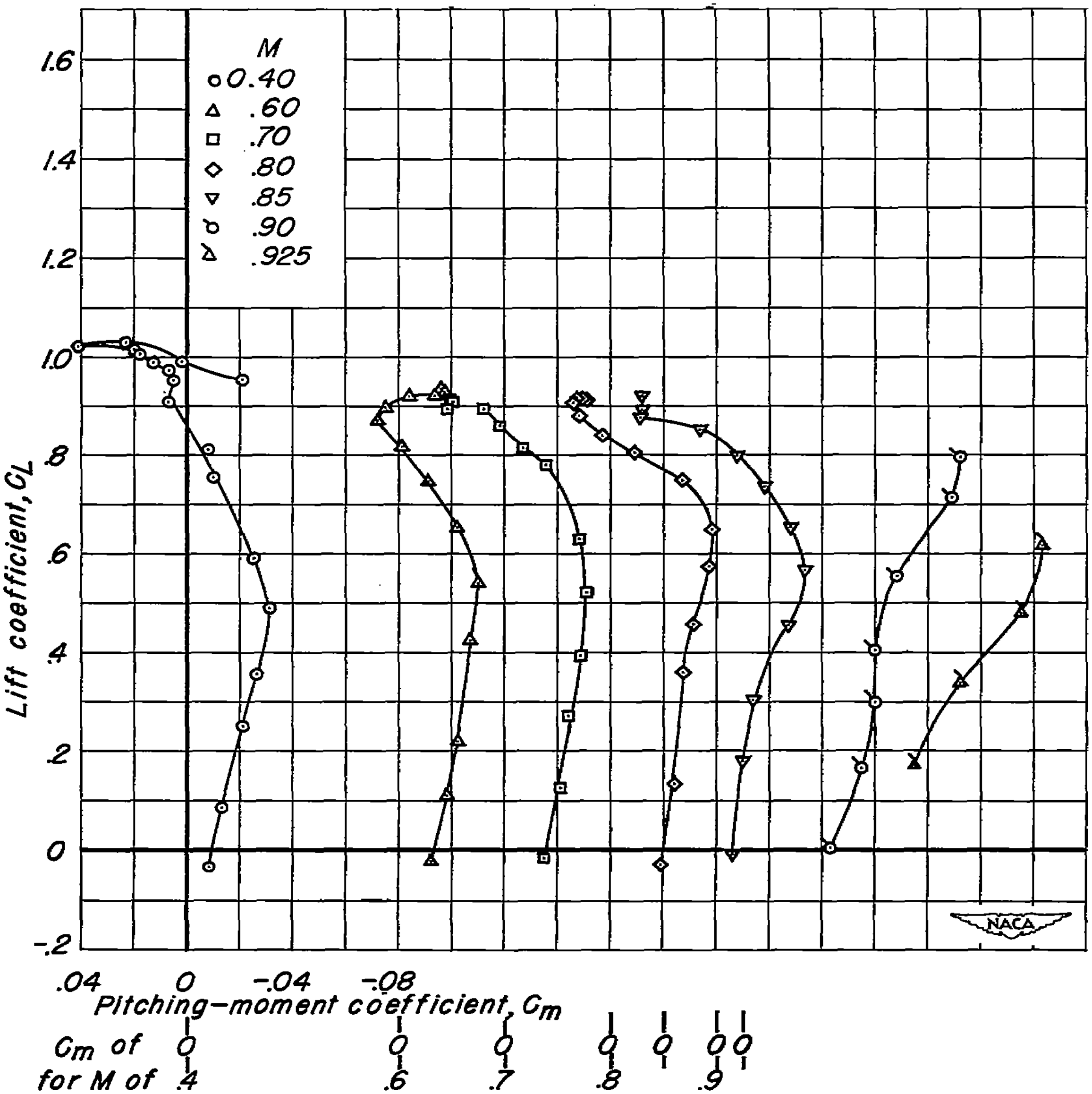

(b) Pitching-moment characteristics.

Figure 13.- Continued.

[redacted]

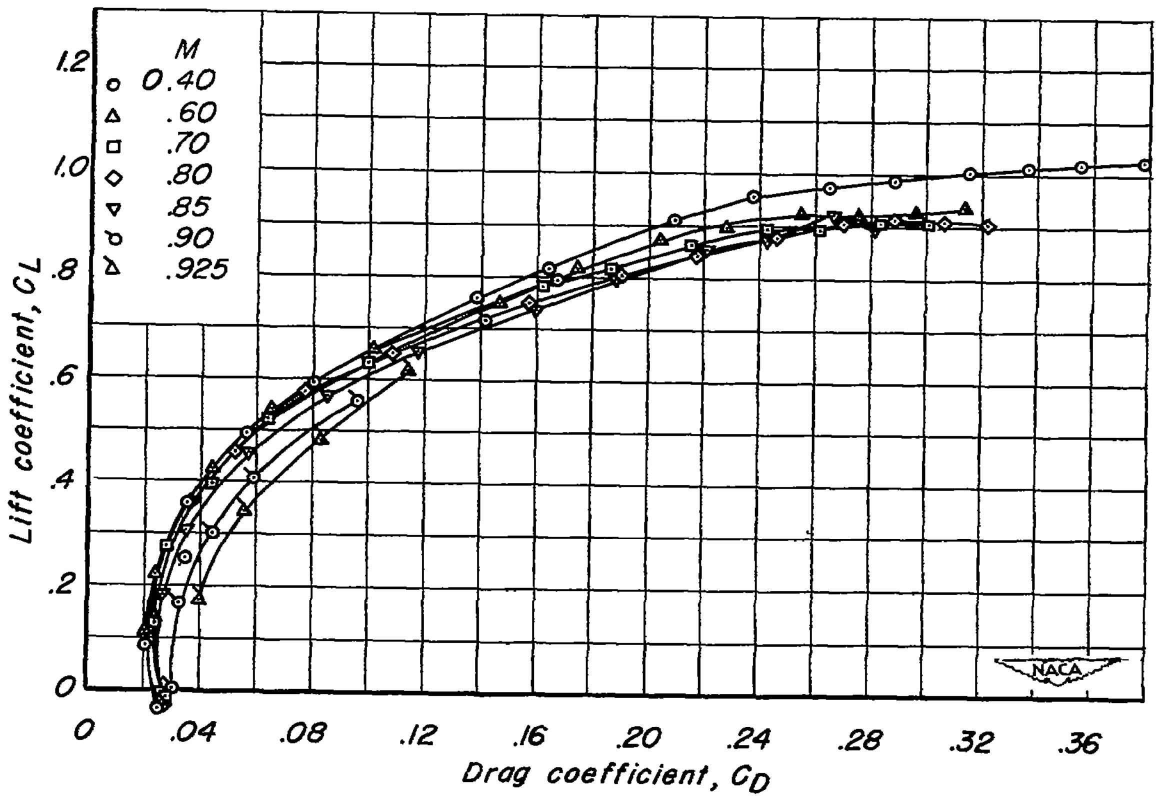

(c) Drag characteristics.

Figure 13.– Concluded.

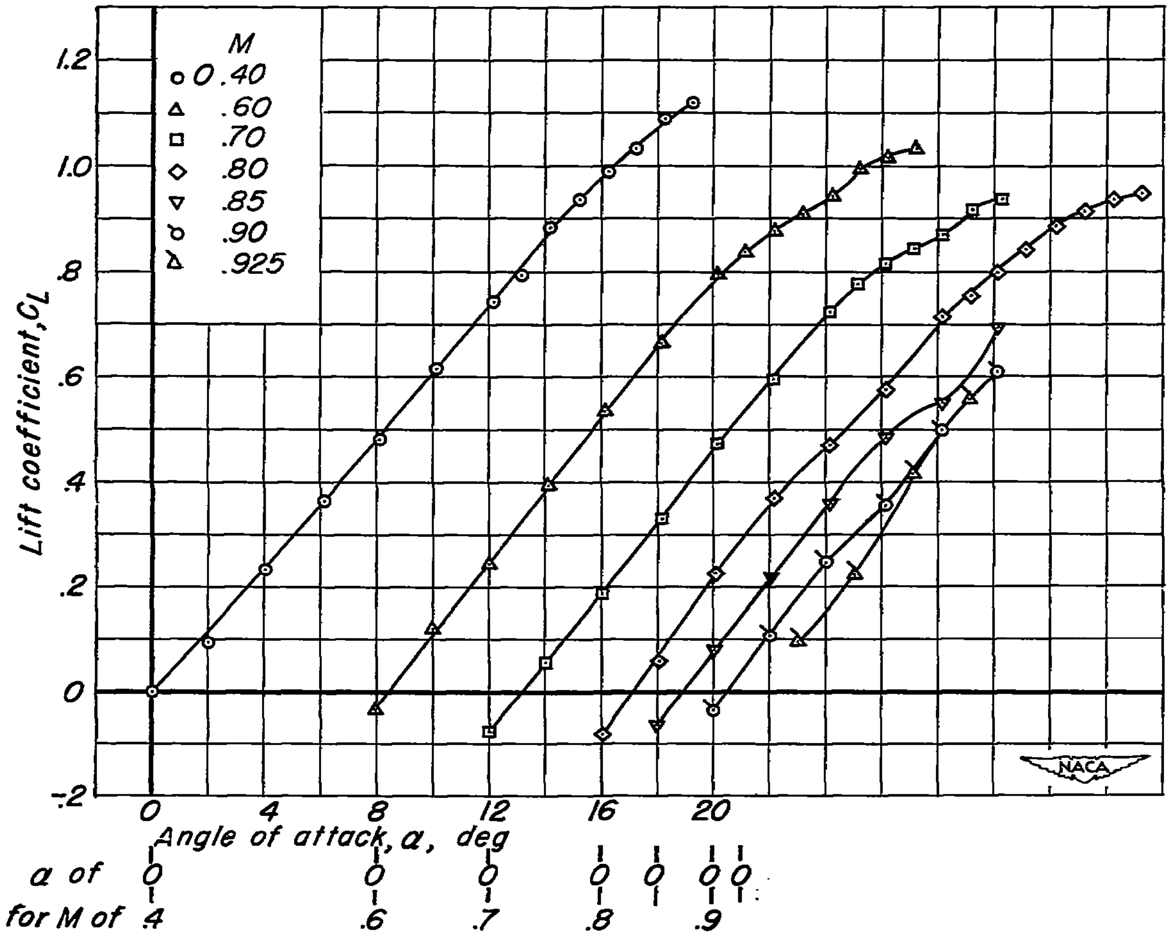

(a) Lift characteristics.

Figure 14.– The aerodynamic characteristics of the MX-656 model with the nose fins in the normal position. δ_{lf}, 20°.

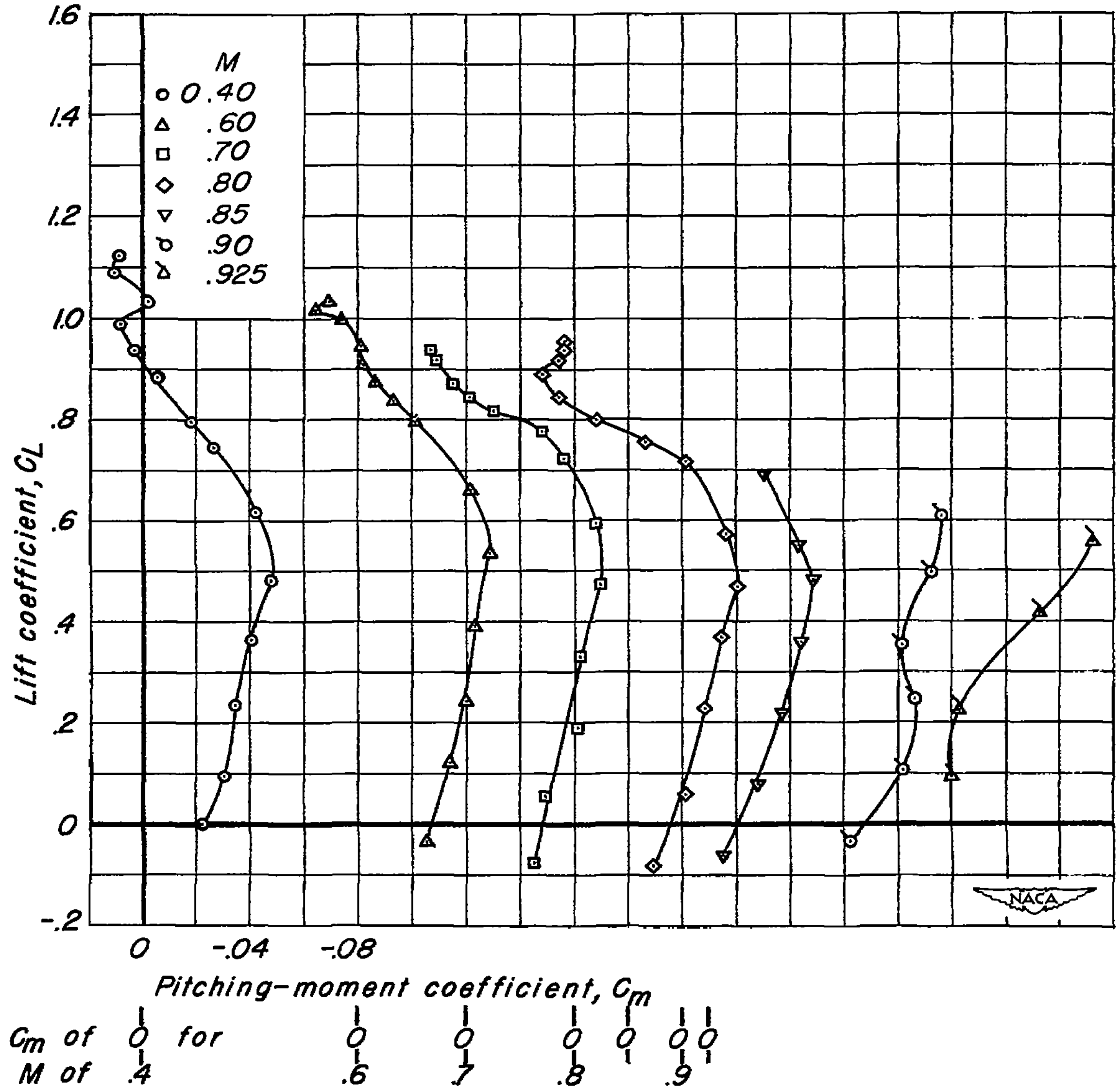

(b) Pitching-moment characteristics.

Figure 14.- Continued.

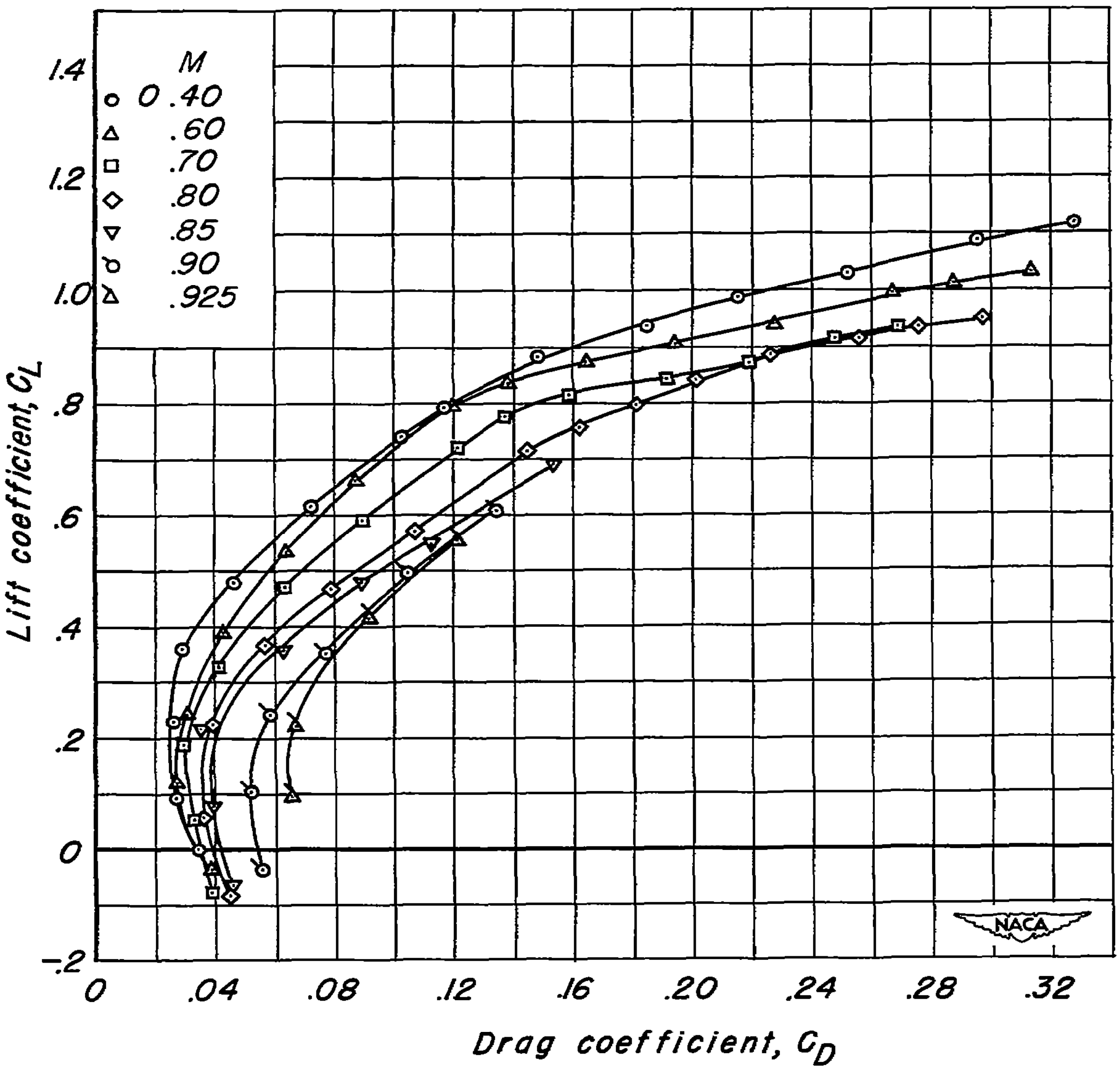

(c) Drag characteristics.

Figure 14.– Concluded.

[redacted]

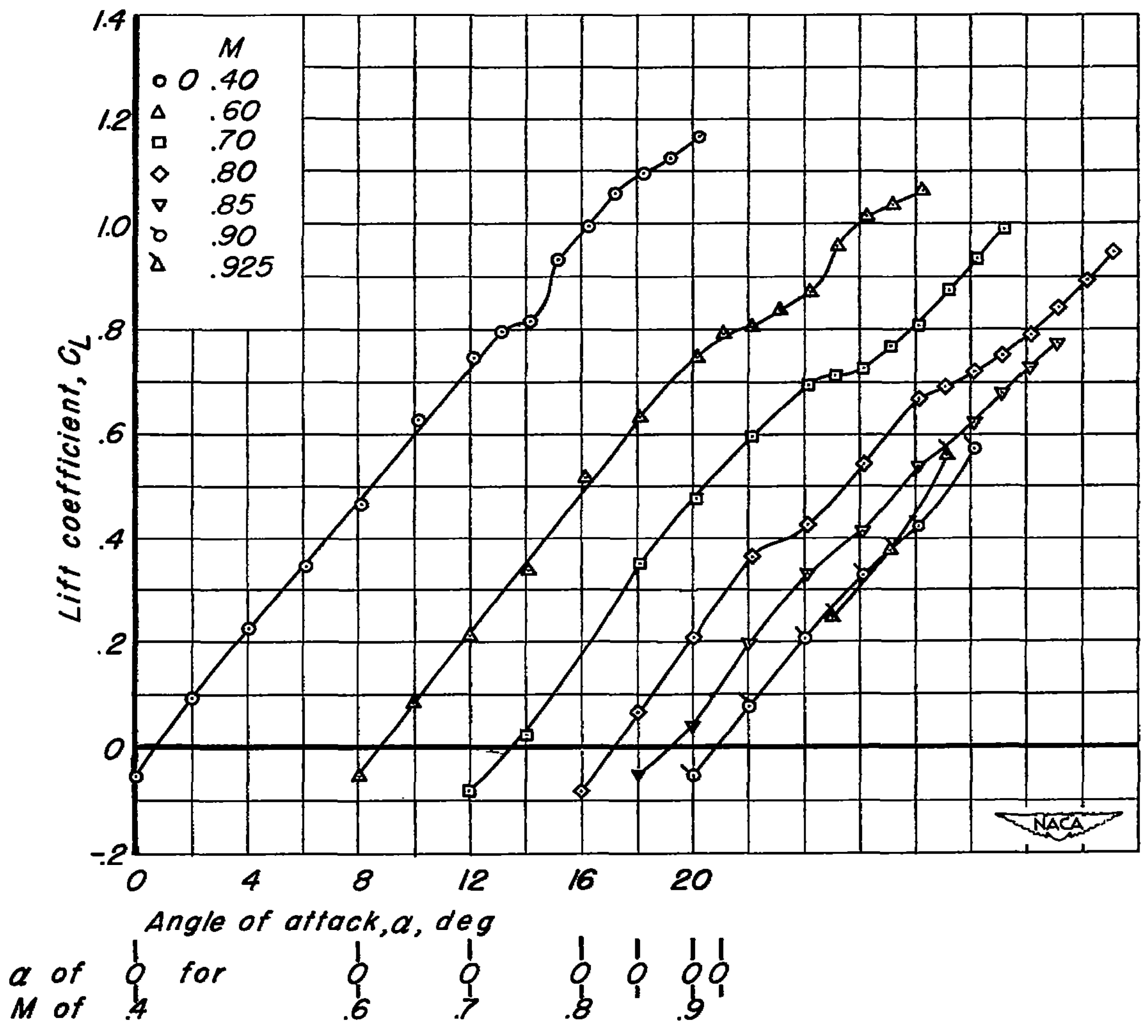

(a) Lift characteristics.

Figure 15.– The aerodynamic characteristics of the MX-656 model with the nose fins in the normal position. δ_{lf}, 30°.

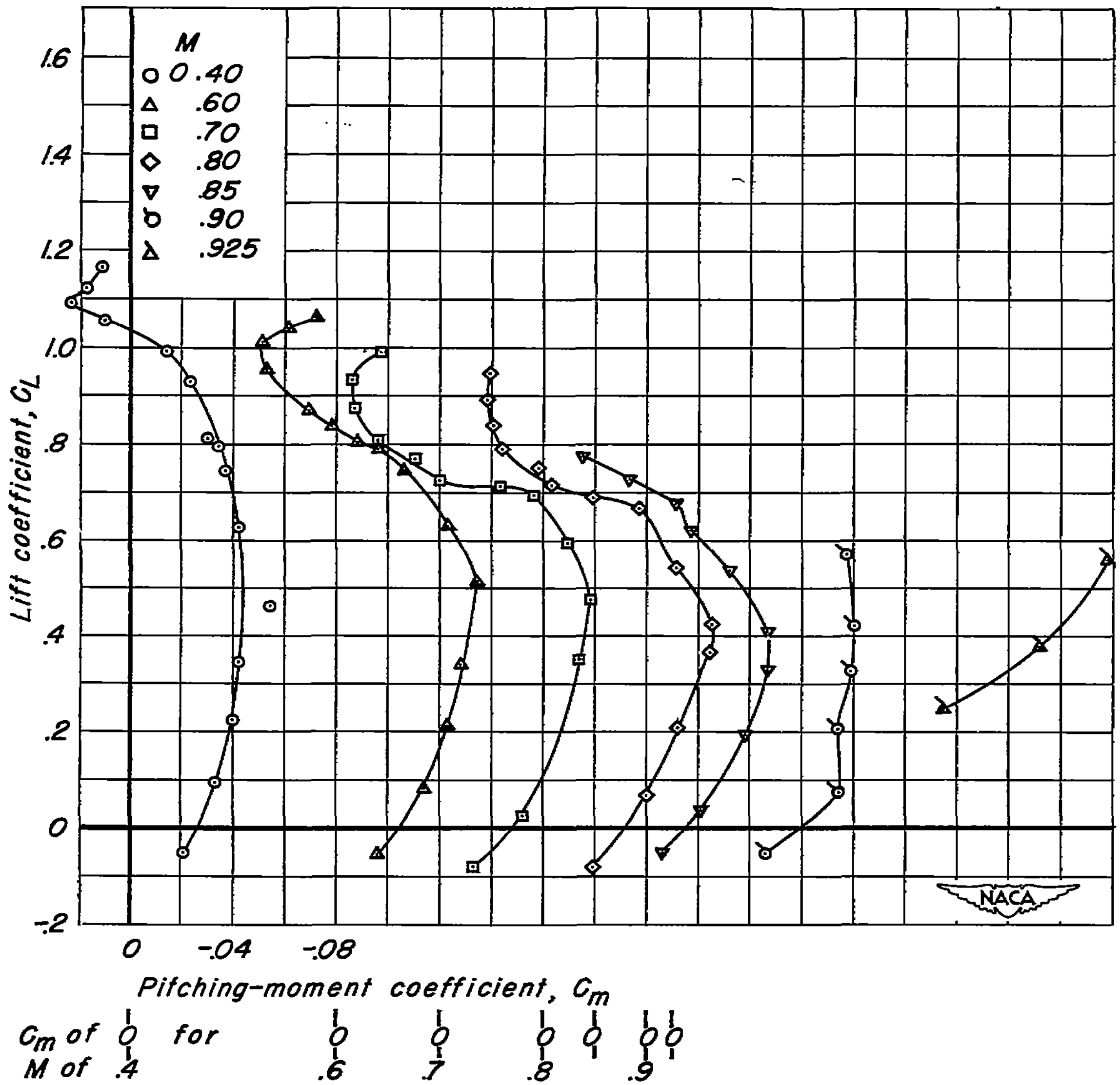

(b) Pitching-moment characteristics.

Figure 15.- Continued.

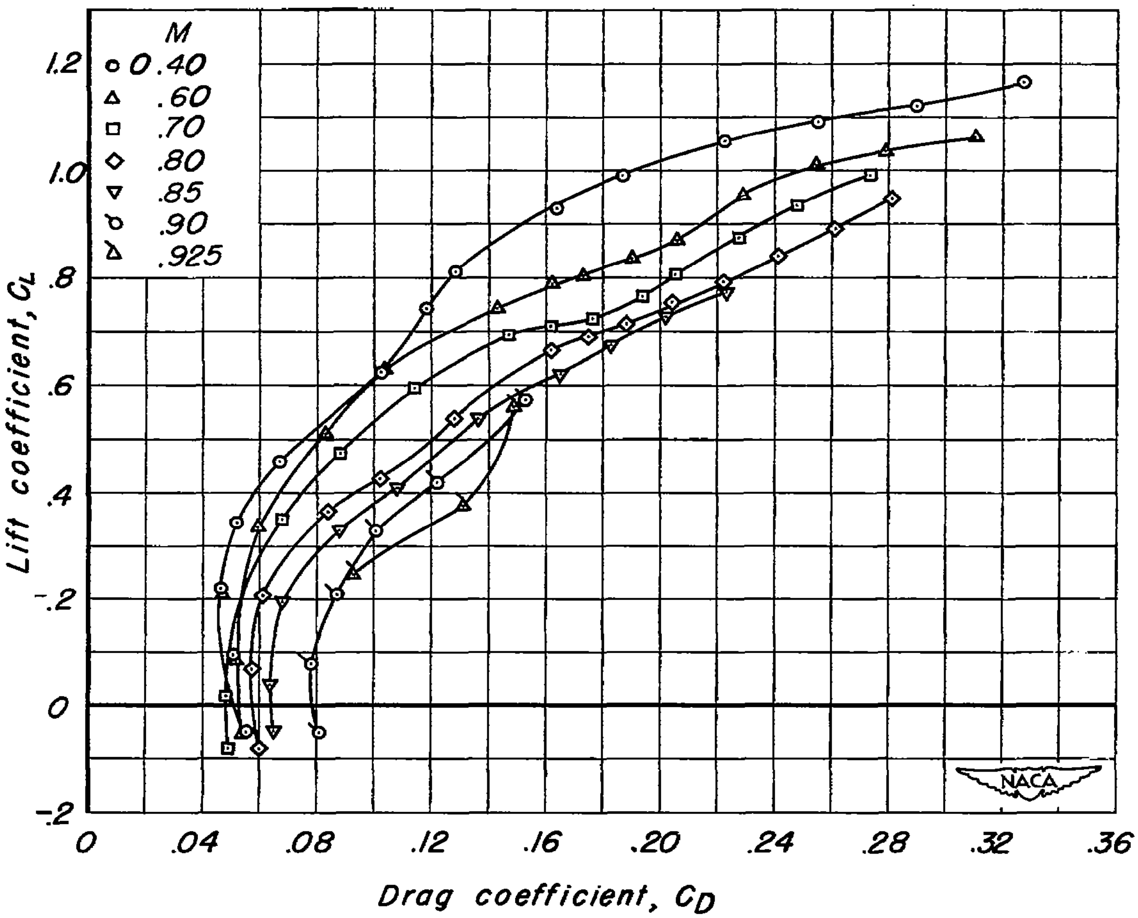

(c) Drag characteristics.

Figure 15.– Concluded.

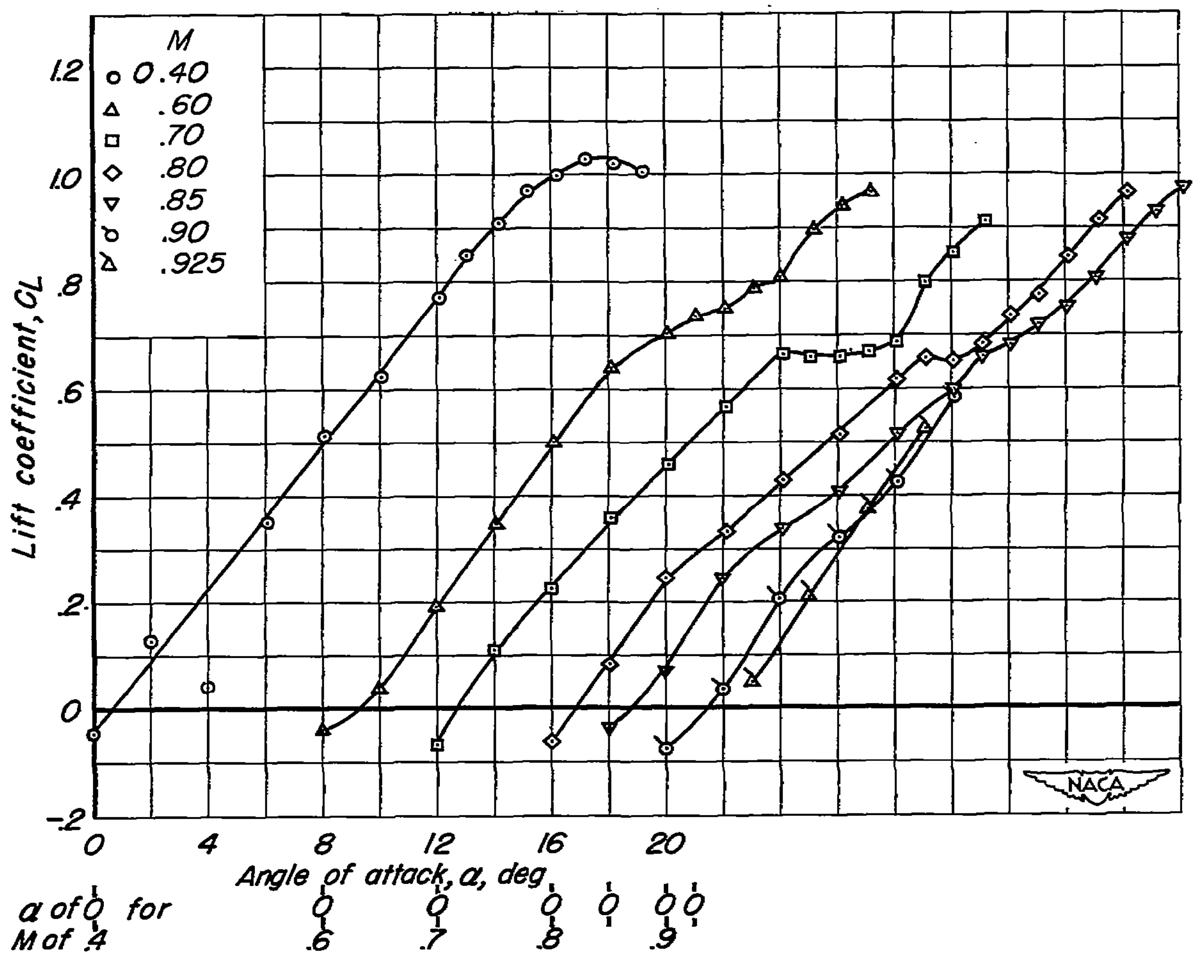

(a) Lift characteristics.

Figure 16.– The aerodynamic characteristics of the MX-656 model without the nose fins. δ_{lf}, 30°.

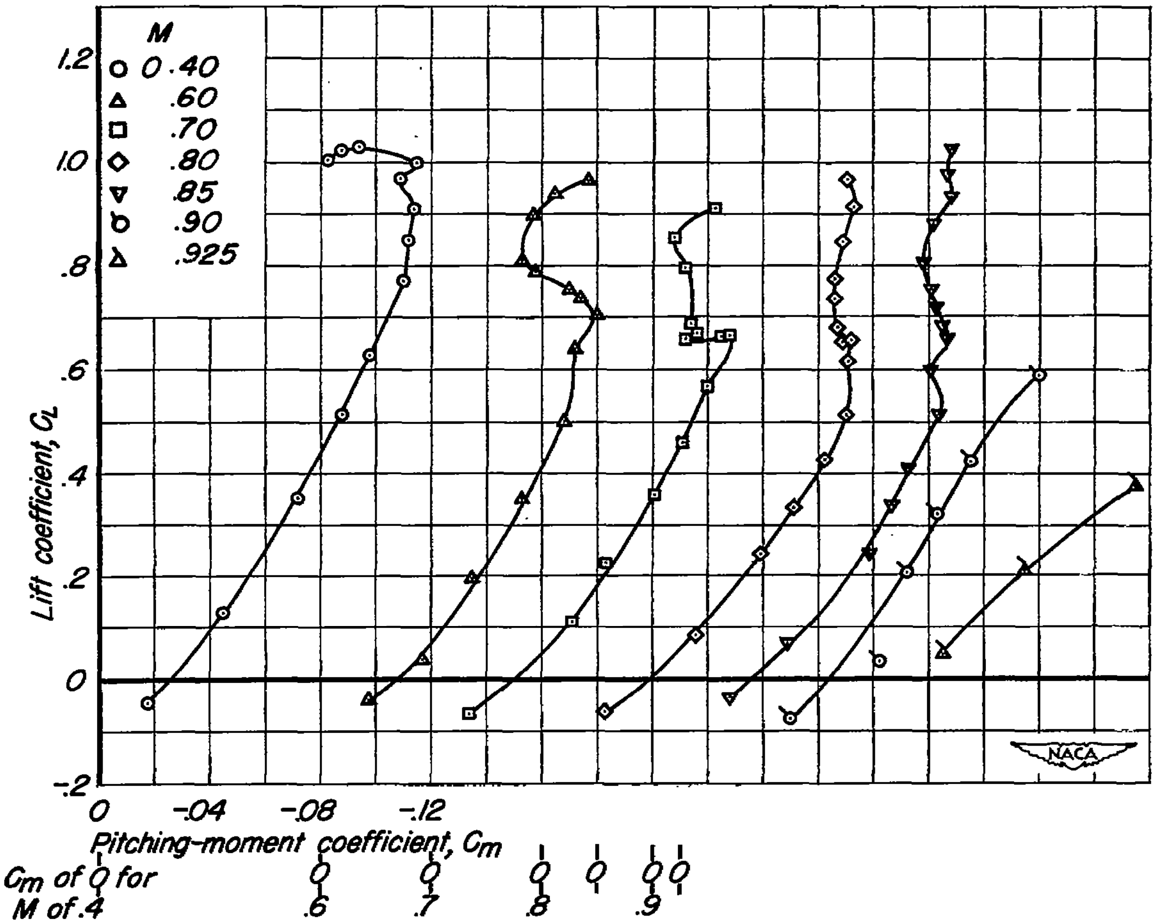

(b) Pitching-moment characteristics.

Figure 16.– Continued.

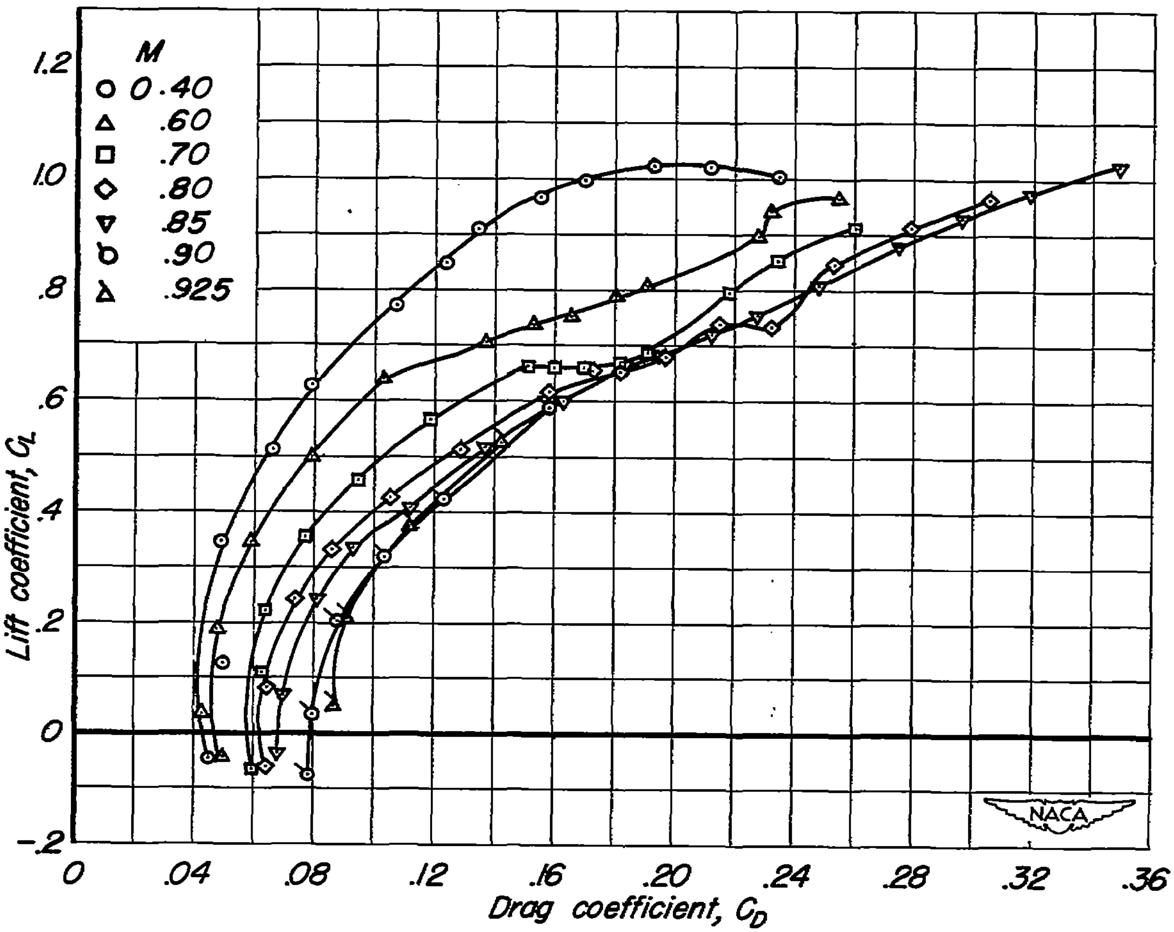

(c) Drag characteristics.

Figure 16- Concluded.

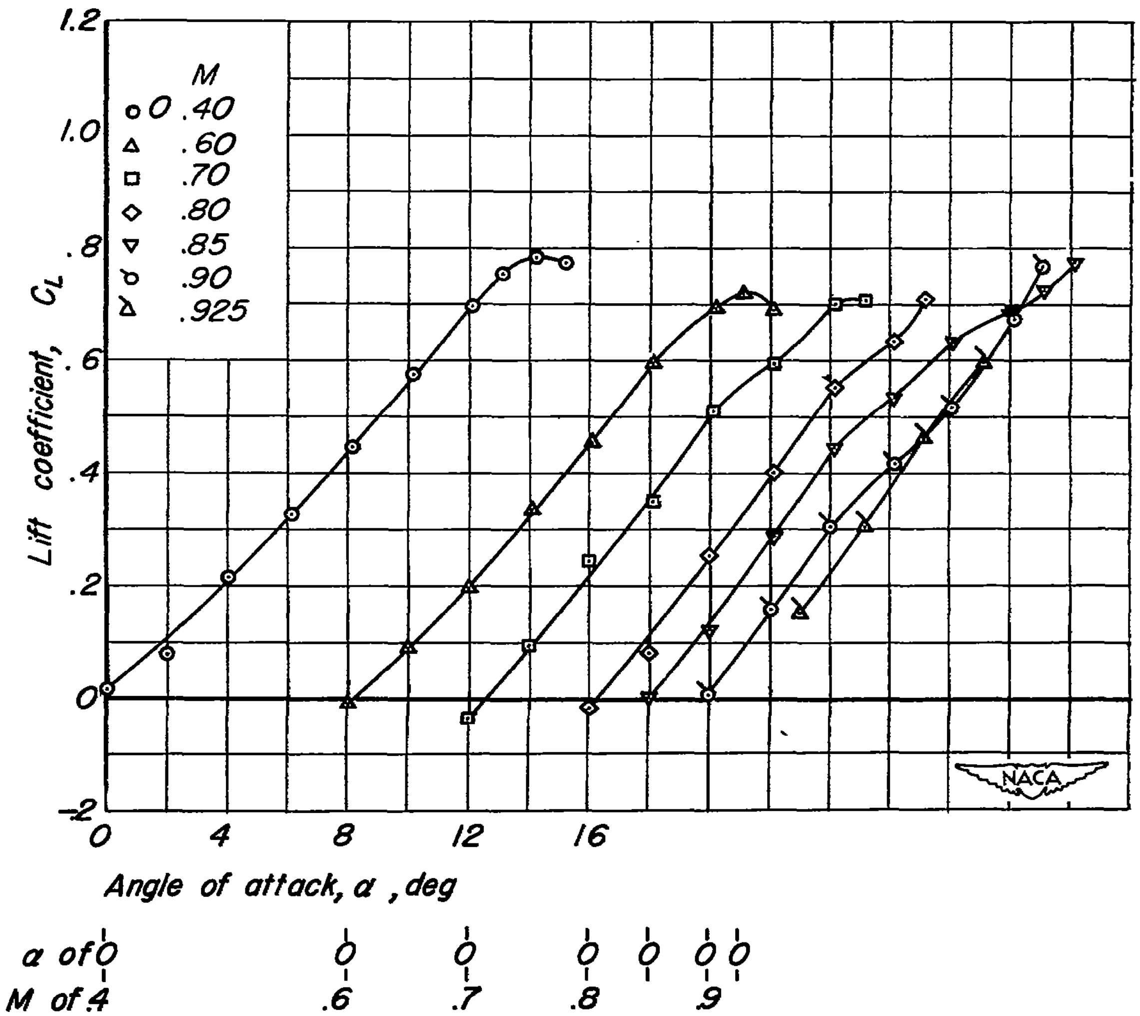

(a) Lift characteristics.

Figure 17.– The aerodynamic characteristics of the MX-656 model without the nose fins and the empennage. δ_{lf}, 10°.

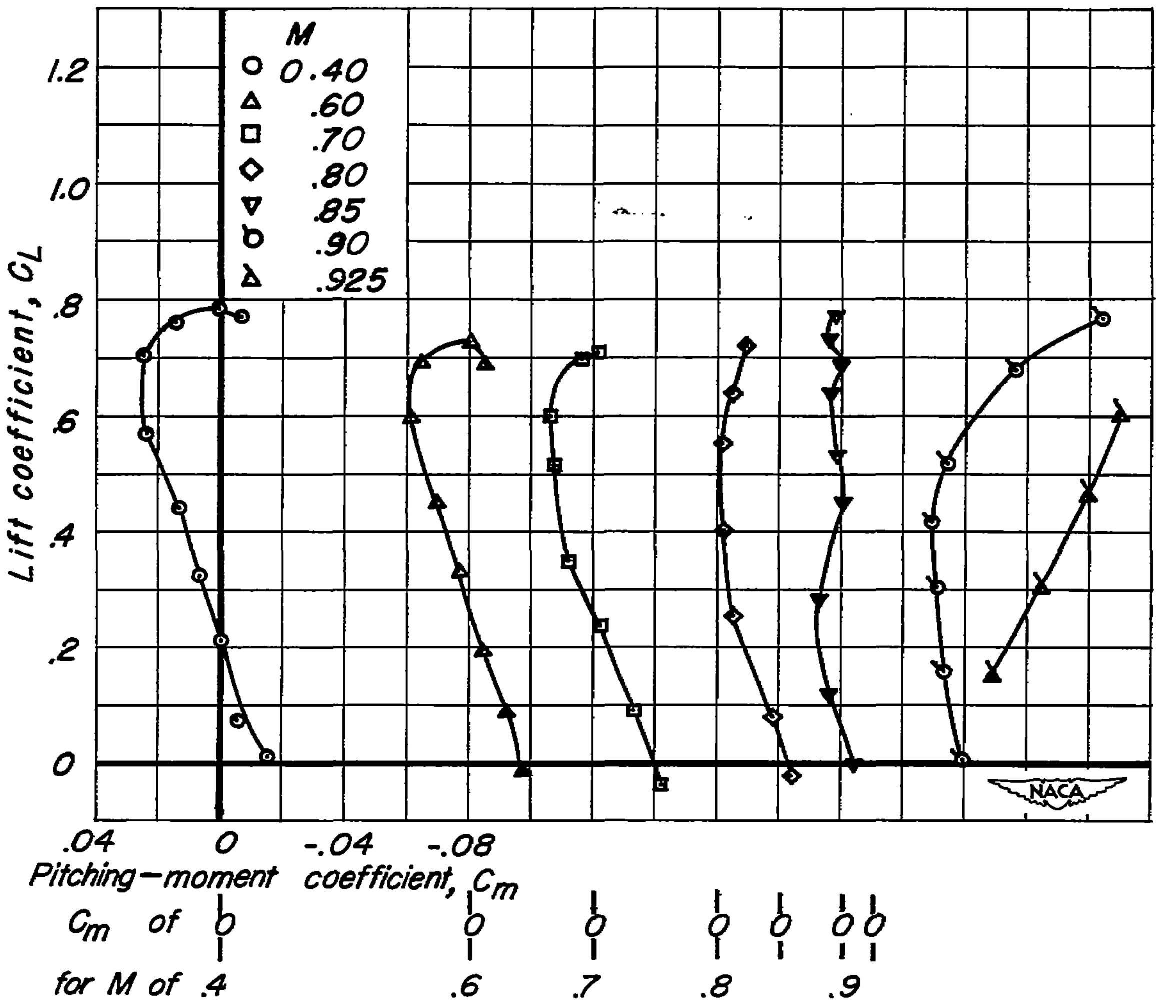

(b) Pitching-moment characteristics.

Figure 17- Continued.

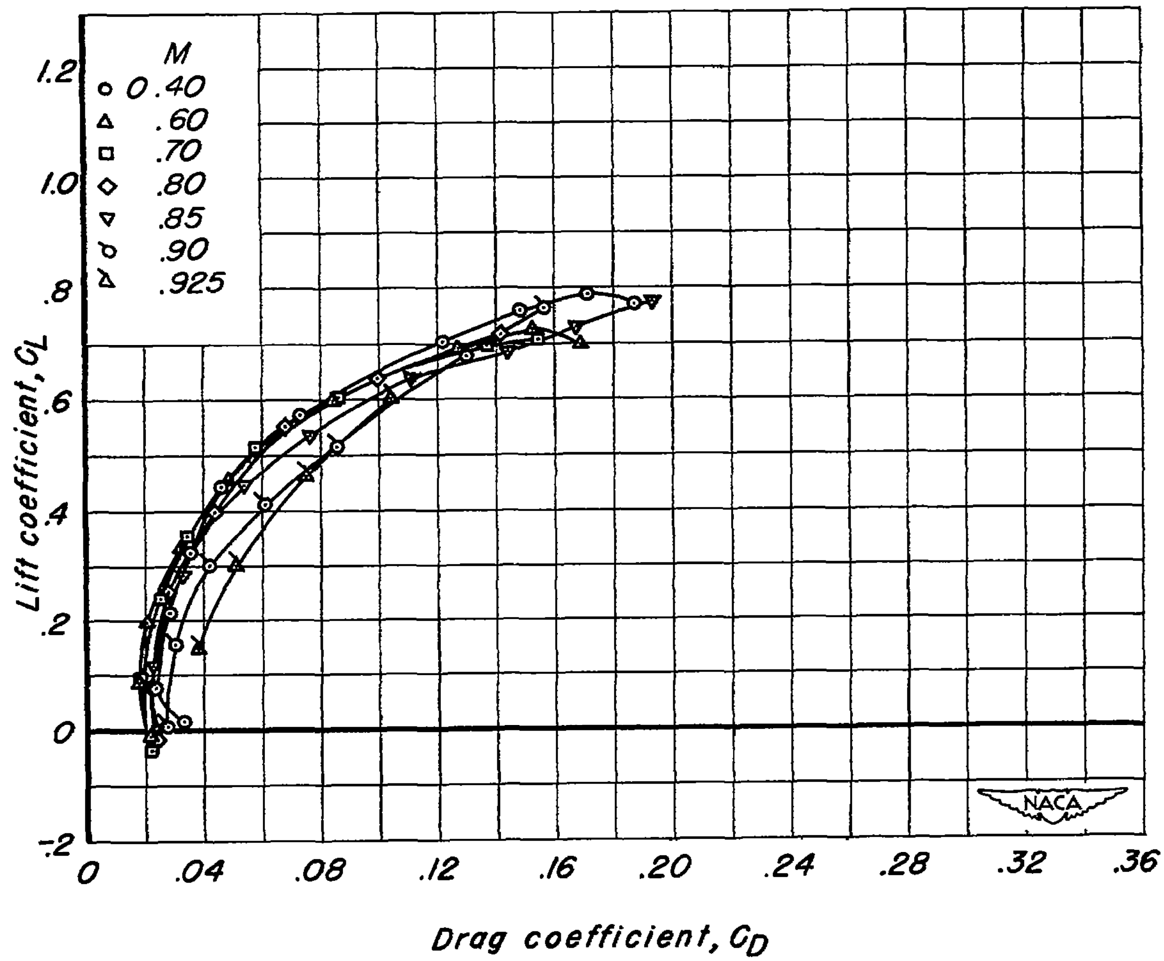

(c) Drag characteristics.

Figure 17.— Concluded.

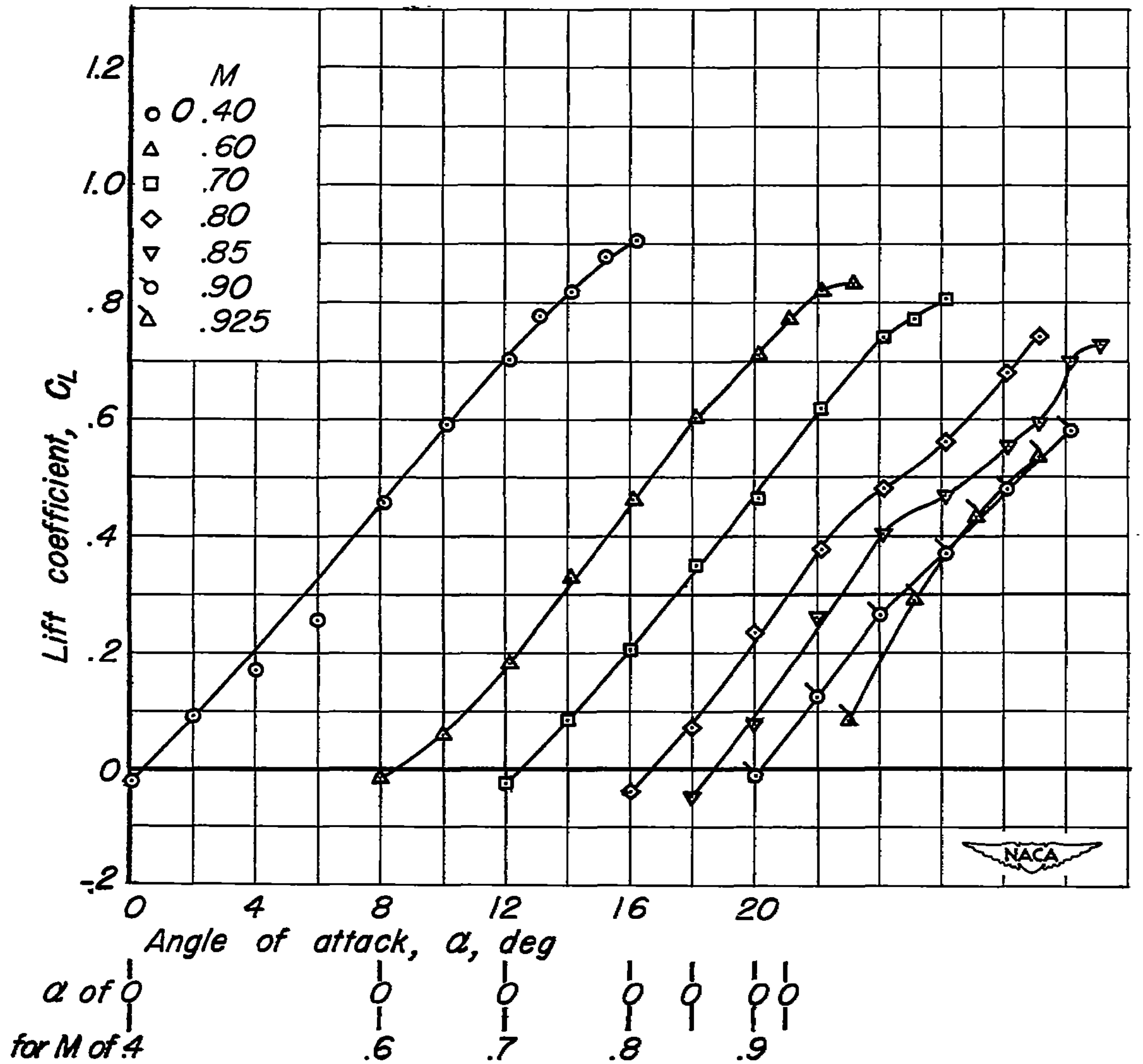

(a) Lift characteristics.

Figure 18.- The aerodynamic characteristics of the MX-656 model without the nose fins and the empennage. δ_{lf}, 20°

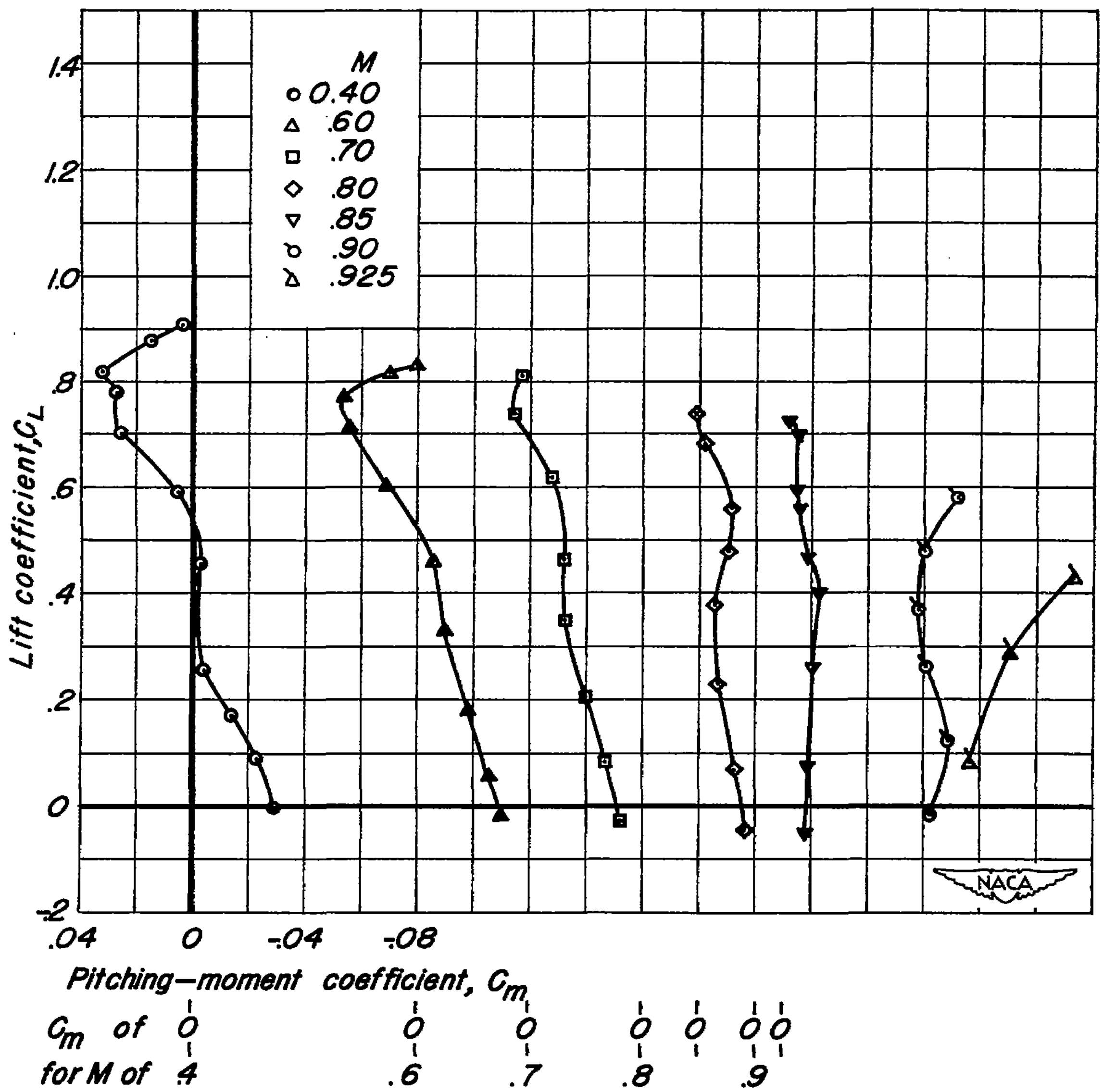

(b) Pitching-moment characteristics.

Figure 18.- Continued.

[redacted]

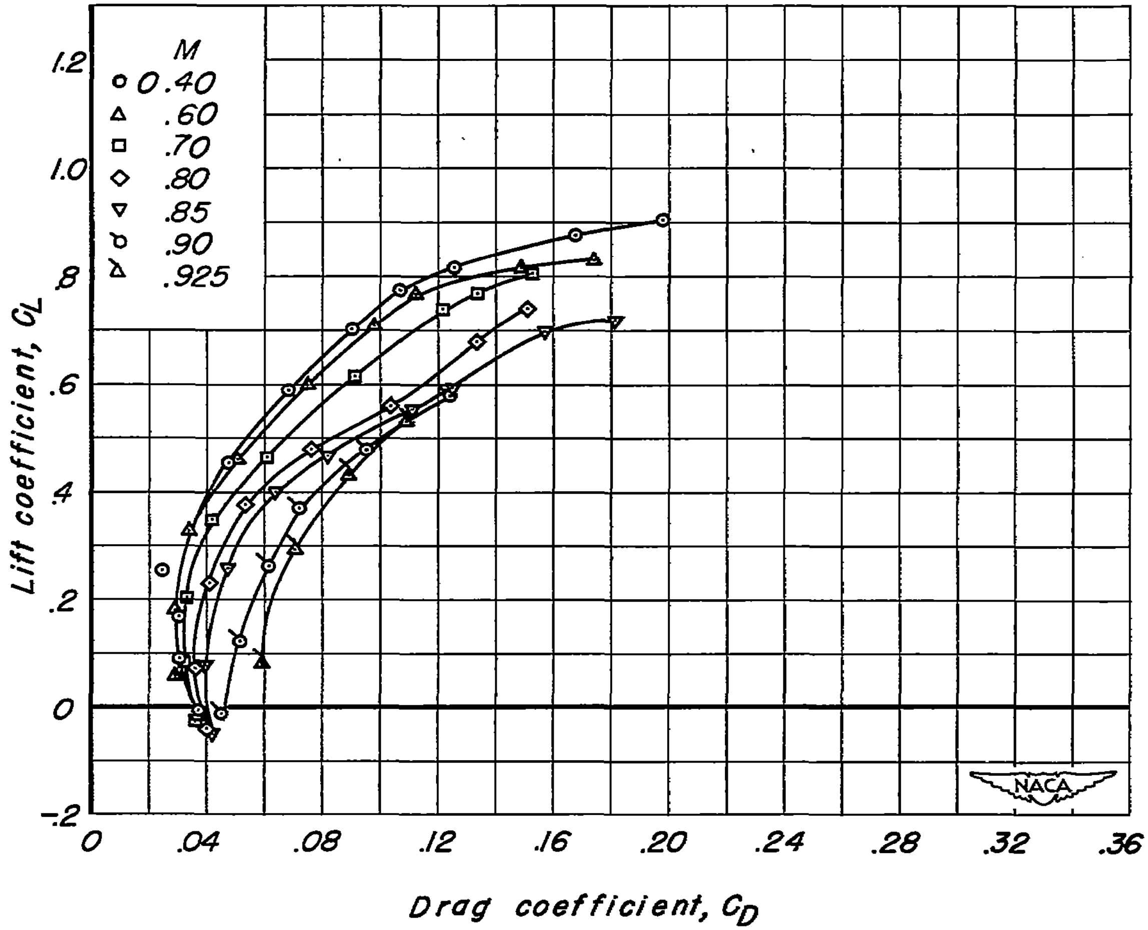

(c) Drag characteristics.

Figure 18.– Concluded.

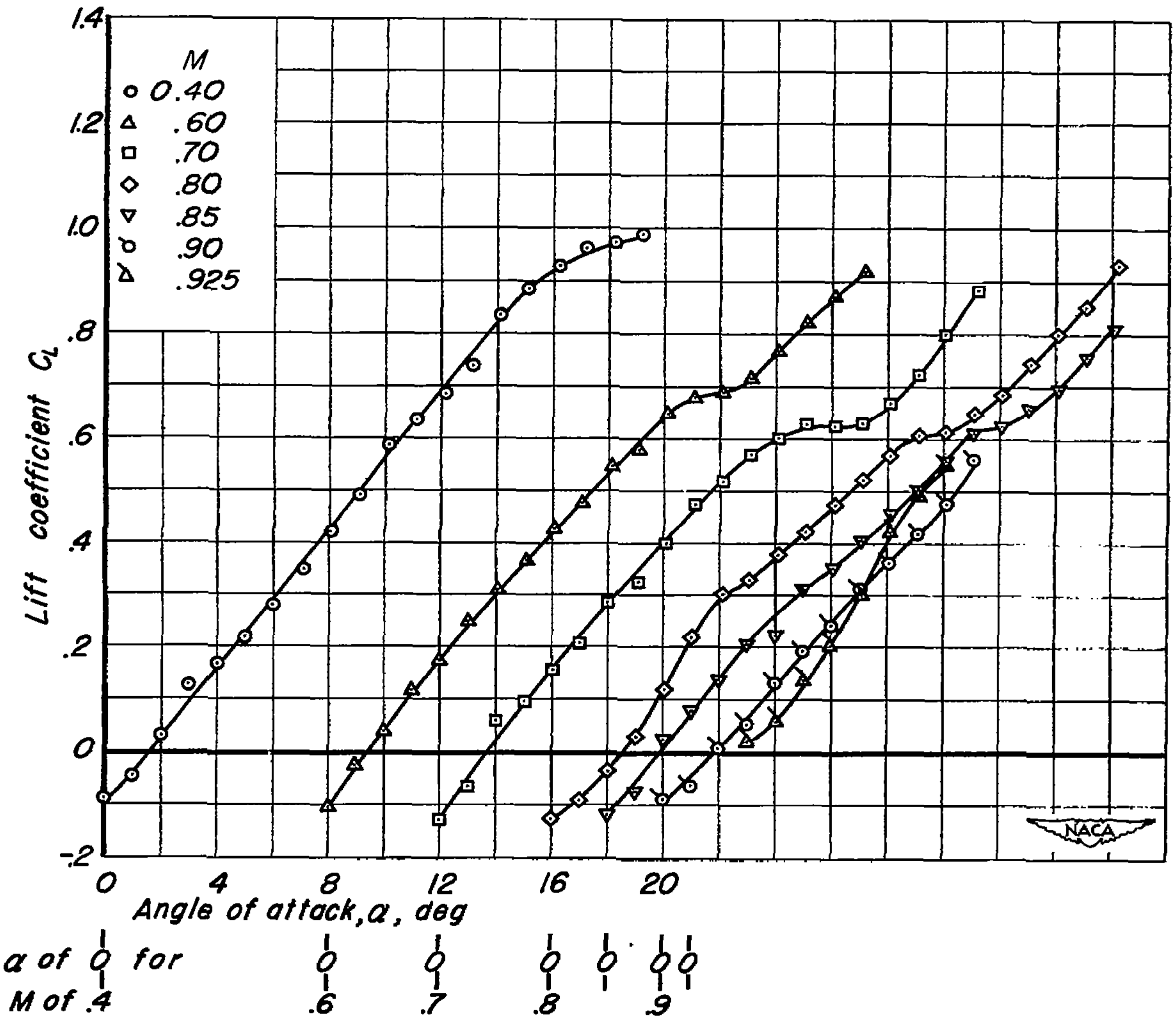

(a) Lift characteristics.

Figure 19.- The aerodynamic characteristics of the MX-656 model without the nose fins. i_t,−5°; δ_{lf},30°.

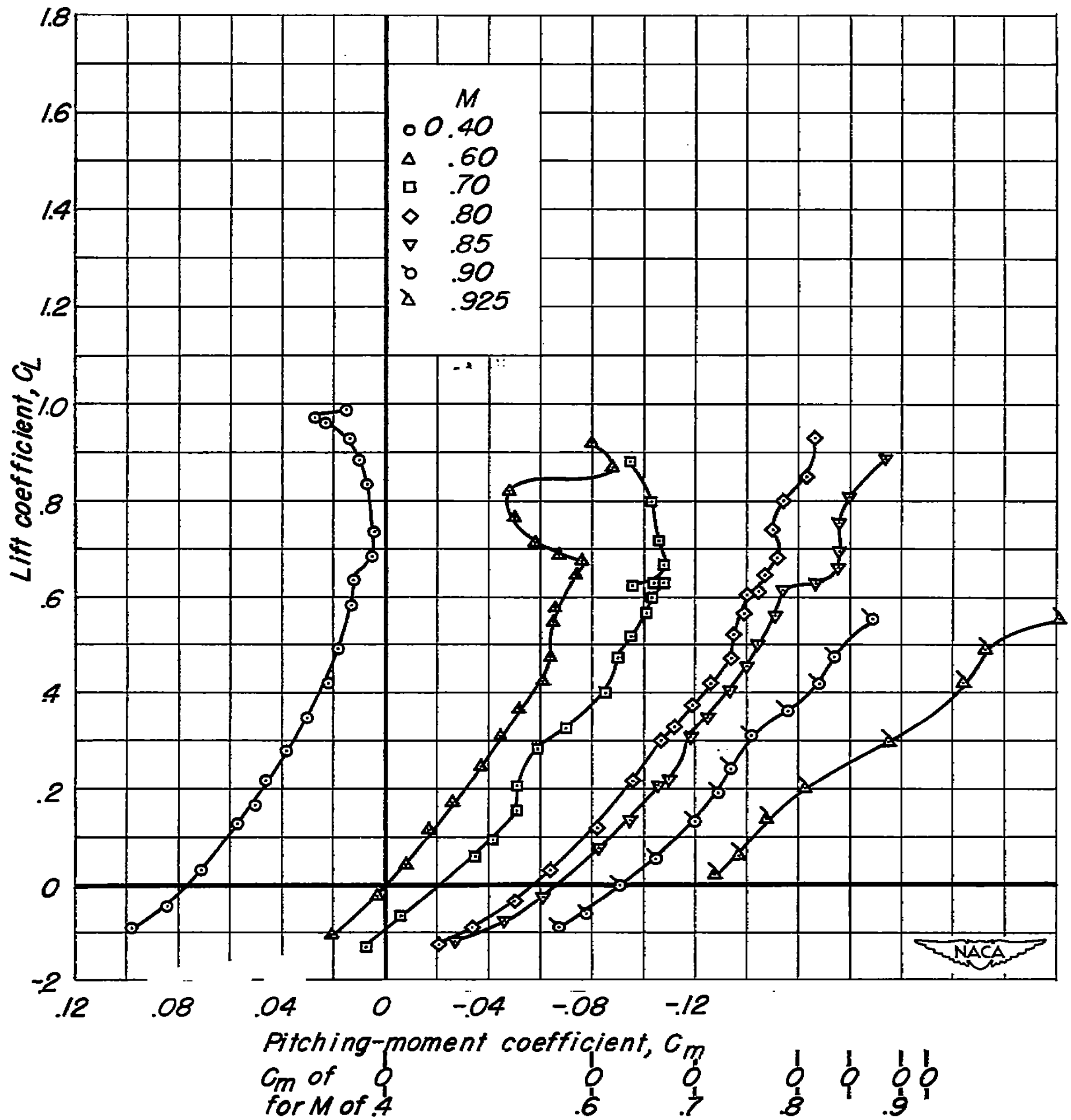

(b) Pitching-moment characteristics.

Figure 19.—Continued.

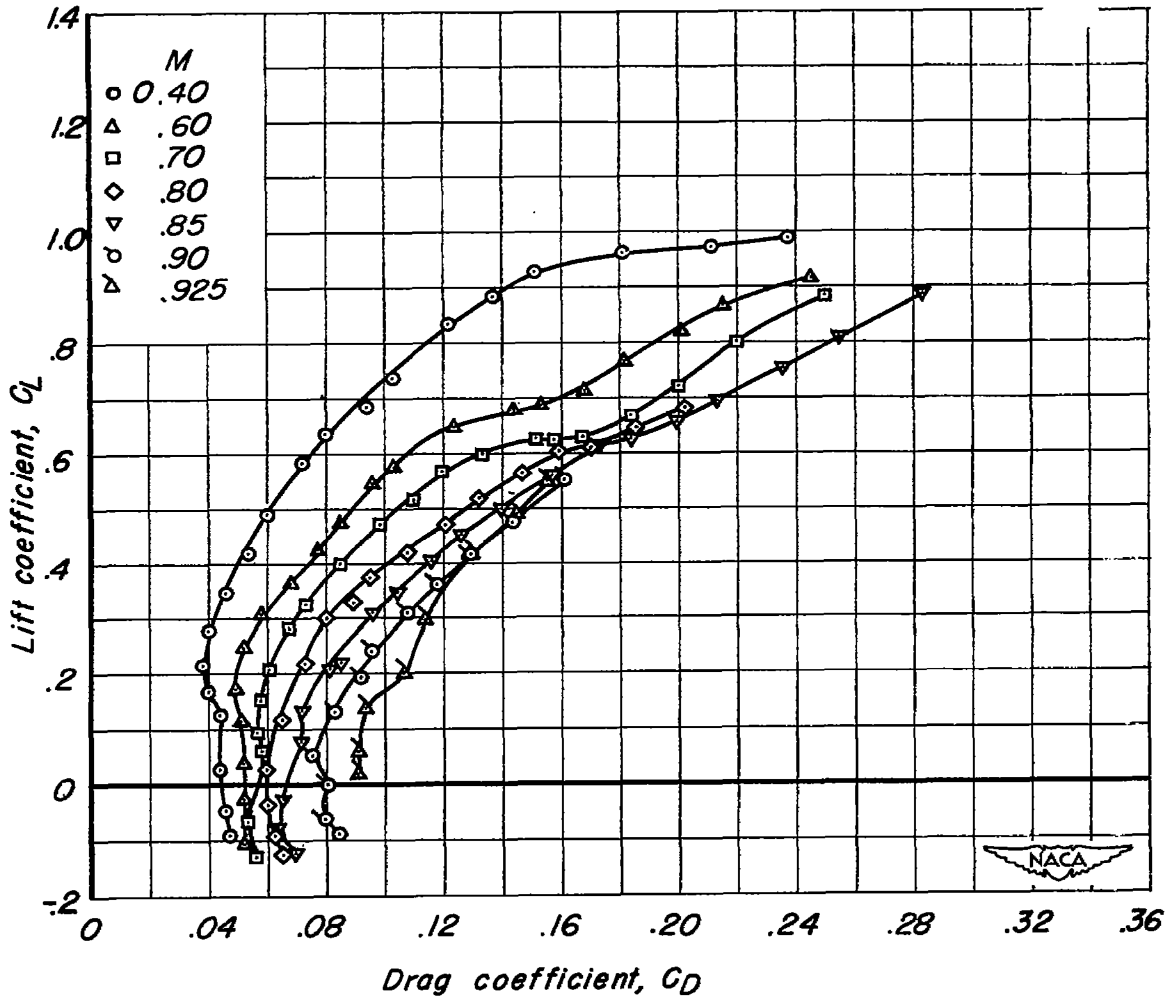

(c) Drag characteristics.

Figure 19.- Concluded.

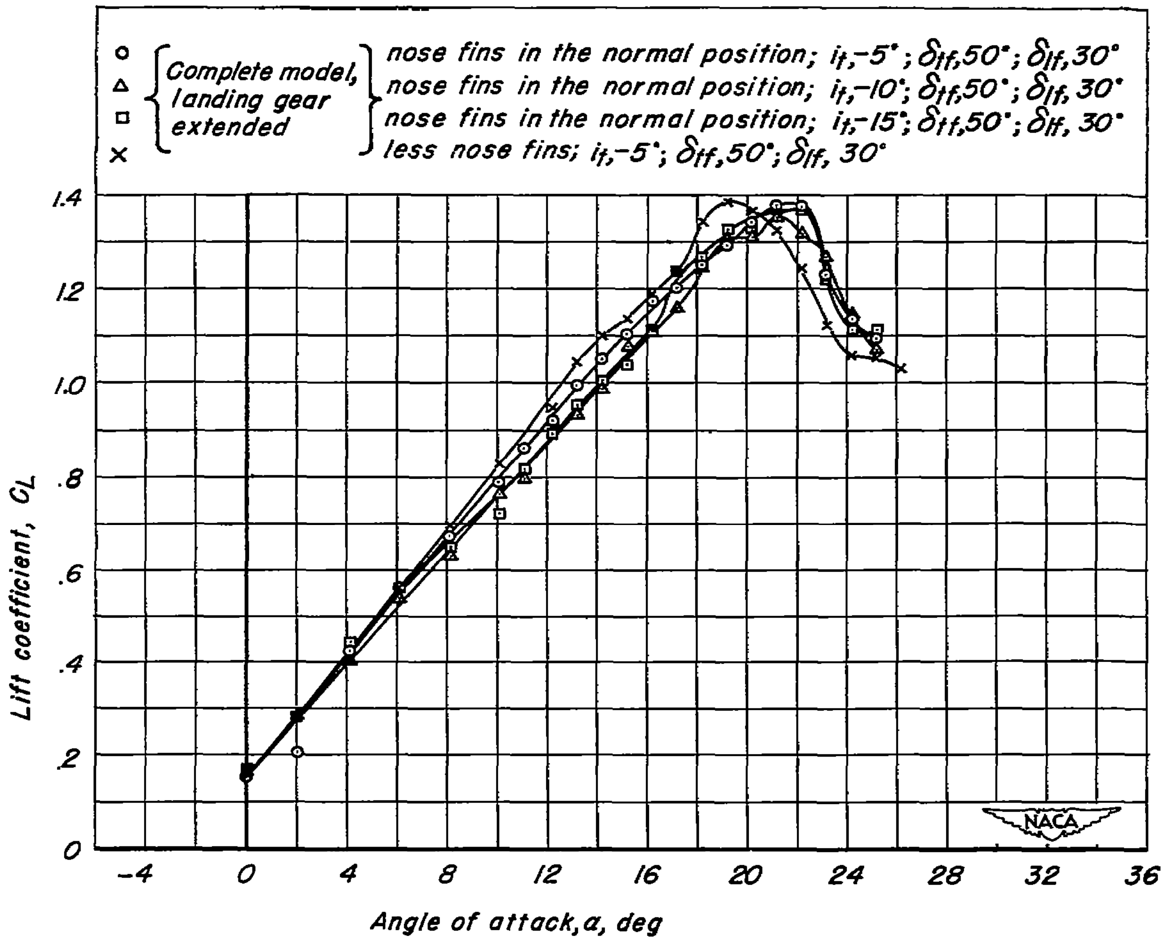

(a) Lift characteristics.

Figure 20.– The aerodynamic characteristics of the MX-656 model with the landing gear extended. δ_{lf}, 30°; δ_{tf}, 50°; M, 0.25.

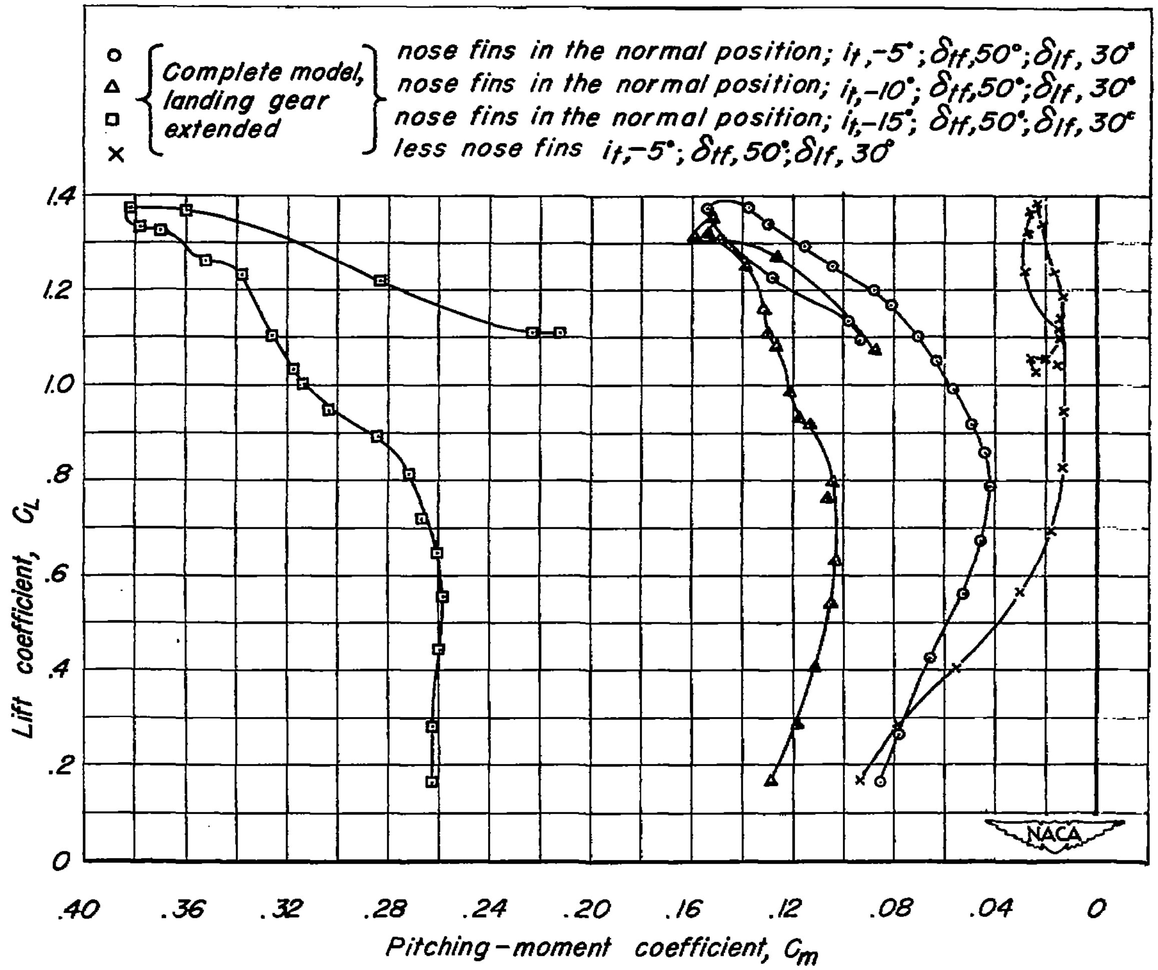

(b) Pitching-moment characteristics.

Figure 20.—Continued.

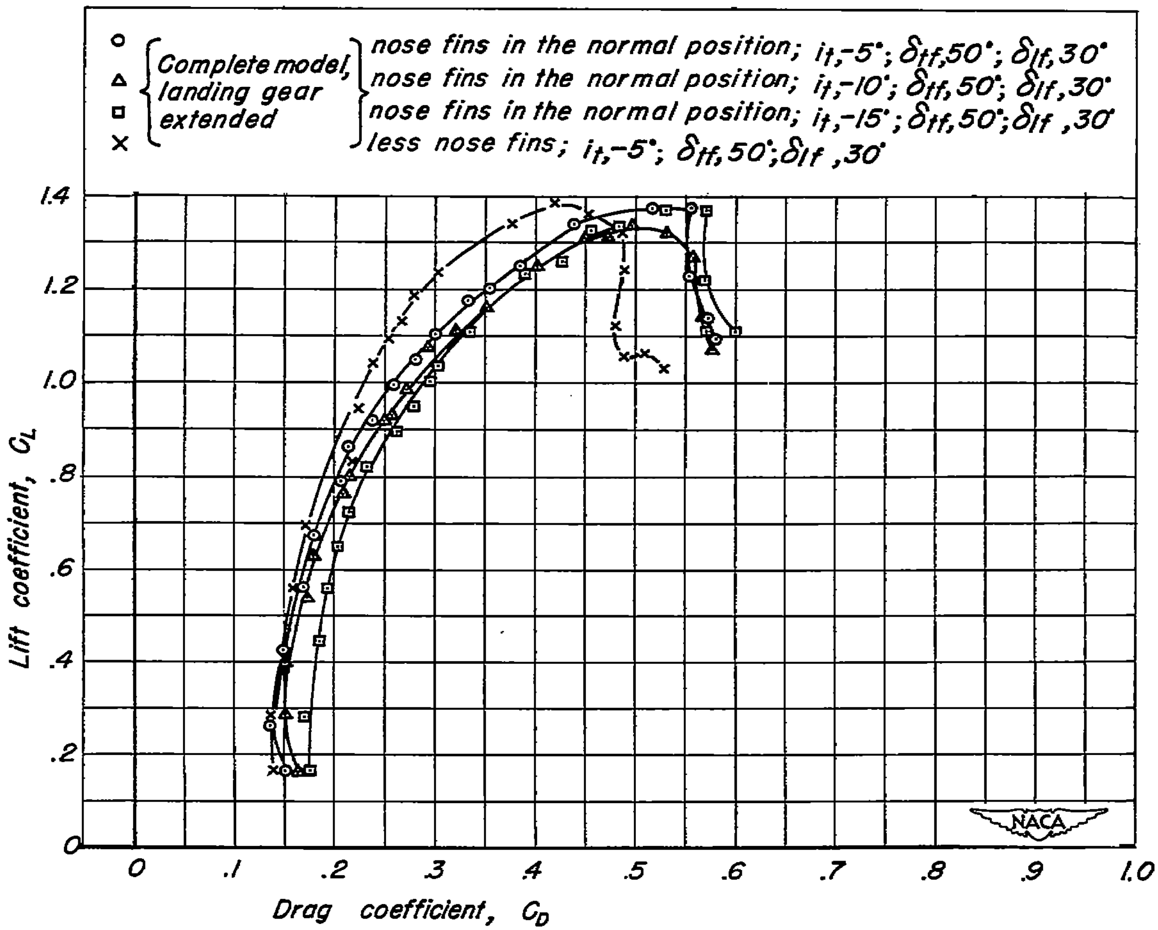

(c) Drag characteristics.

Figure 20.– Concluded.

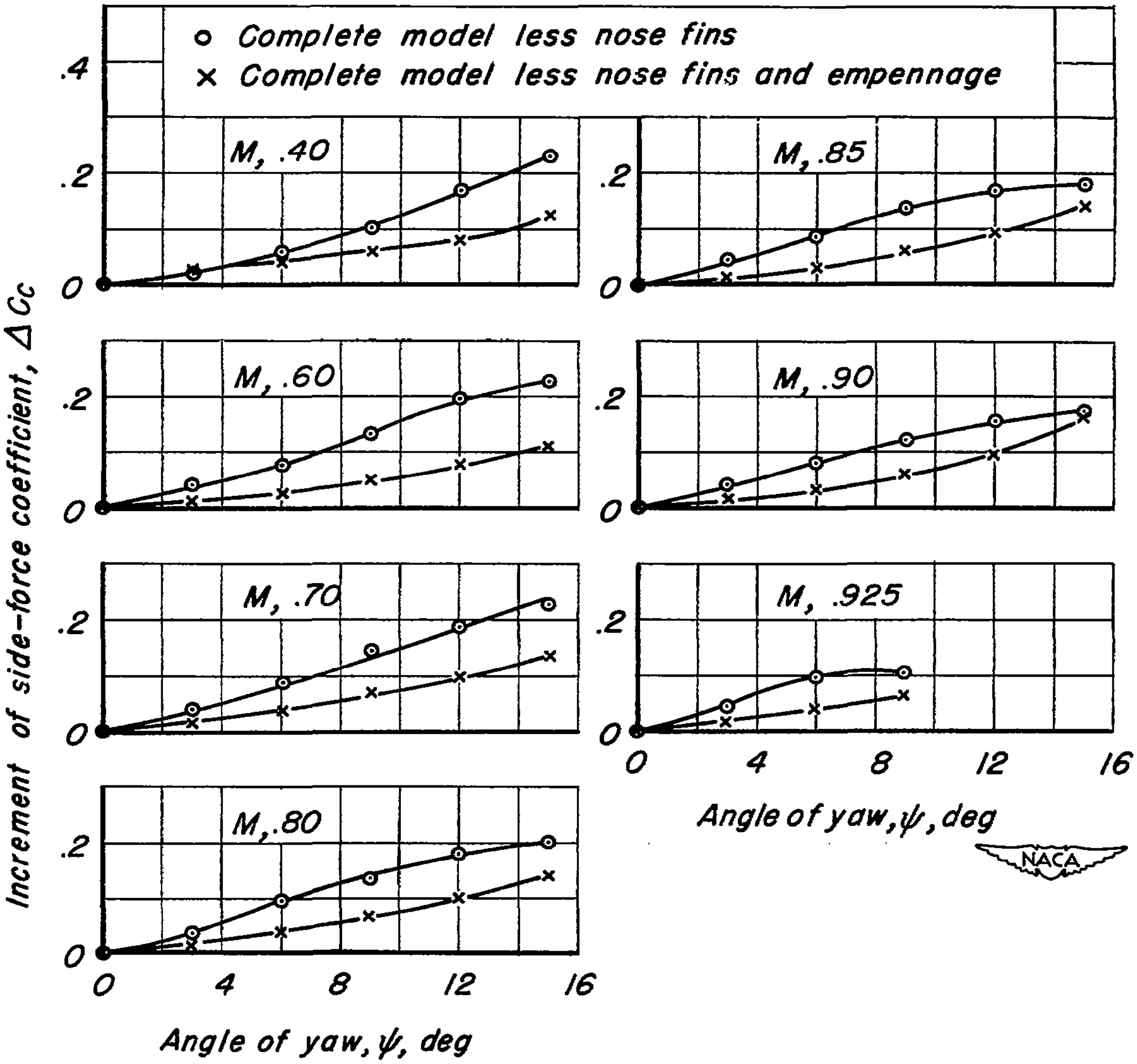

(a) Side-force characteristics.

Figure 21.- The aerodynamic characteristics in yaw of the MX-656 model without the nose fins. α, 0°.

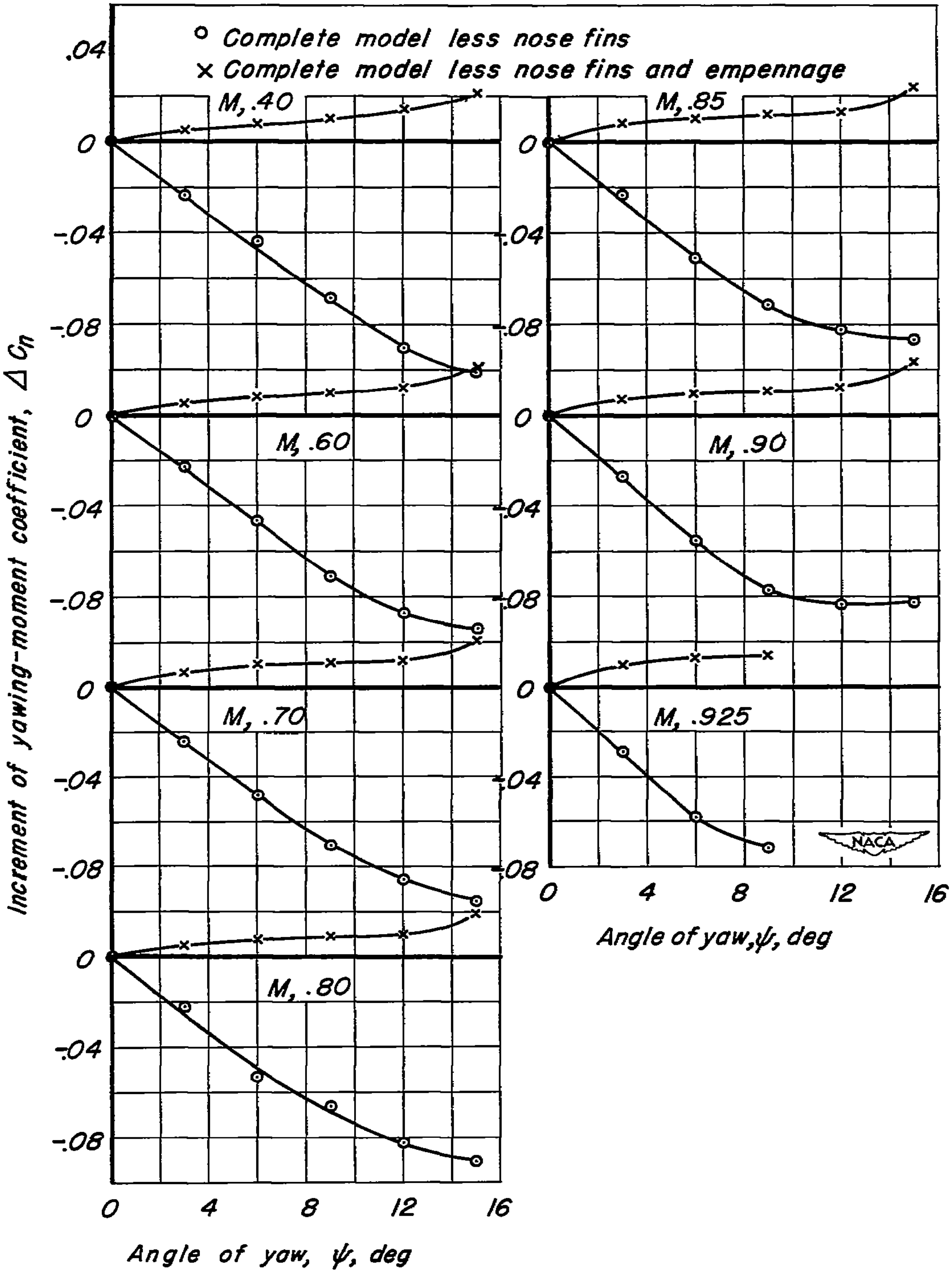

(b) Yawing-moment characteristics.

Figure 21.–Continued.

[redacted]

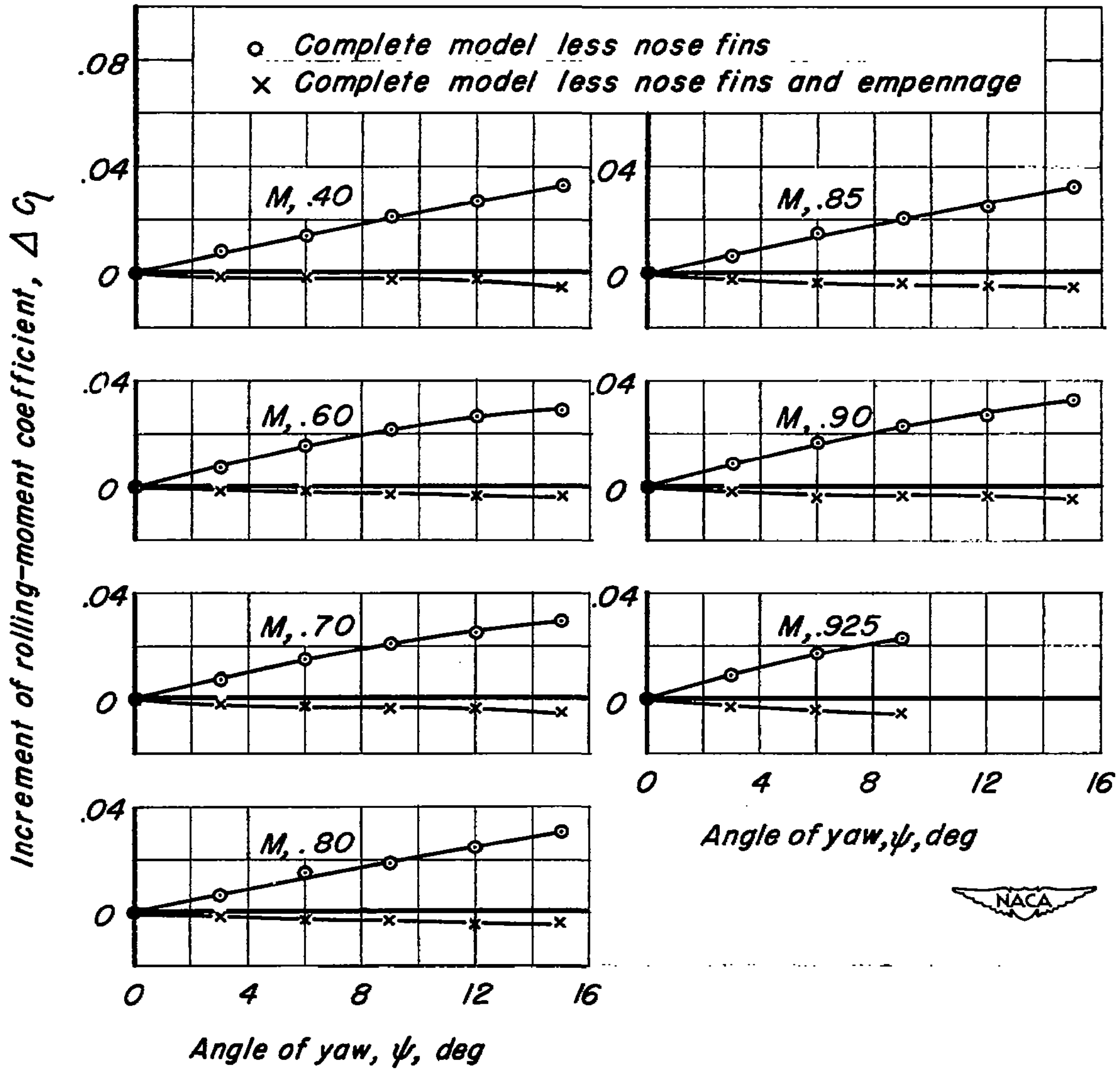

(c) Rolling-moment characteristics.

Figure 21.– Concluded.

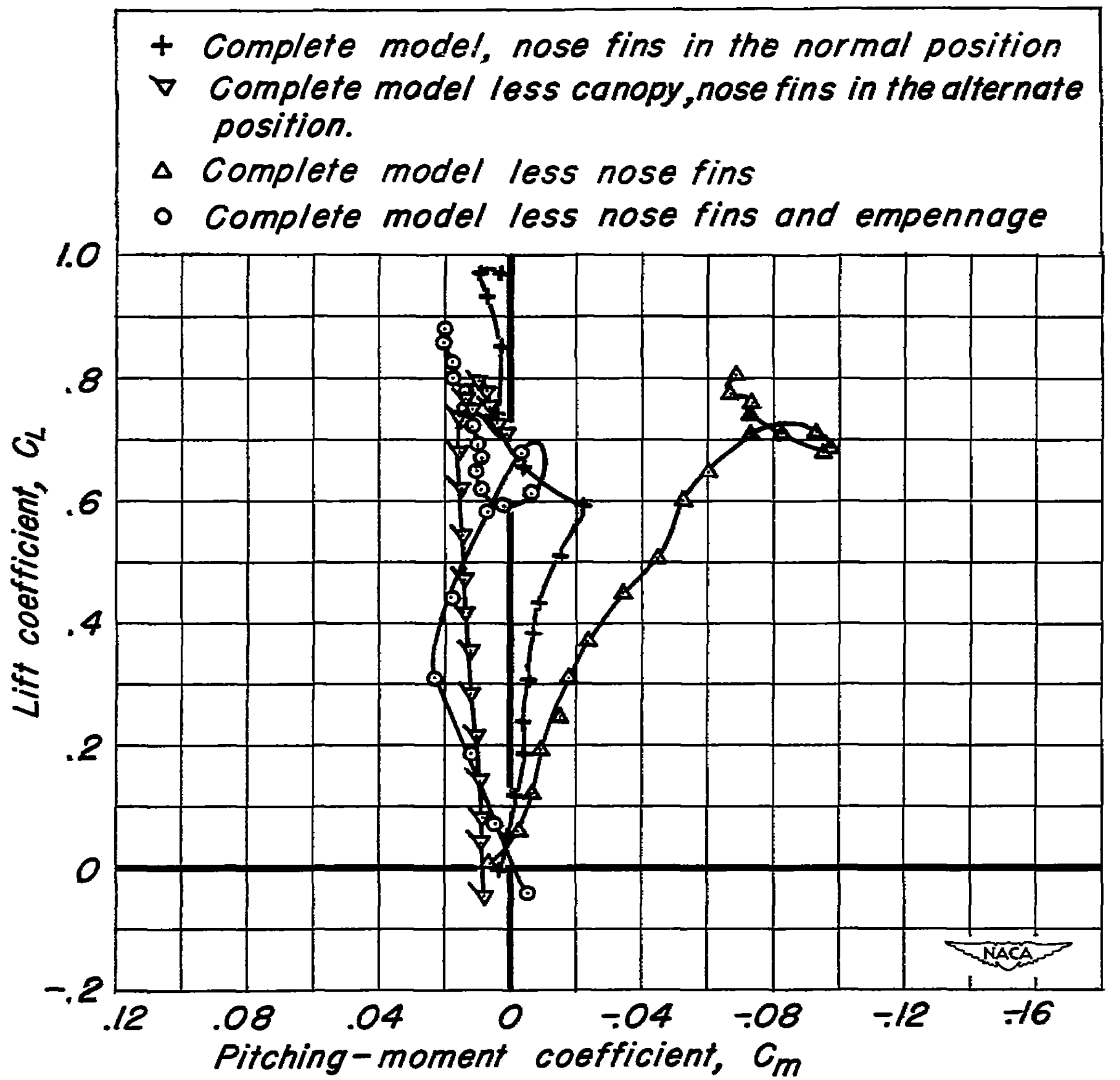

(a) Mach number, 0.40.

Figure 22.- The effect of the nose fins on the variation of pitching-moment coefficient with lift coefficient for the MX-656 model.

[redacted]

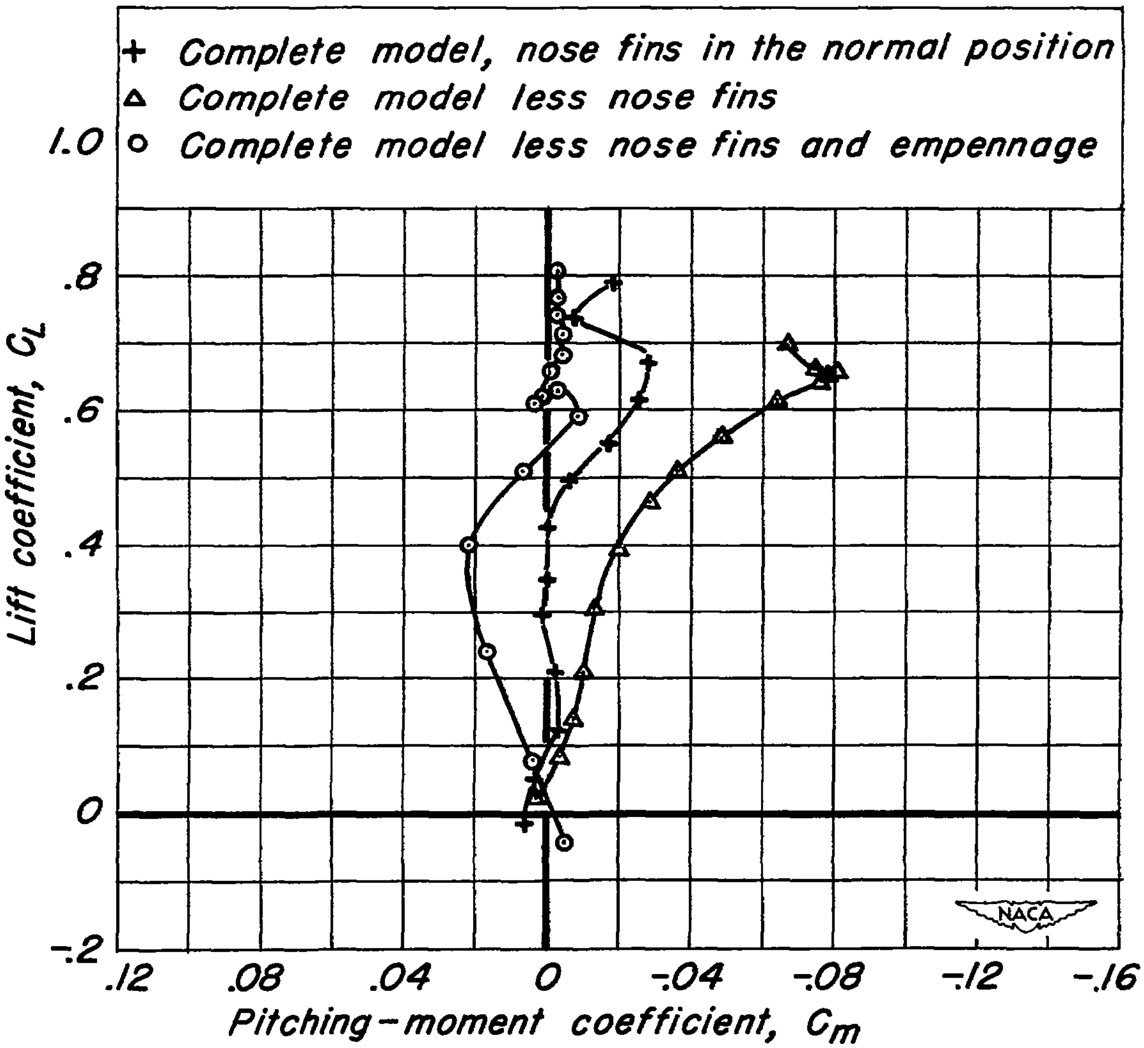

(b) Mach number, 0.80.

Figure 22.—Continued.

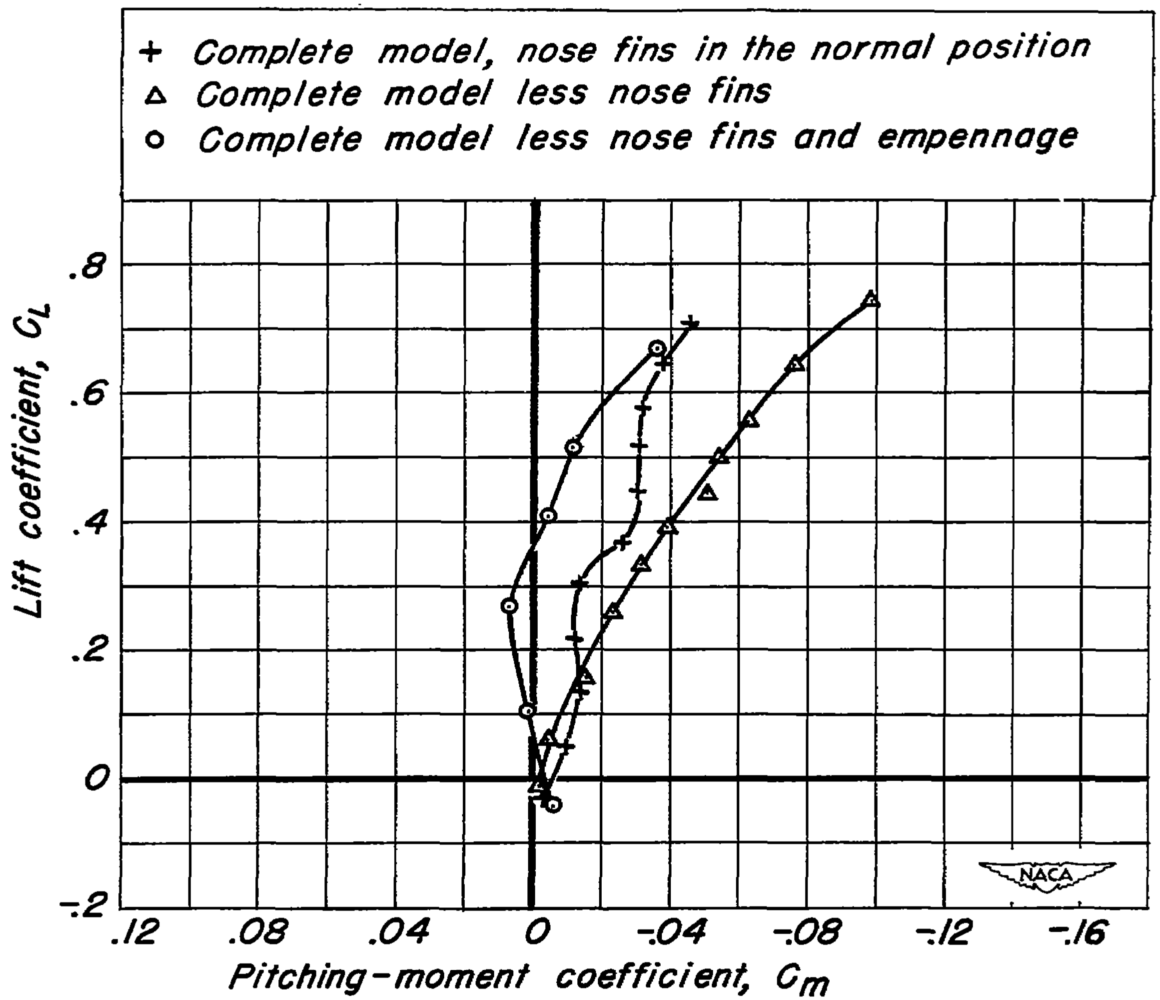

(c) Mach number, 0.90.

Figure 22.- Concluded.

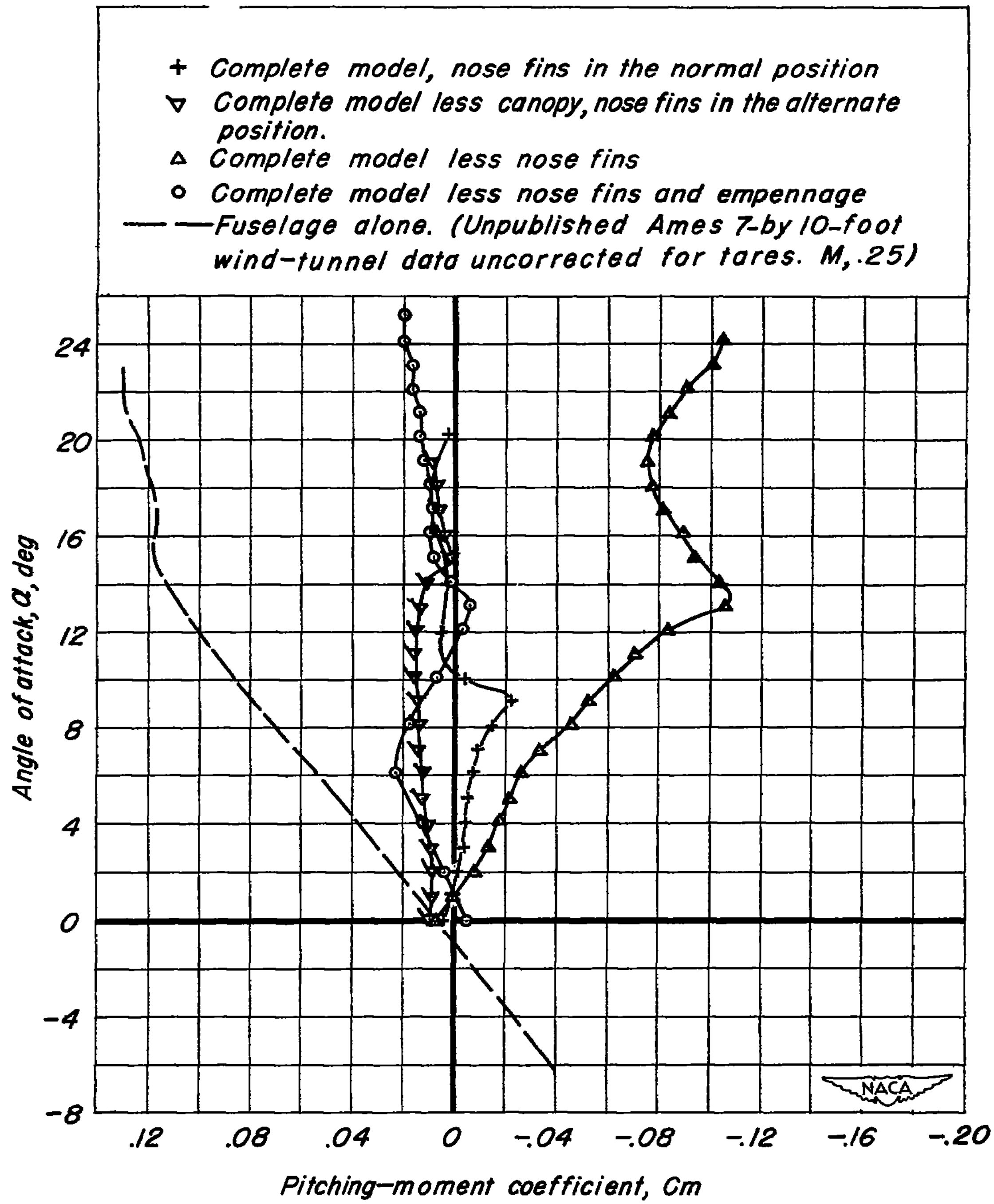

(a) Mach number, 0.40.

Figure 23.- The effect of the nose fins on the variation of pitching-moment coefficient with angle of attack for the MX-656 model.

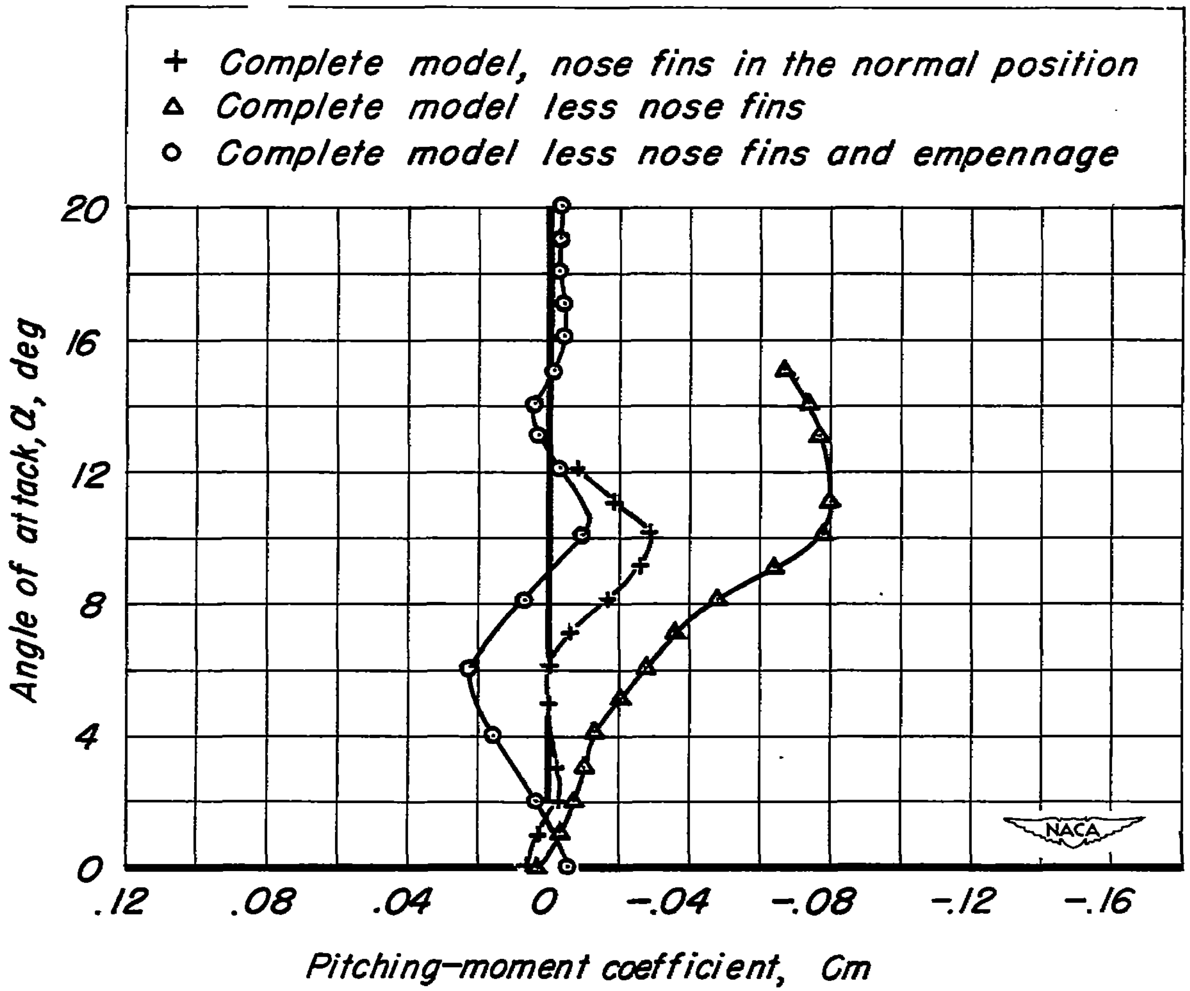

(b) Mach number, 0.80.

Figure 23.–Continued.

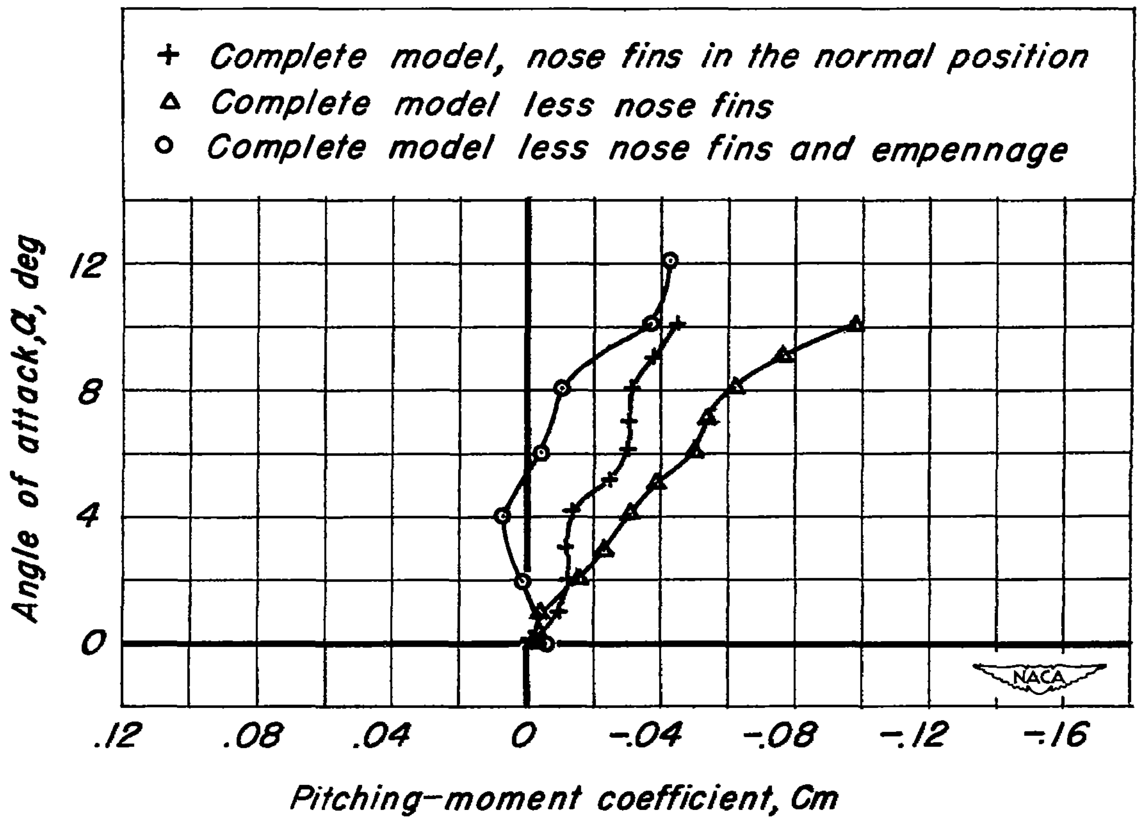

(c) Mach number, 0.90.

Figure 23.- Concluded.

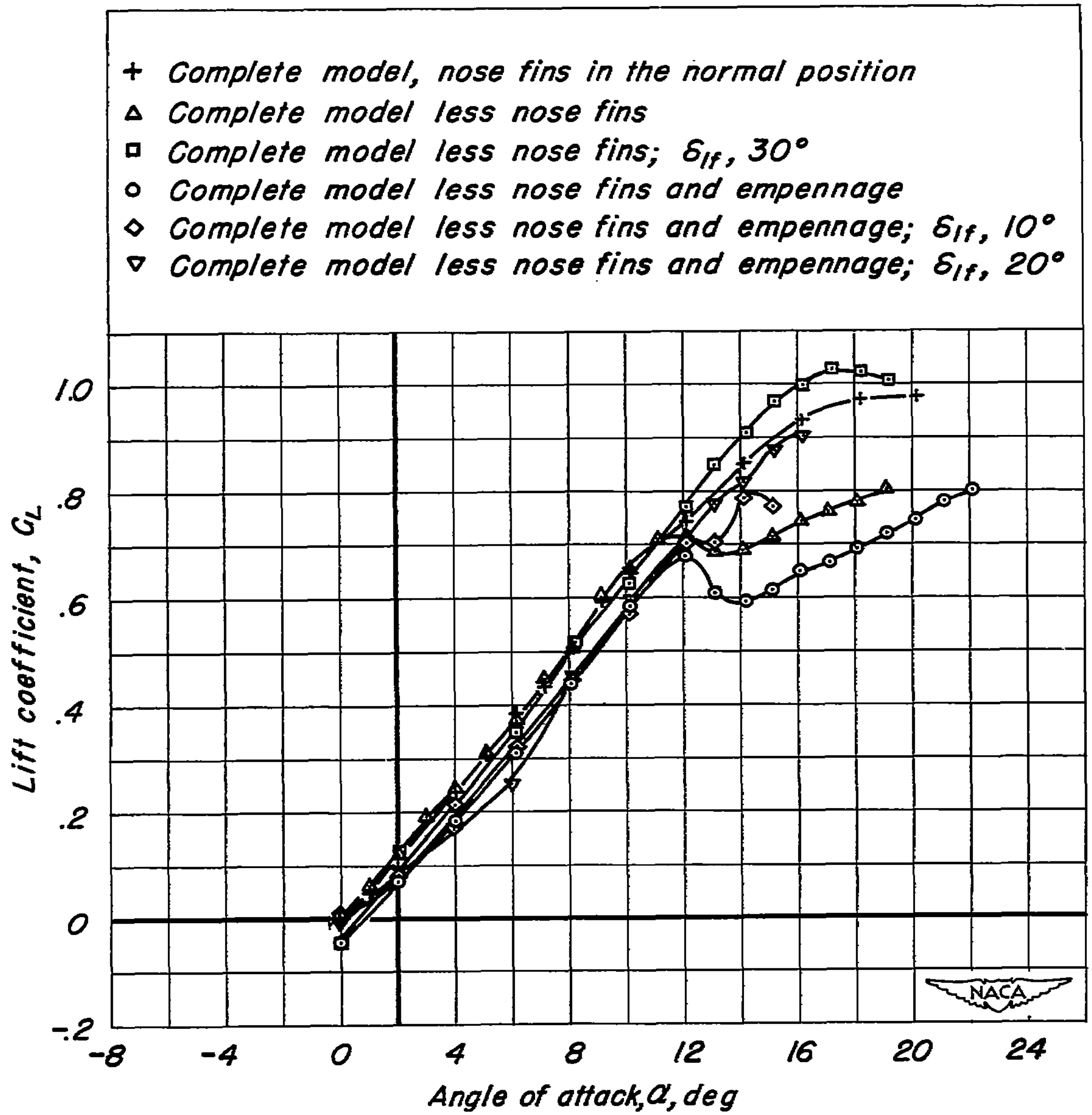

(a) Mach number, 0.40.

Figure 24.– The effect of several changes in configuration on the variation of lift coefficient with angle of attack for the MX-656 model.

[redacted]

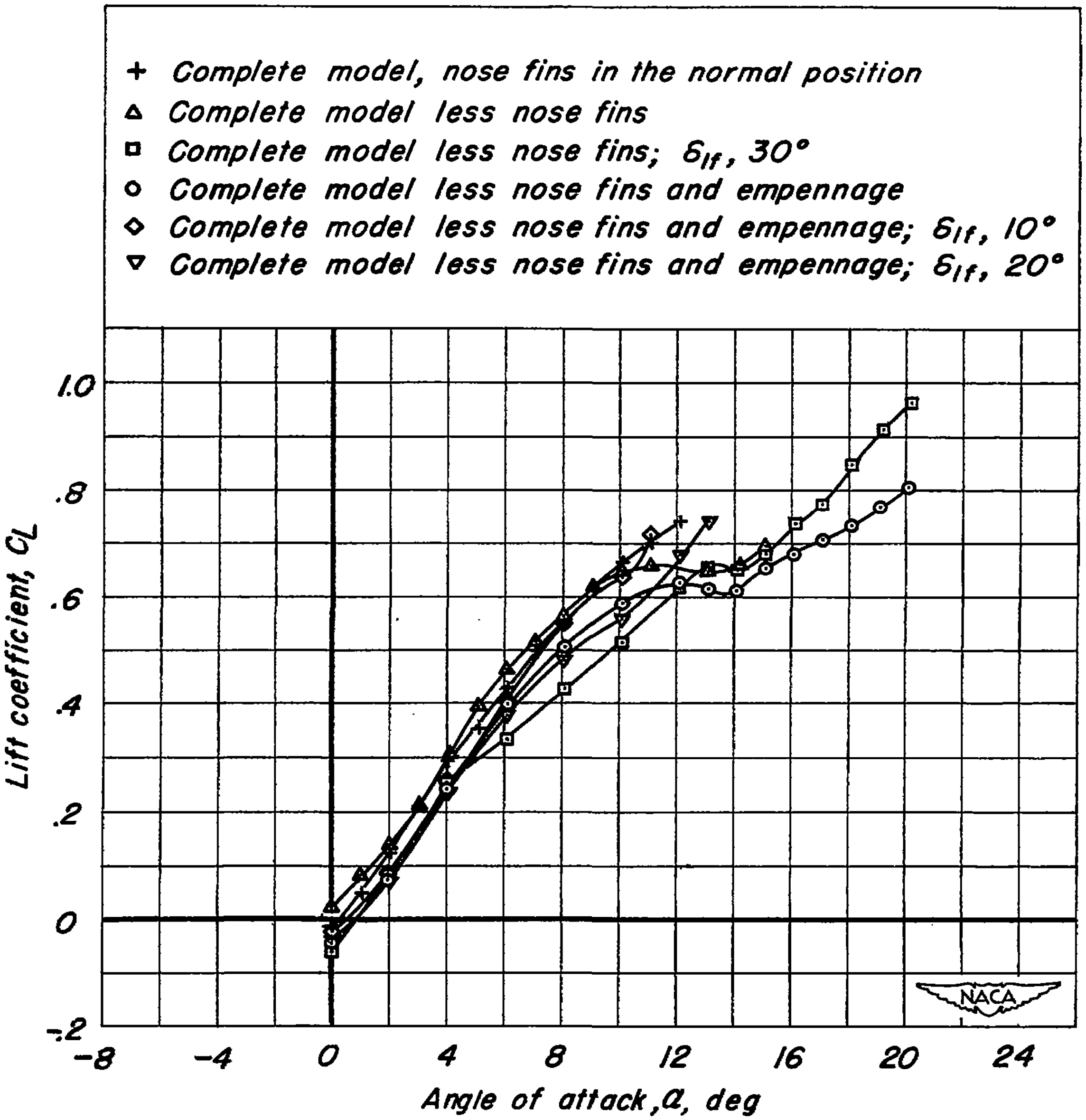

(b) Mach number, 0.80.

Figure 24.– Continued.

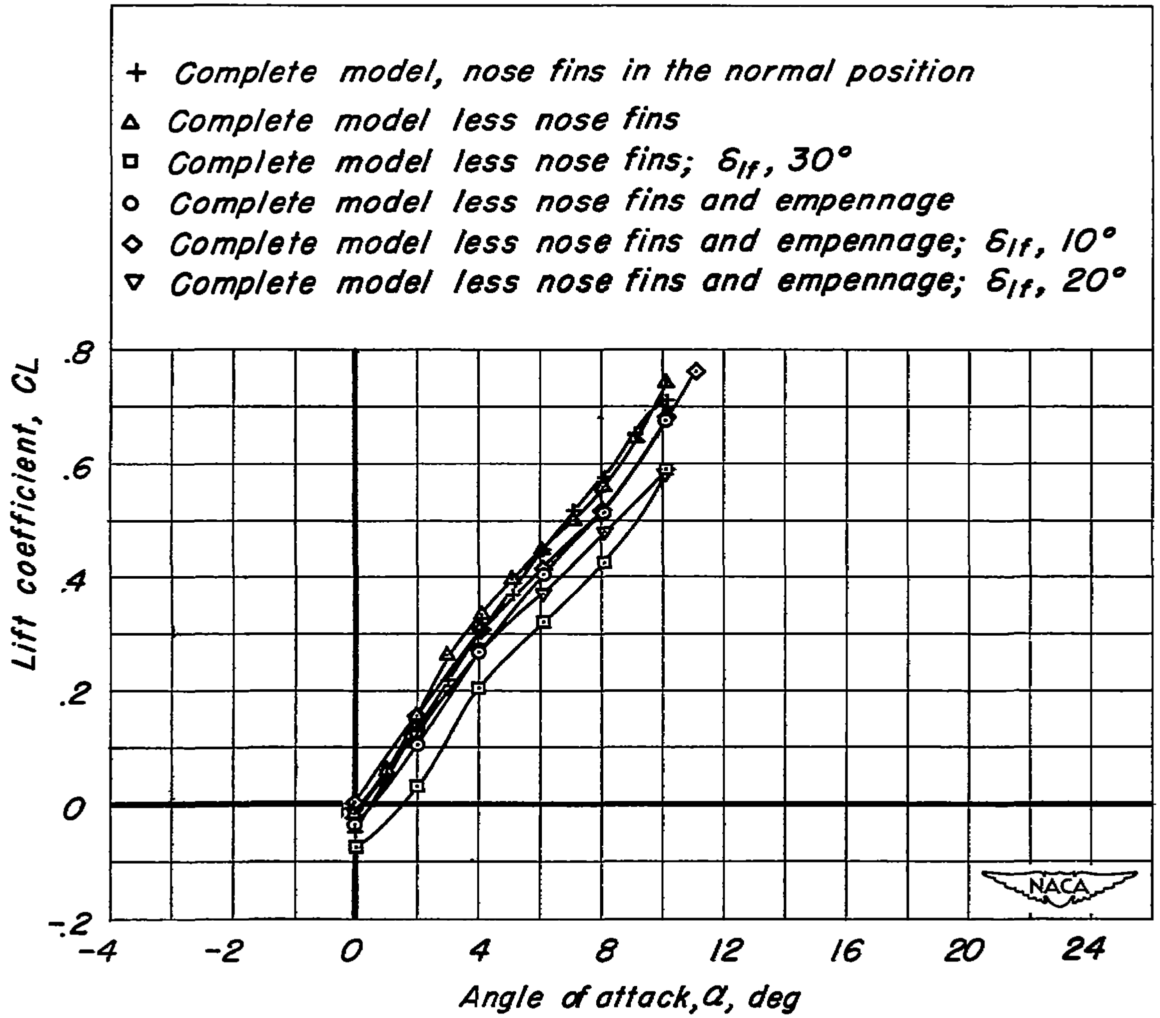

(c) Mach number, 0.90.

Figure 24.- Concluded.

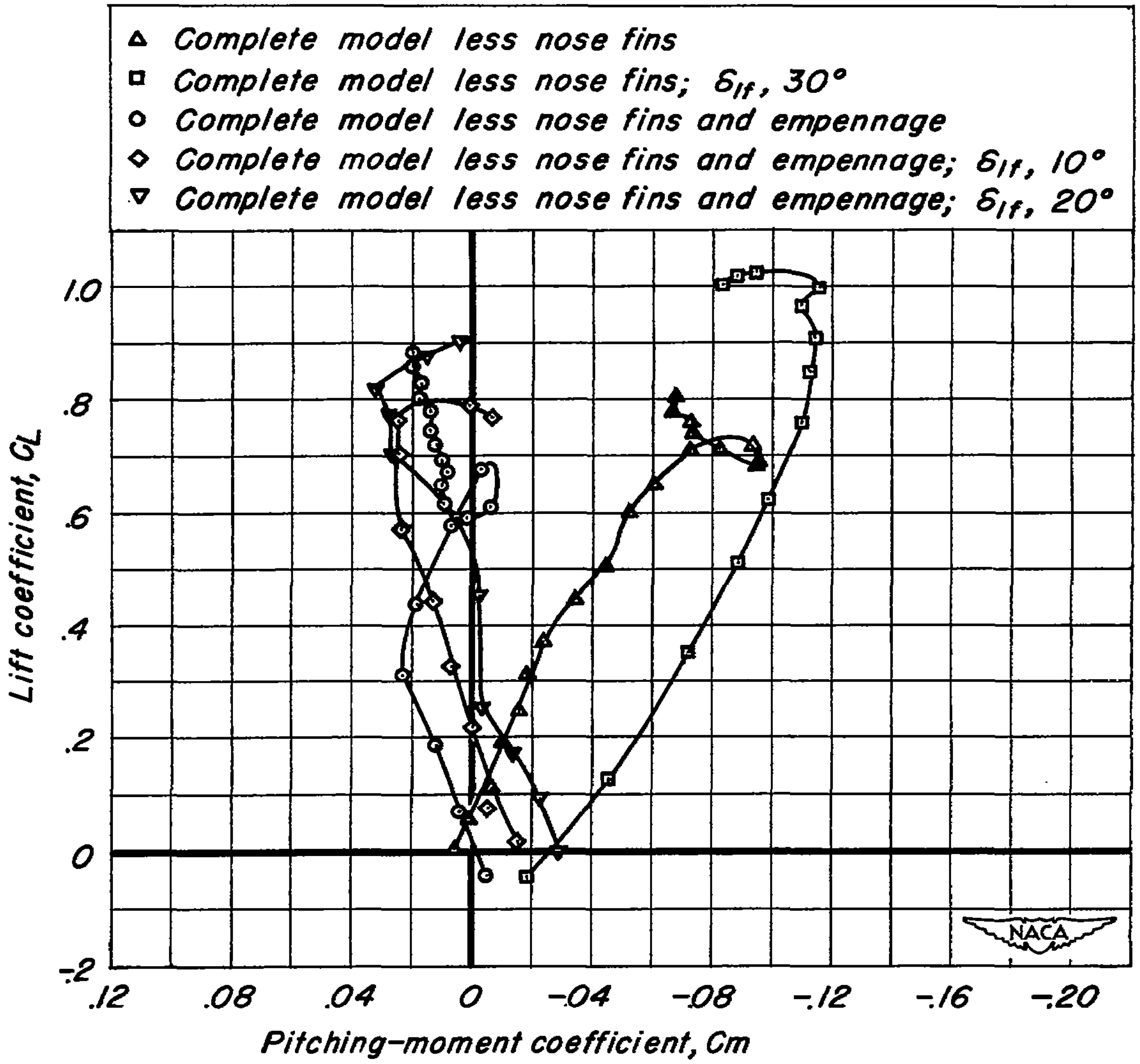

(a) Mach number, 0.40.

Figure 25.– The effect of the leading-edge flaps on the variation of pitching-moment coefficient with lift coefficient for the MX-656 model without the nose fins.

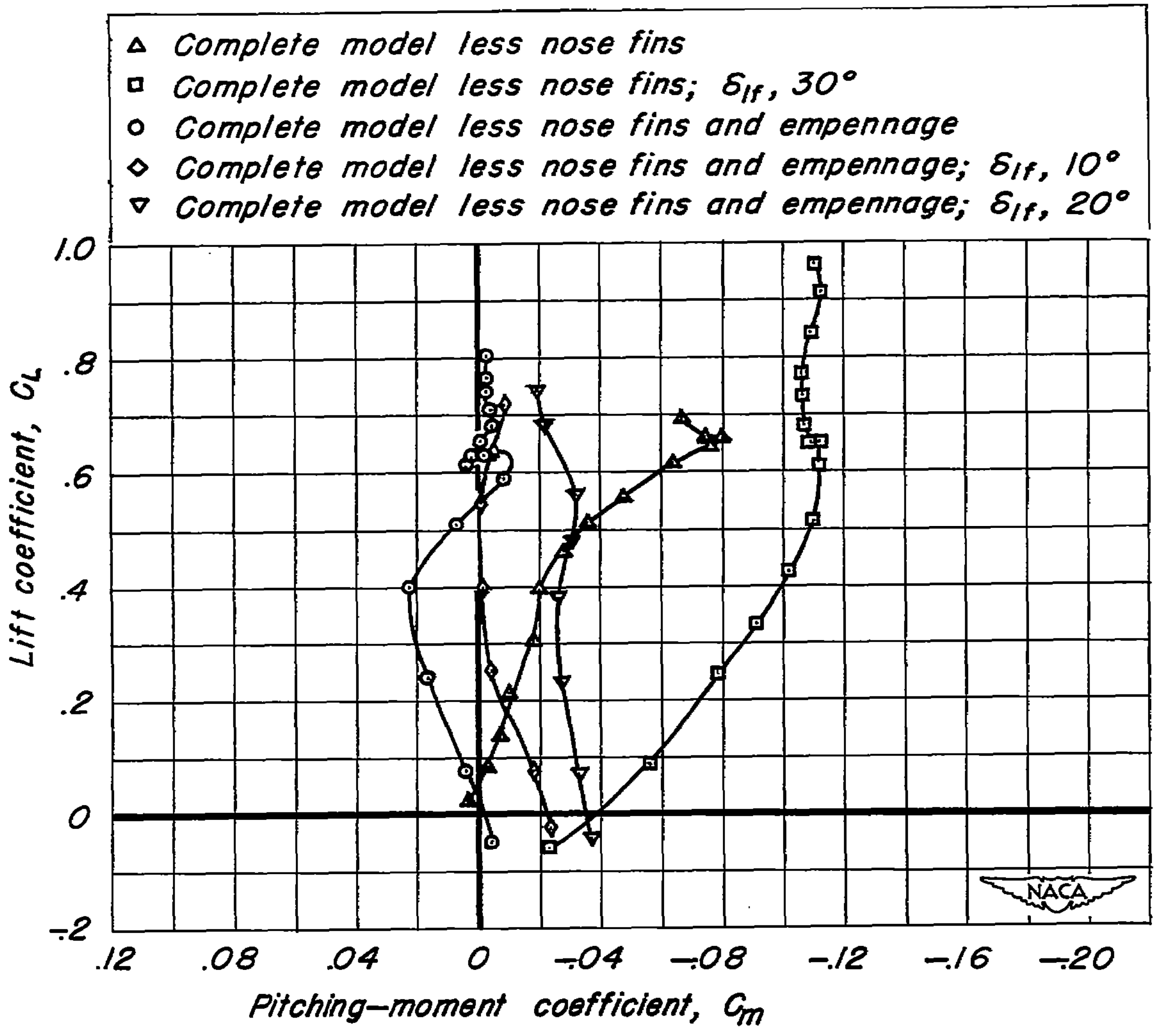

(b) Mach number, 0.80.

Figure 25.— Continued.

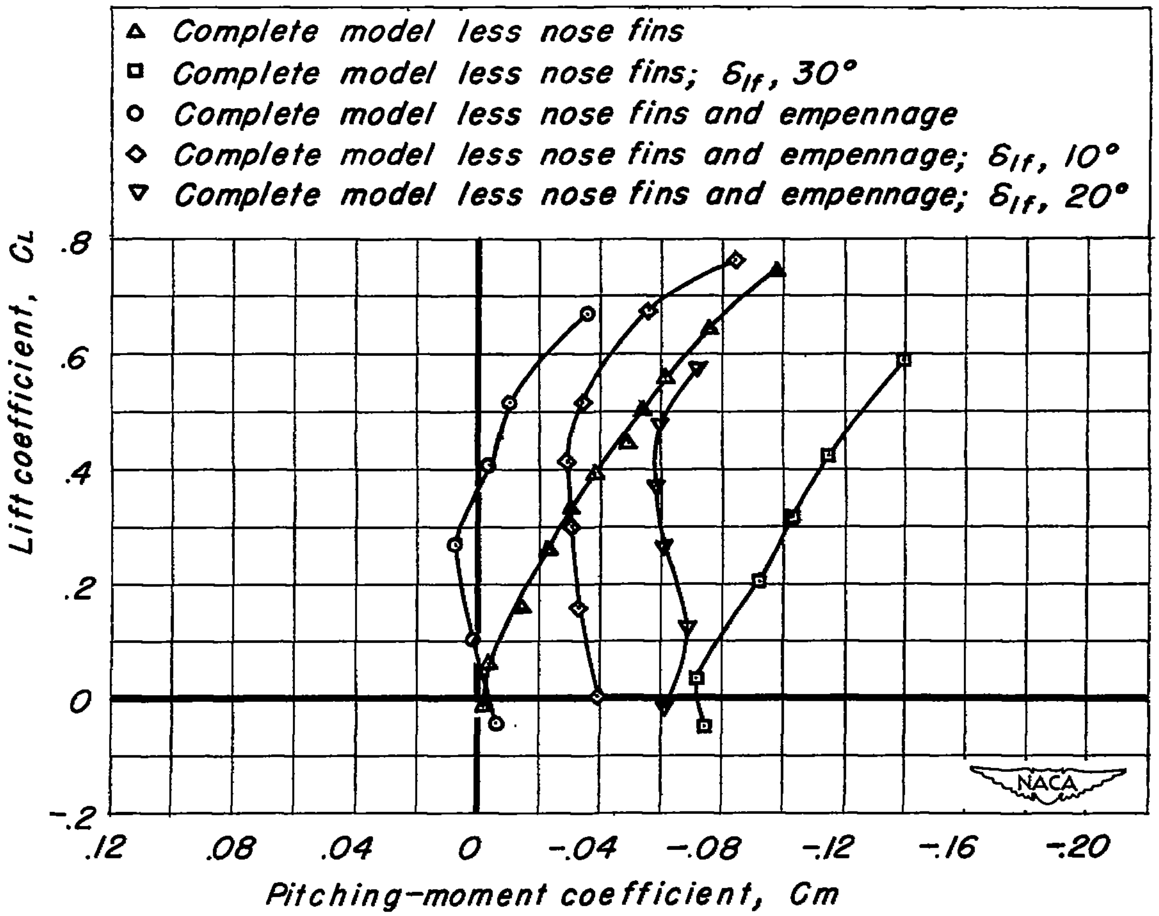

(c) Mach number, 0.90.

Figure 25.– Concluded.

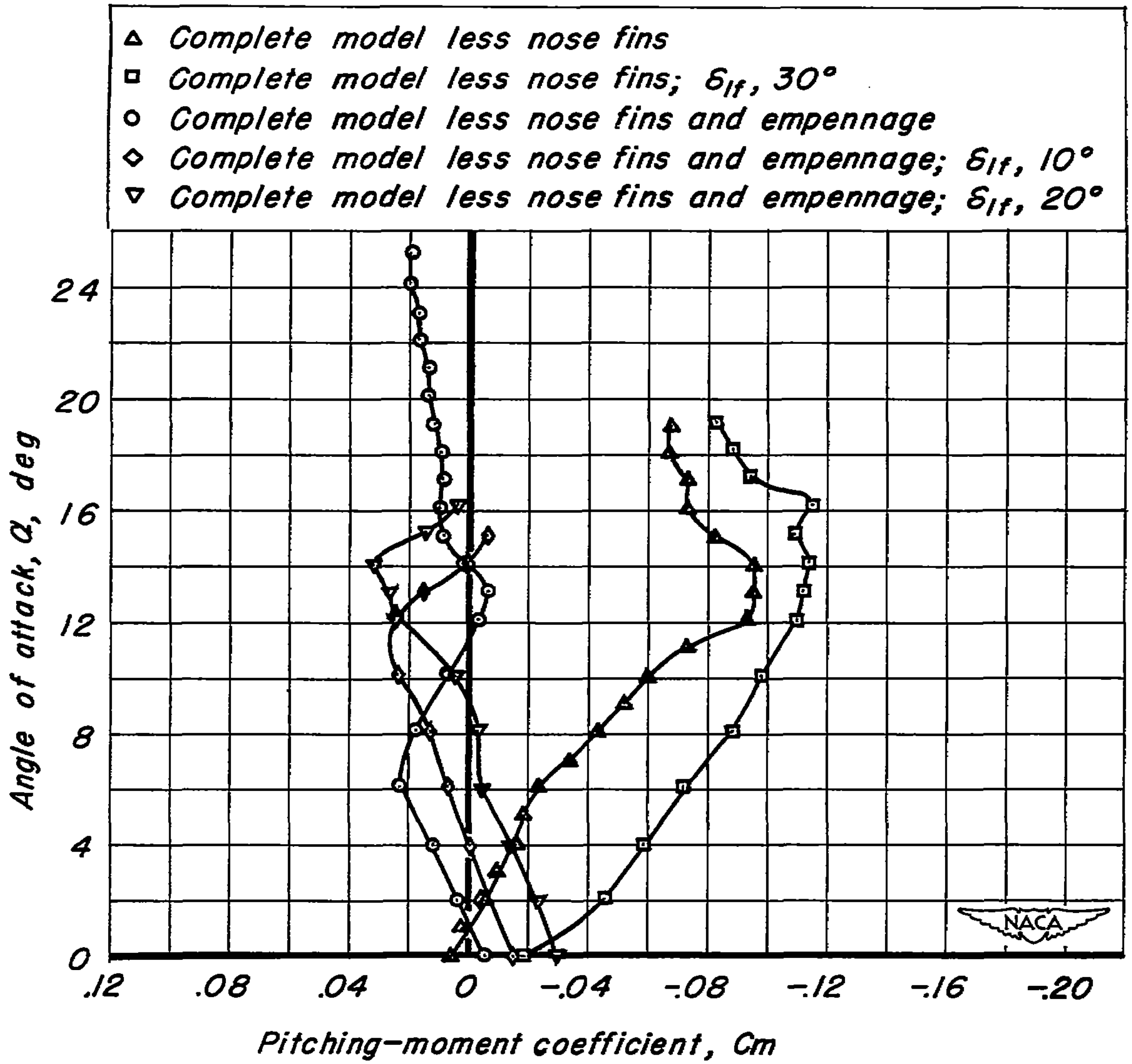

(a) Mach number, 0.40.

Figure 26.– The effect of the leading-edge flaps on the variation of pitching-moment coefficient with angle of attack for the MX-656 model.

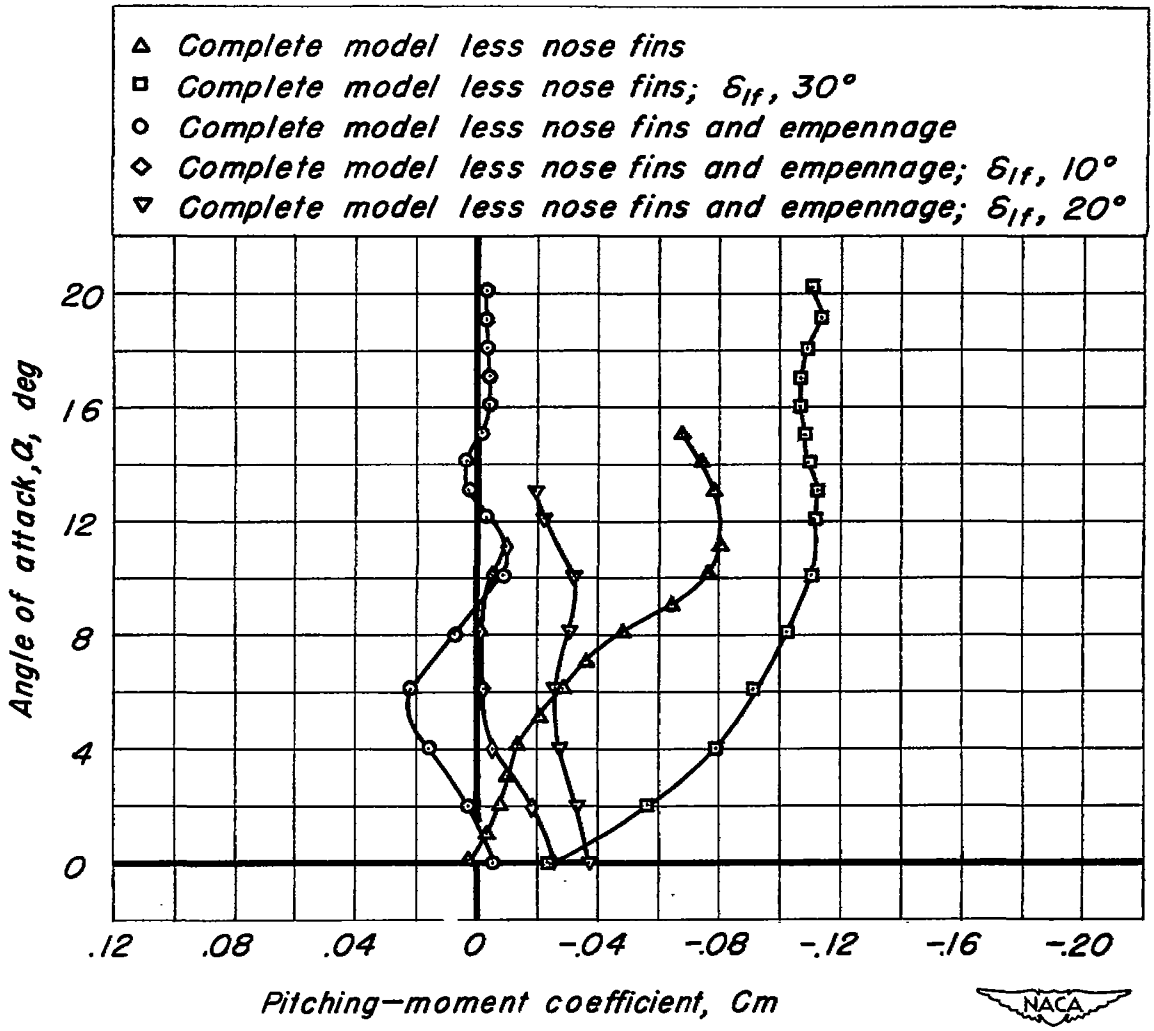

(b) Mach number, 0.80.

Figure 26.- Continued.

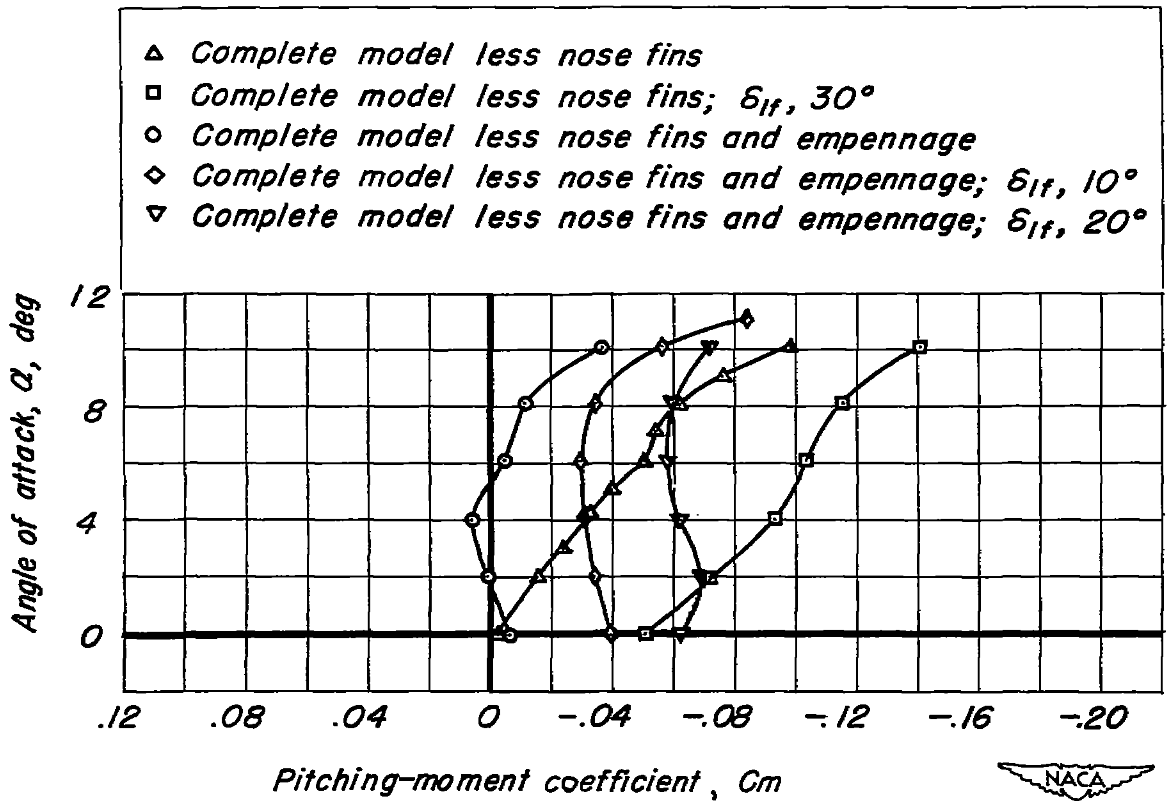

(c) Mach number, 0.90.

Figure 26.—Concluded.

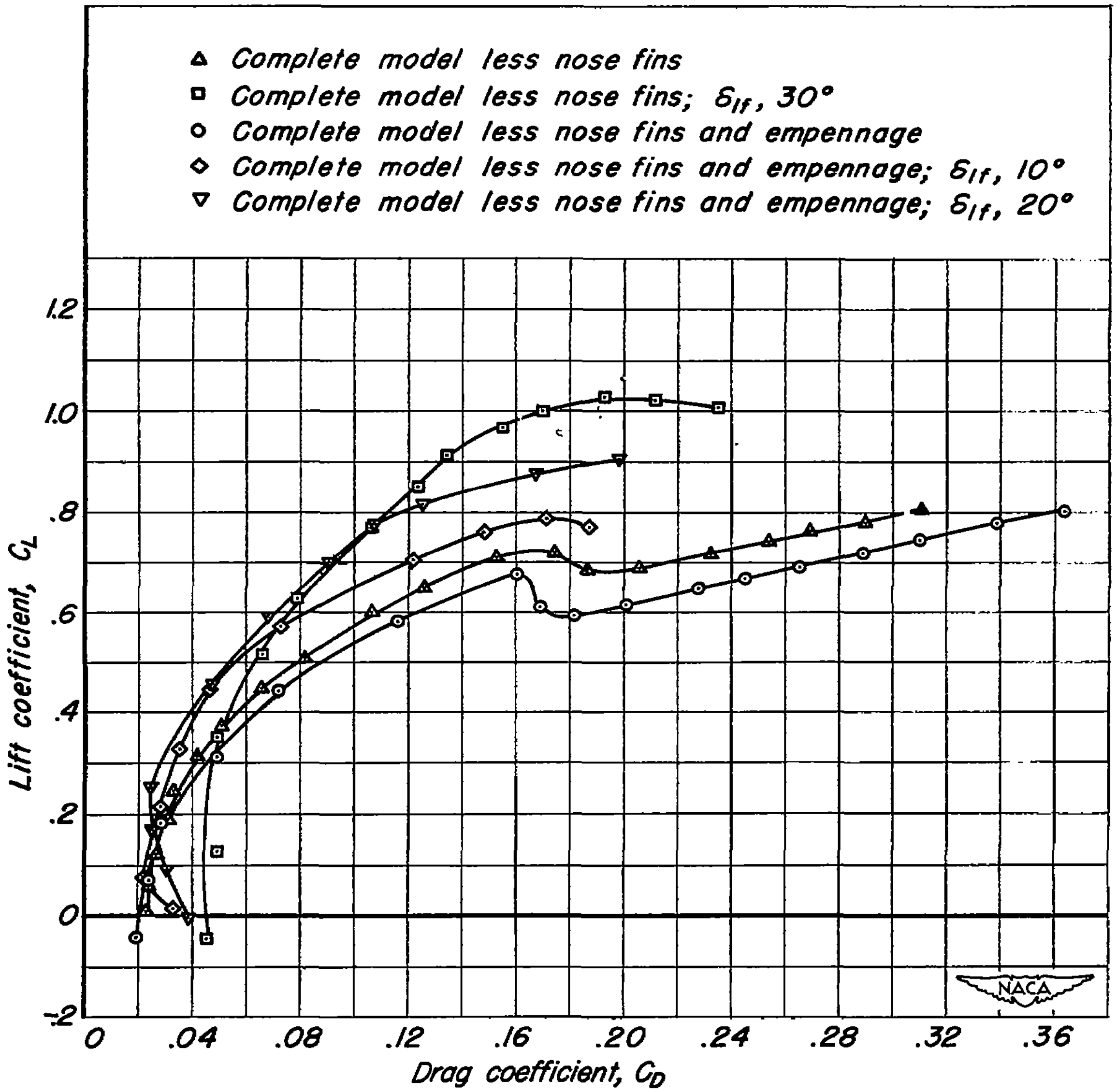

(a) Mach number, 0.40.

Figure 27.– The effect of the leading-edge flaps on the variation of drag coefficient with lift coefficient for the MX-656 model without the nose fins.

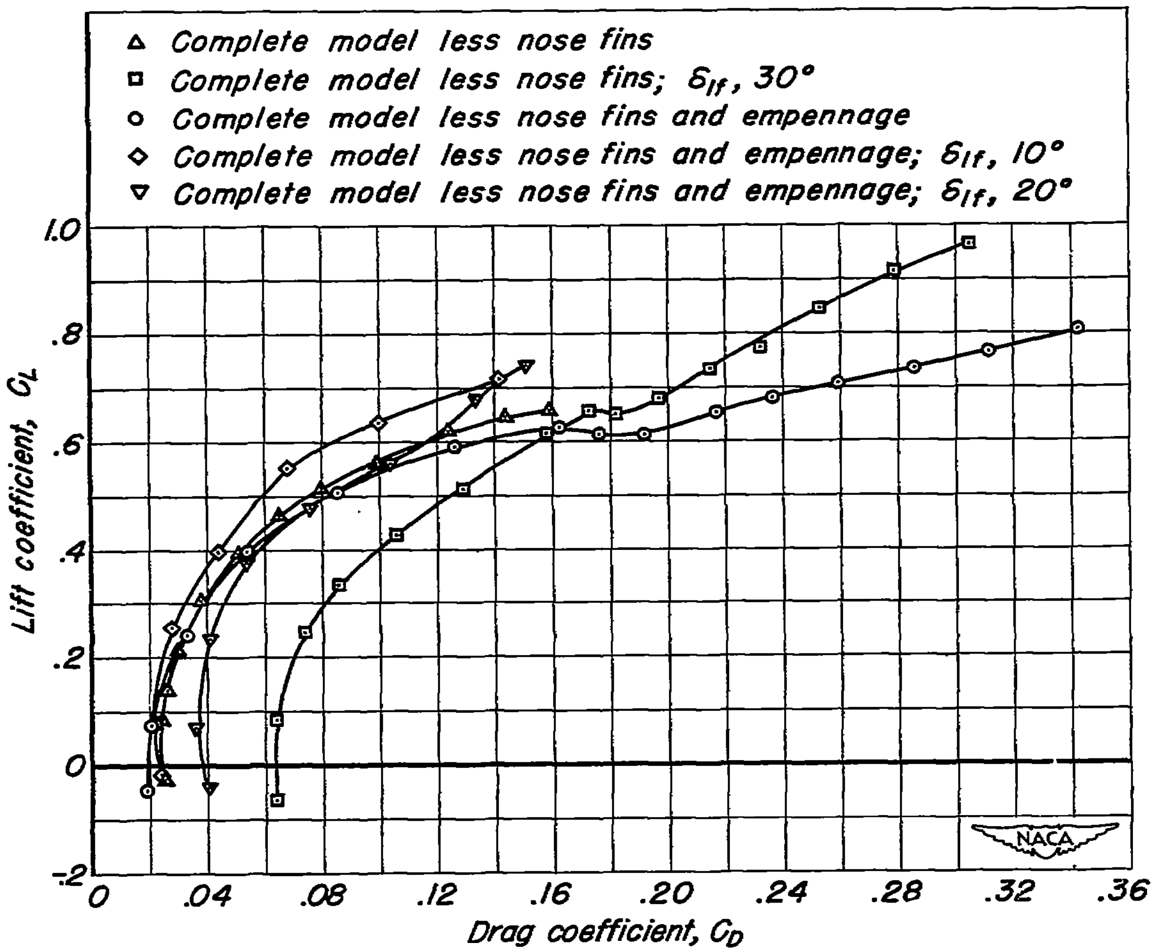

(b) Mach number, 0.80.

Figure 27.– Continued.

[redacted]

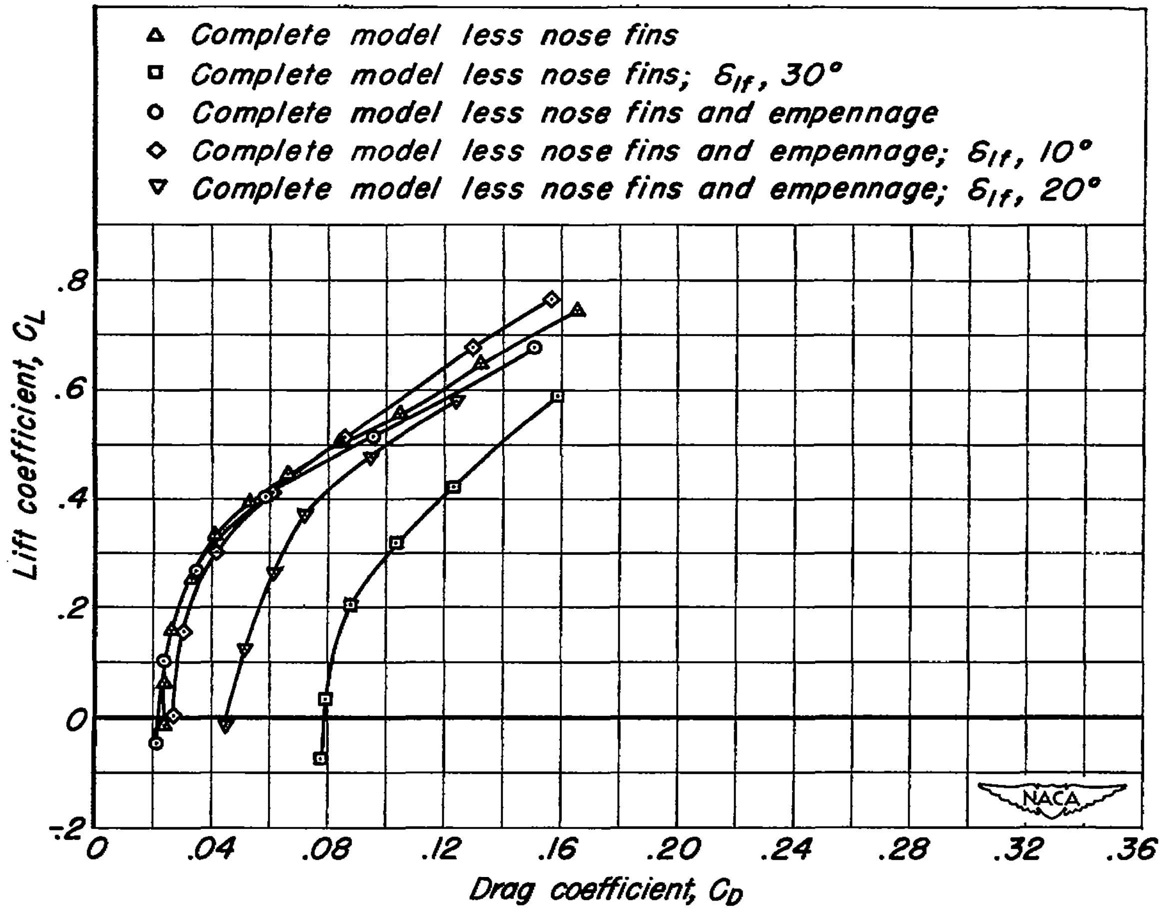

(c) Mach number, 0.90.

Figure 27.- Concluded.

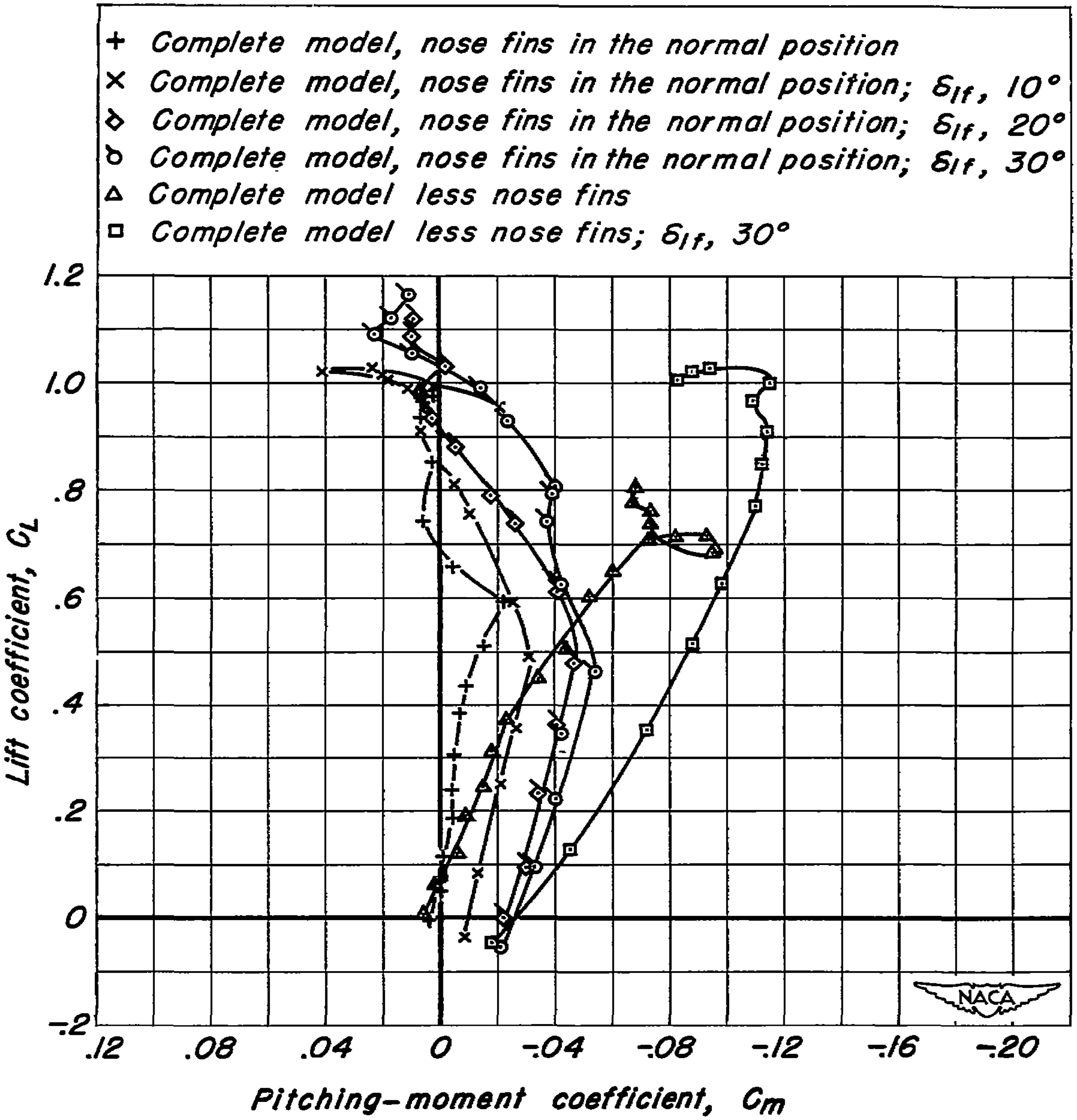

(a) Mach number, 0.40.

Figure 28.- The effect of several changes in configuration on the variation of pitching-moment coefficient with lift coefficient for the MX-656 model.

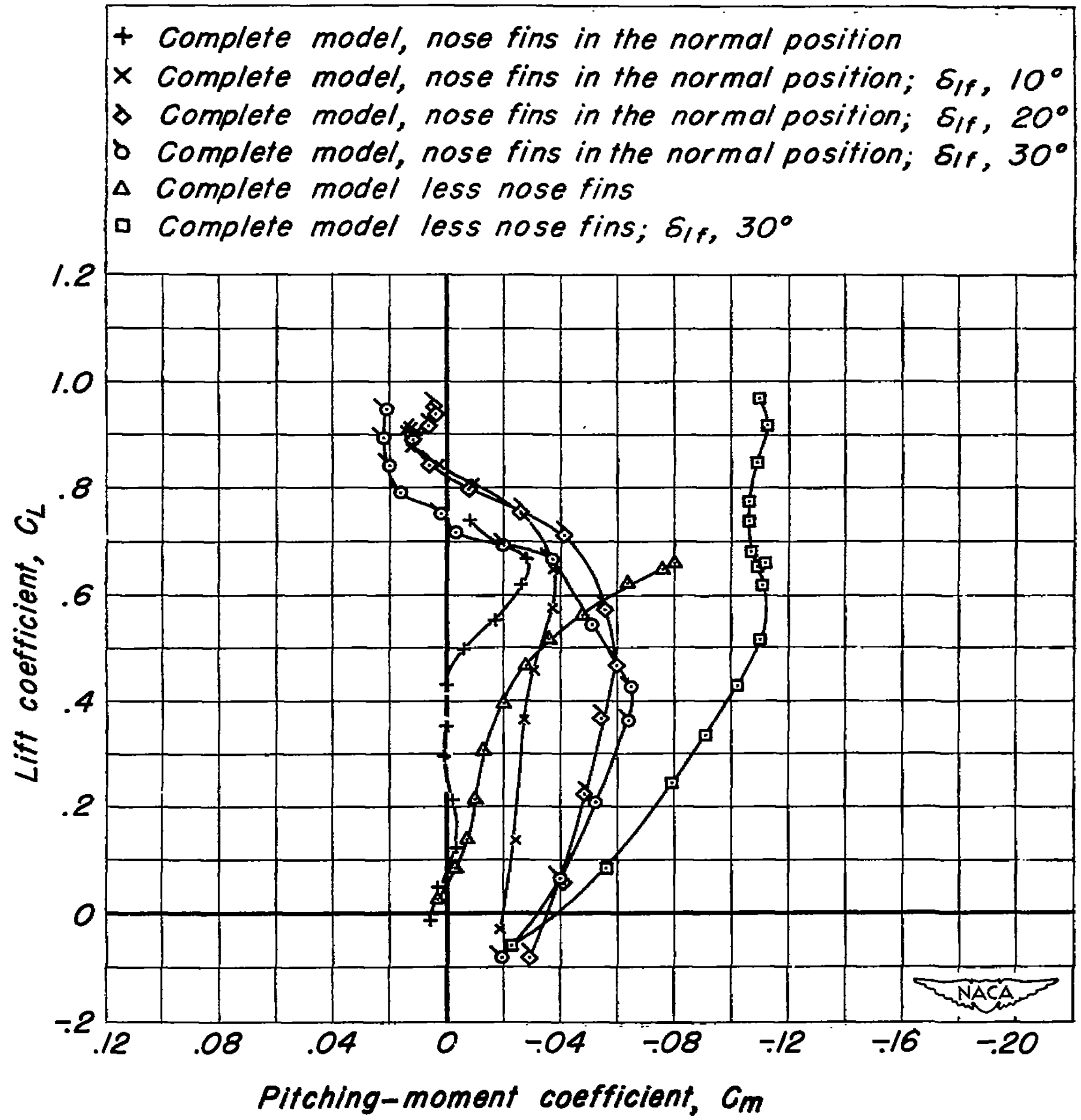

(b) Mach number, 0.80.

Figure 28.- Continued.

[redacted]

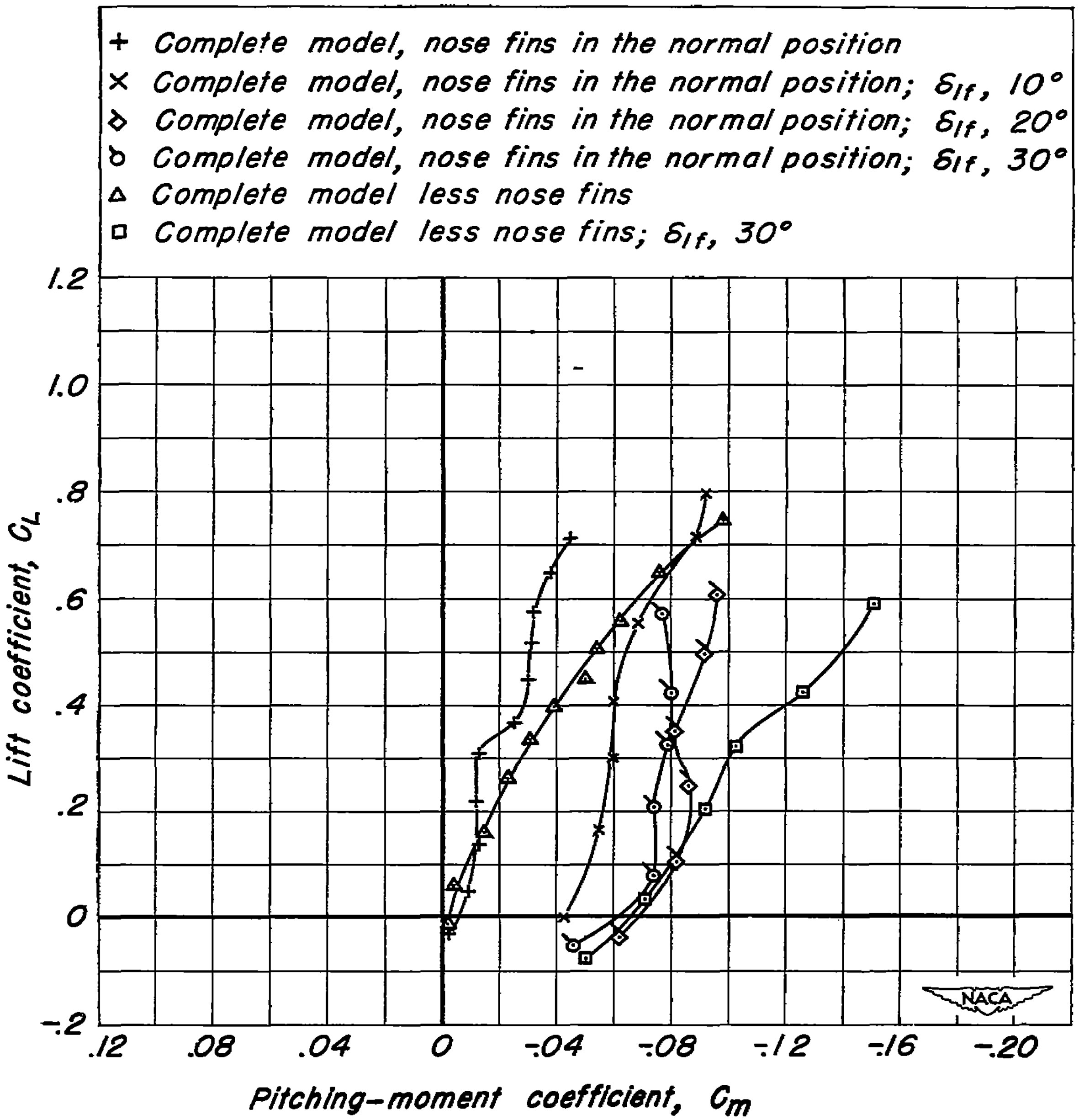

(c) Mach number, 0.90.

Figure 28.- Concluded.

[redacted]

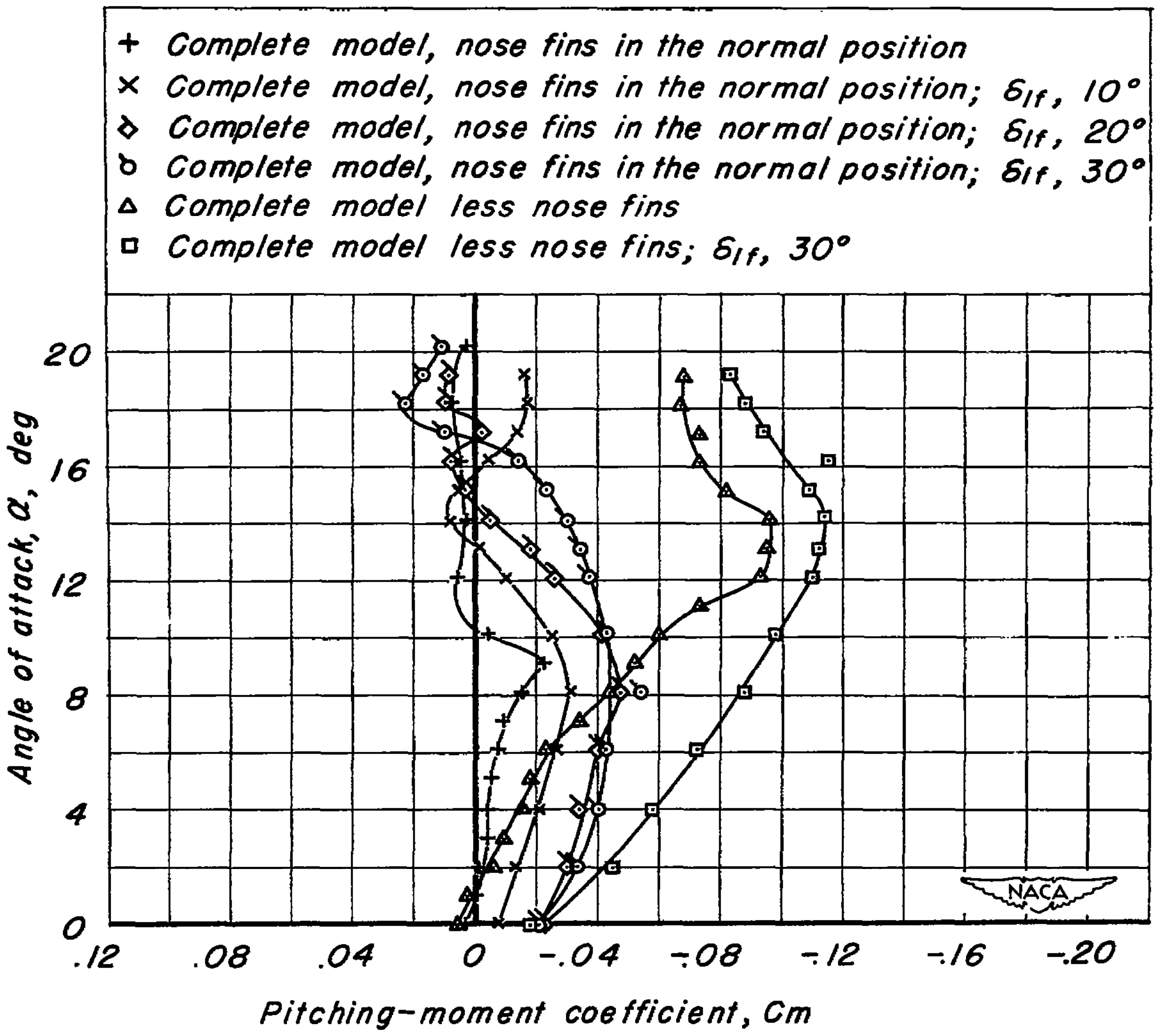

(a) Mach number, 0.40.

Figure 29.- The effect of several changes in configuration on the variation of pitching-moment coefficient with angle of attack for the MX-656 model.

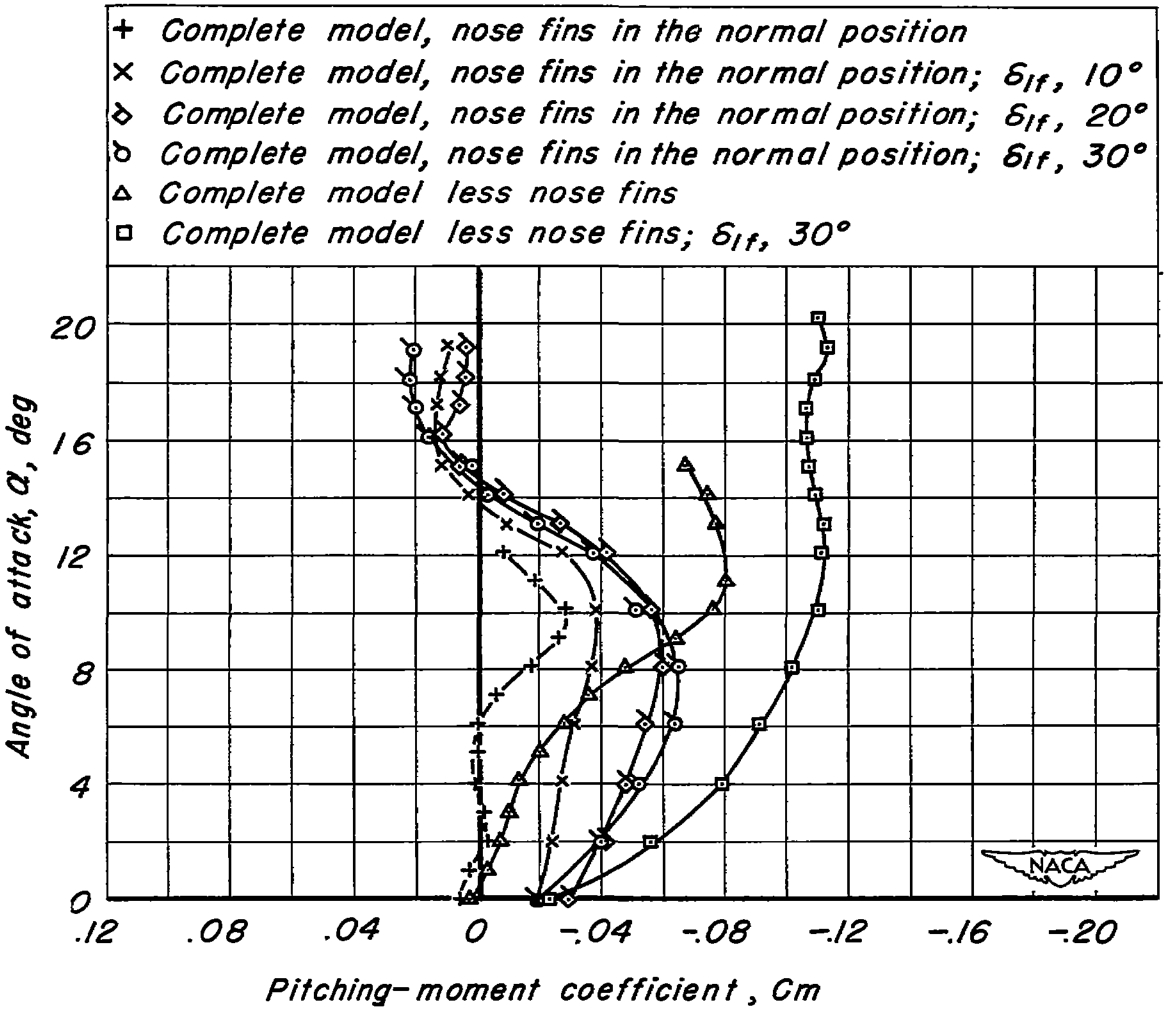

(b) Mach number, 0.80.

Figure 29.– Continued.

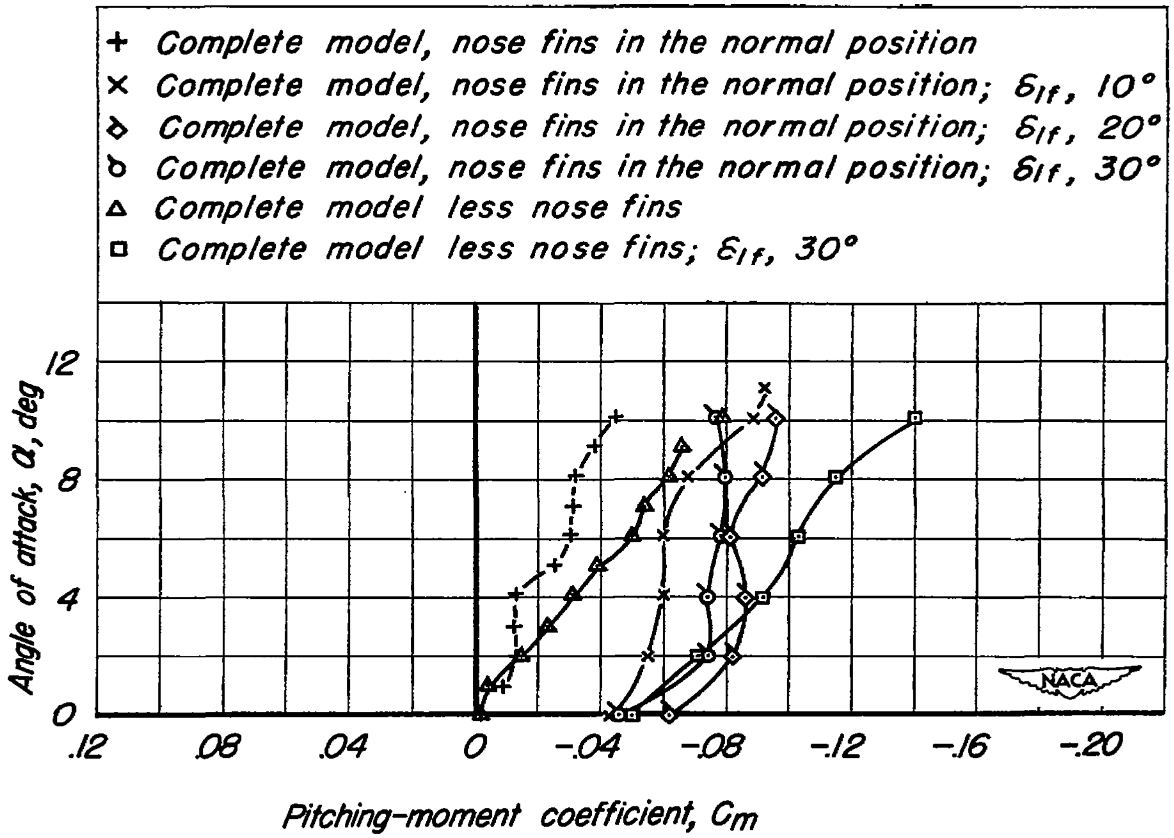

(c) Mach number, 0.90.

Figure 29.– Concluded.

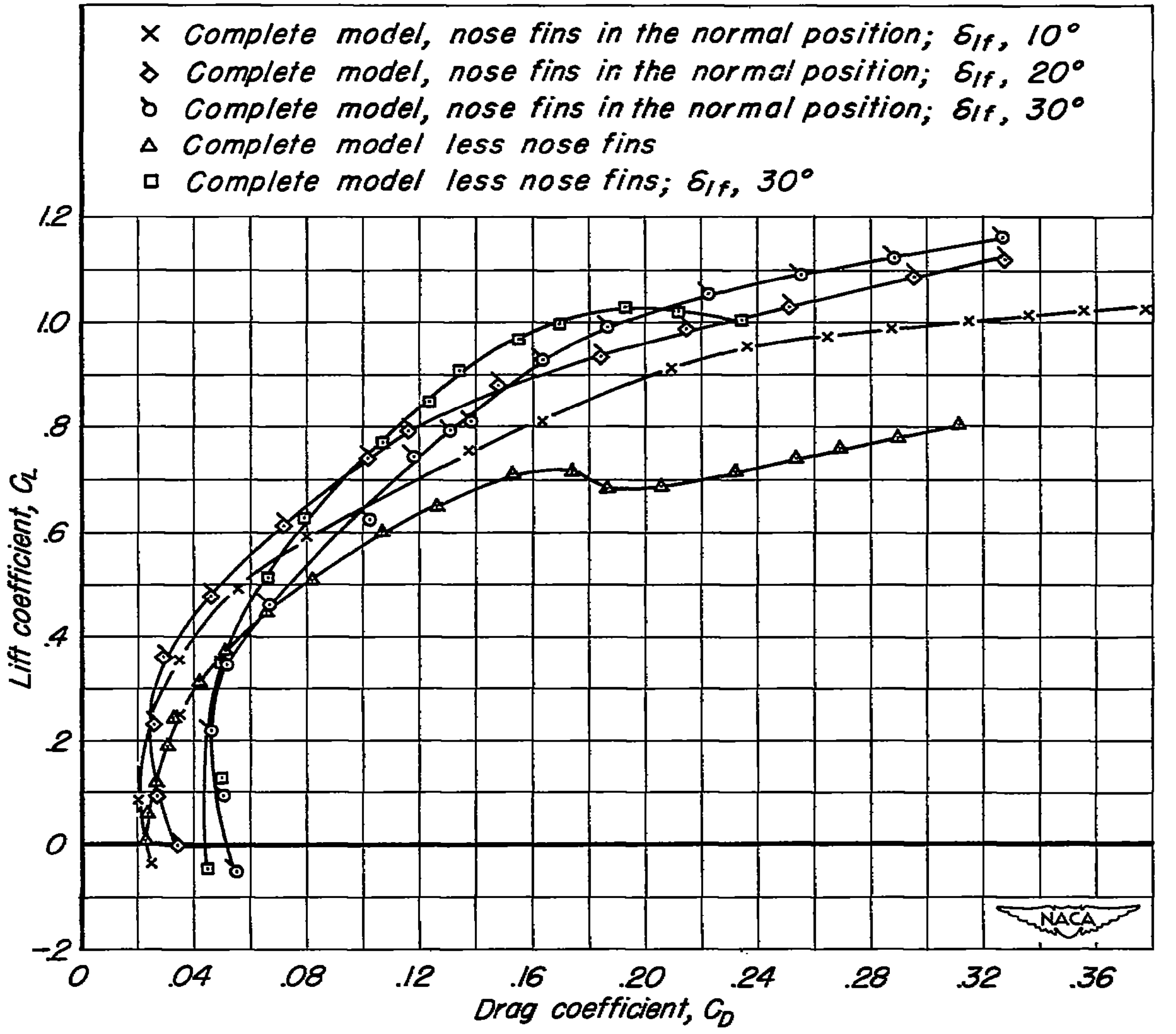

(a) Mach number, 0.40.

Figure 30.– The effect of several changes in configuration on the variation of drag coefficient with lift coefficient for the MX-656 model.

[redacted]

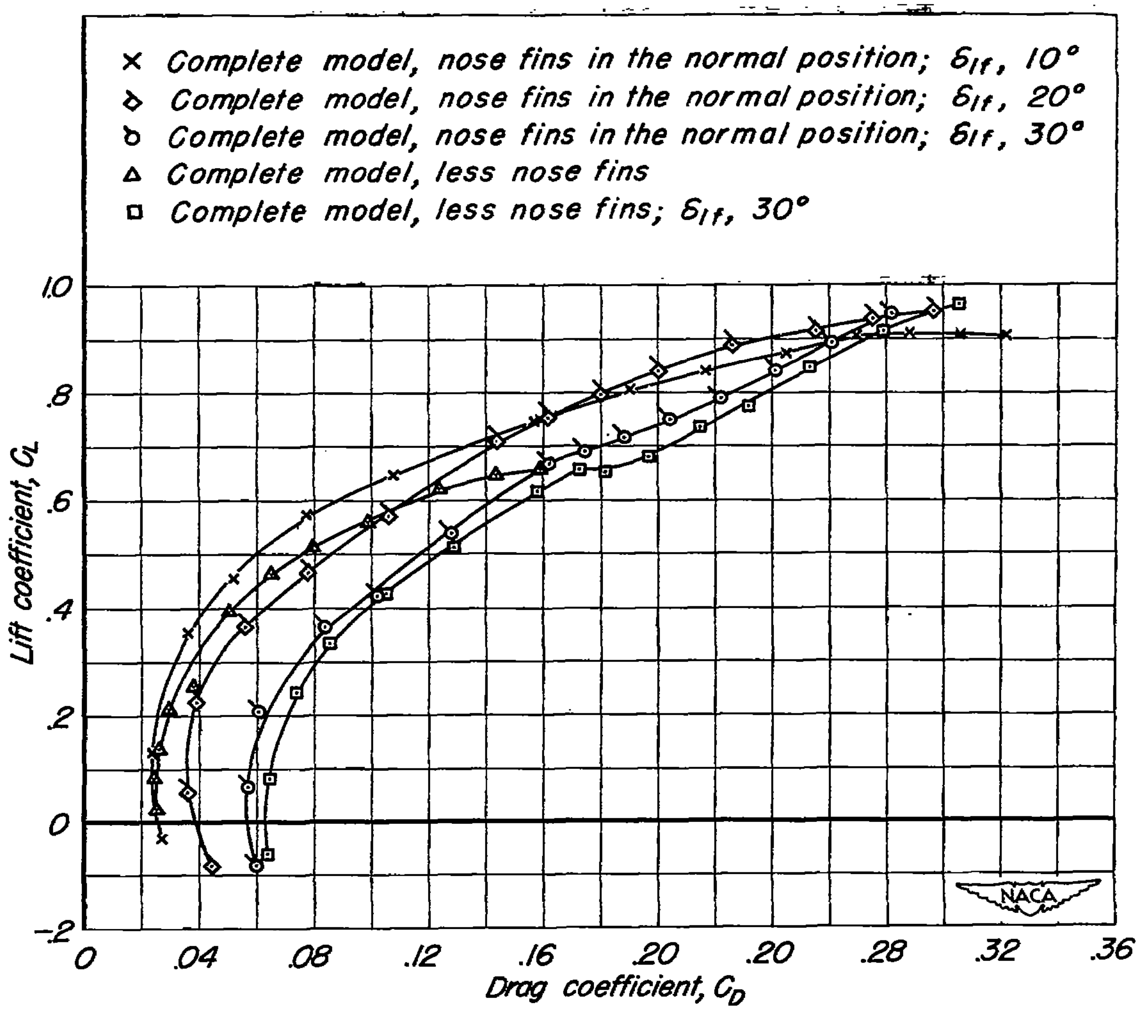

(b) Mach number, 0.80.

Figure 30.–Continued.

[redacted]

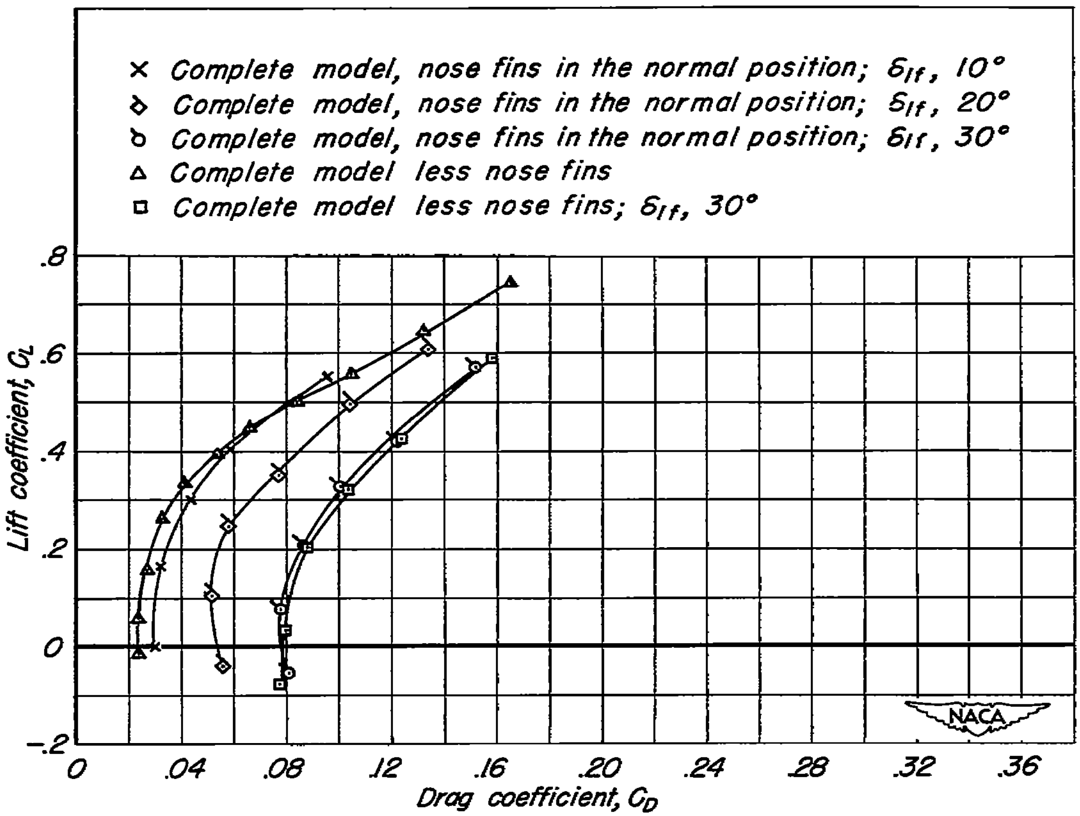

(c) Mach number, 0.90.

Figure 30.- Concluded.

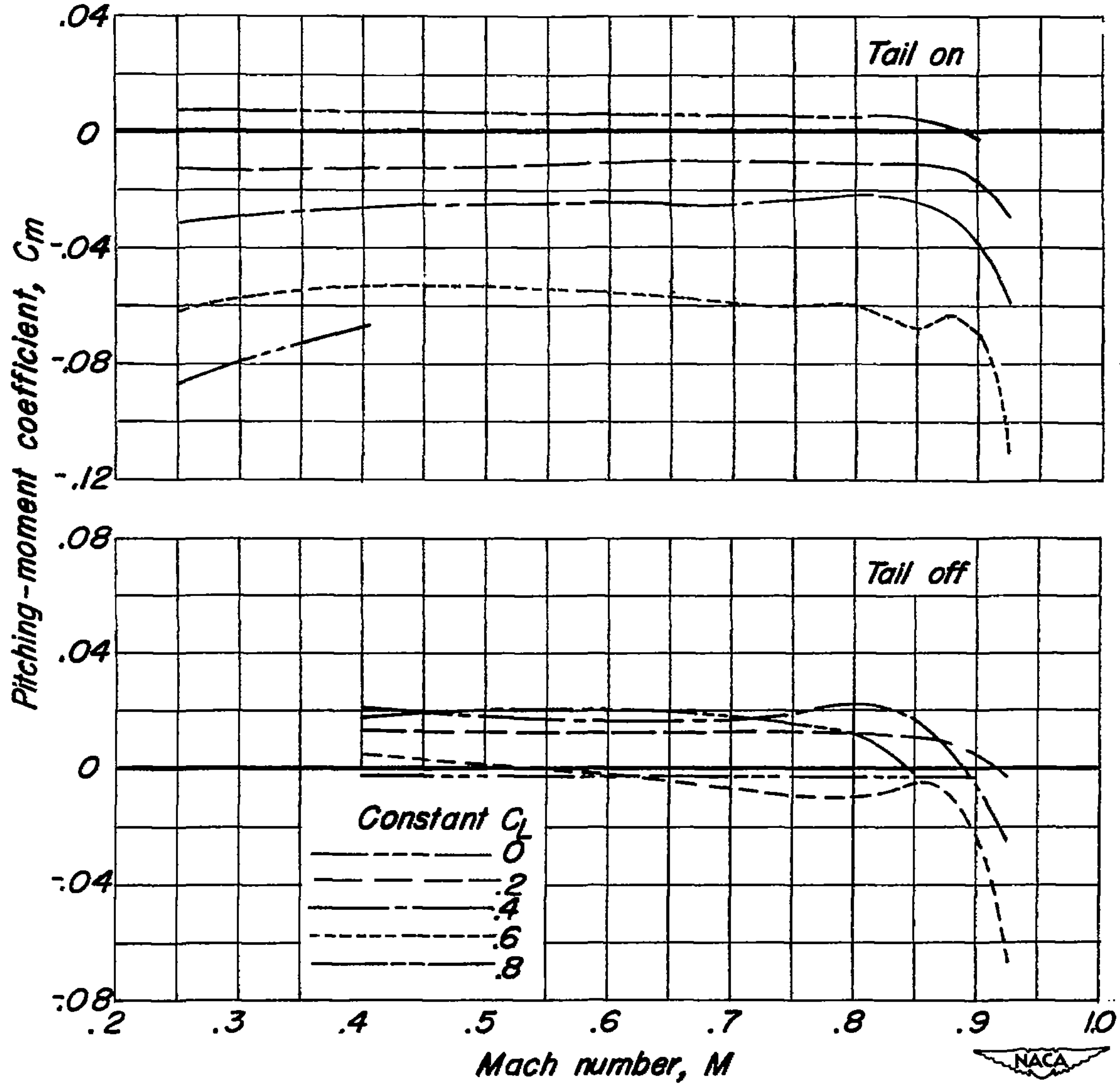

Figure 31.– The variation of pitching-moment coefficient with Mach number for the MX-656 model without the nose fins.

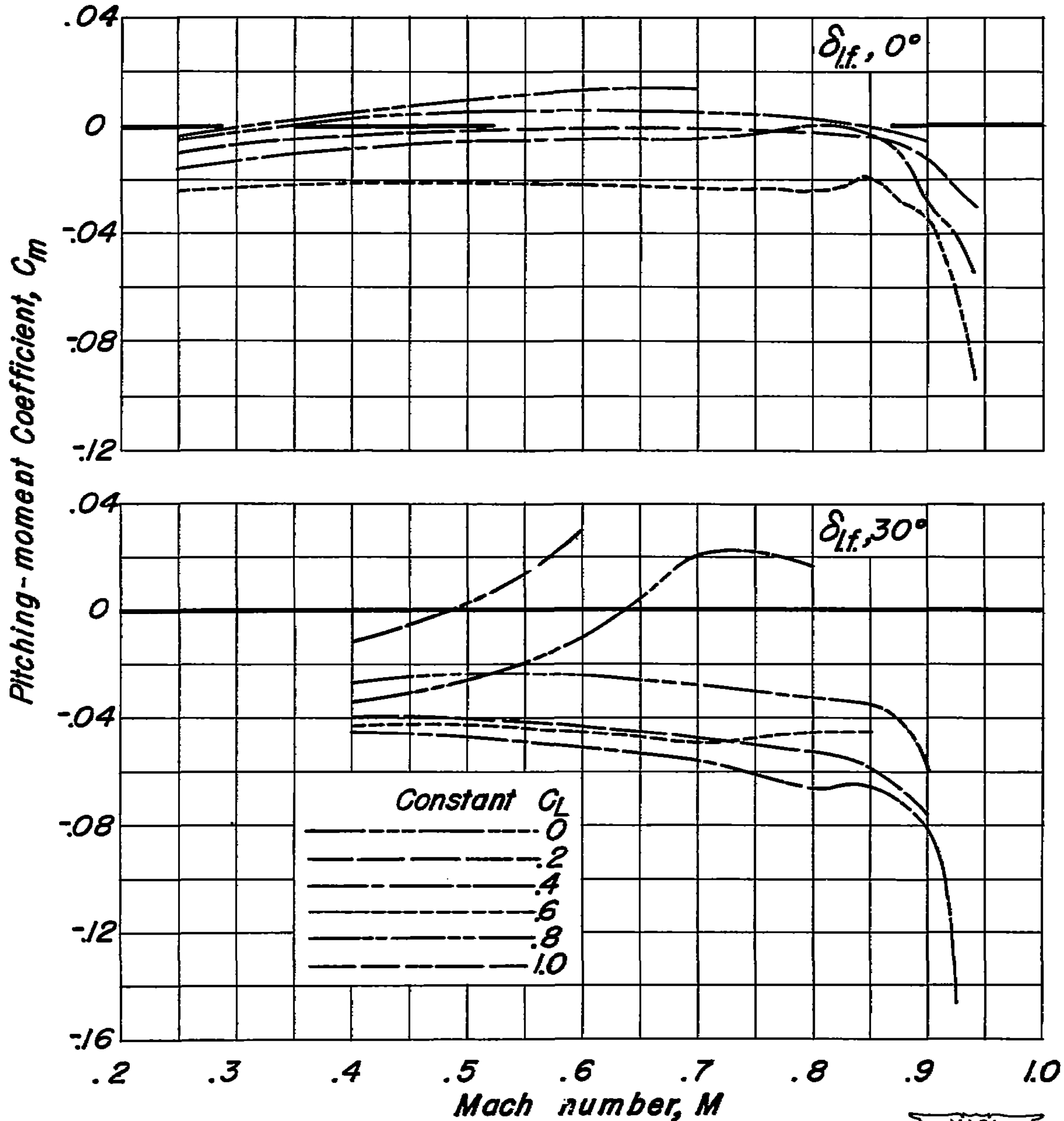

Figure 32.– The variation of pitching-moment coefficient with Mach number for the MX-656 model with the nose fins in the normal position.

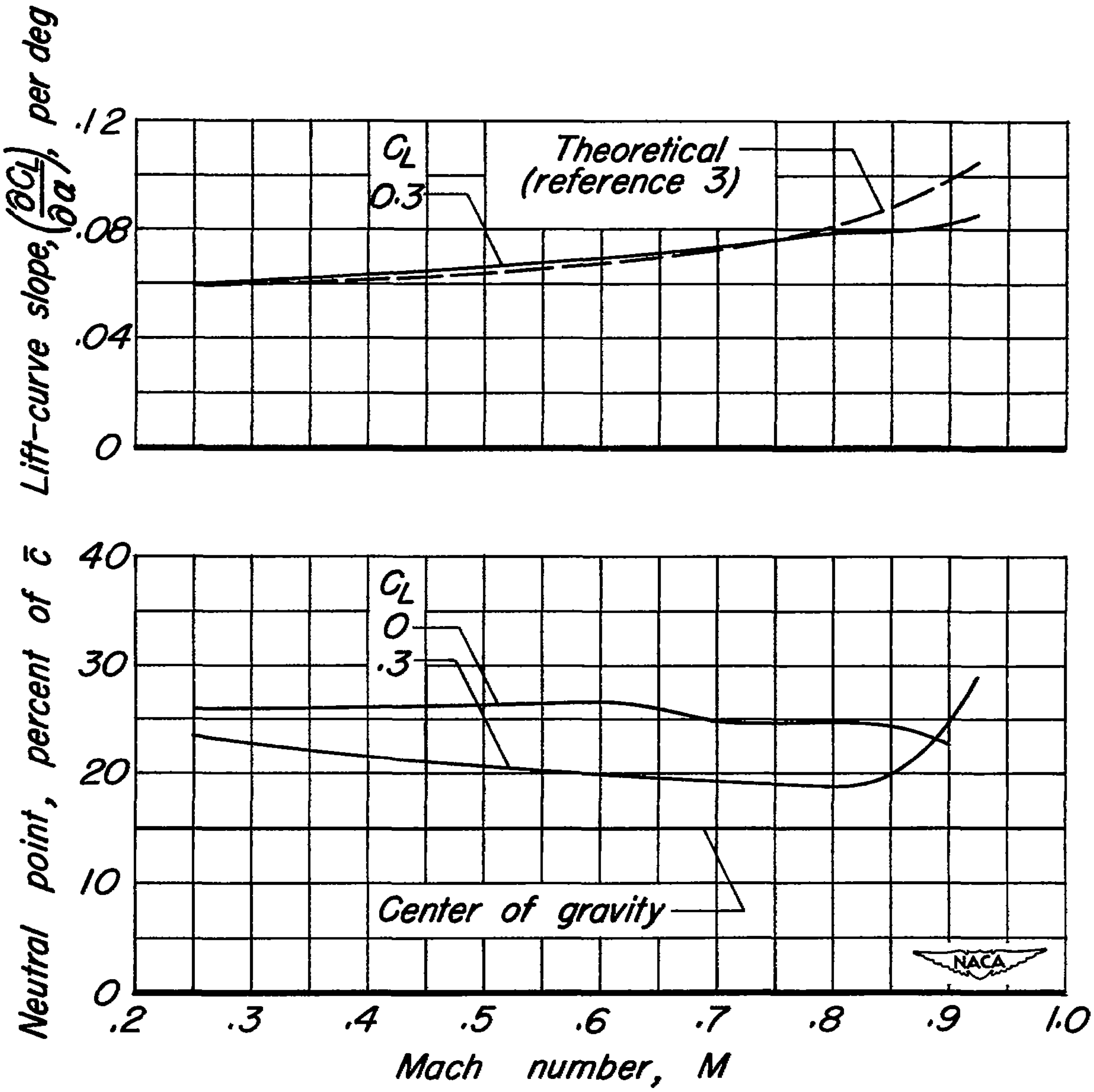

Figure 33.–The variation of lift-curve slope and neutral point with Mach number for the MX-656 model without the nose fins.

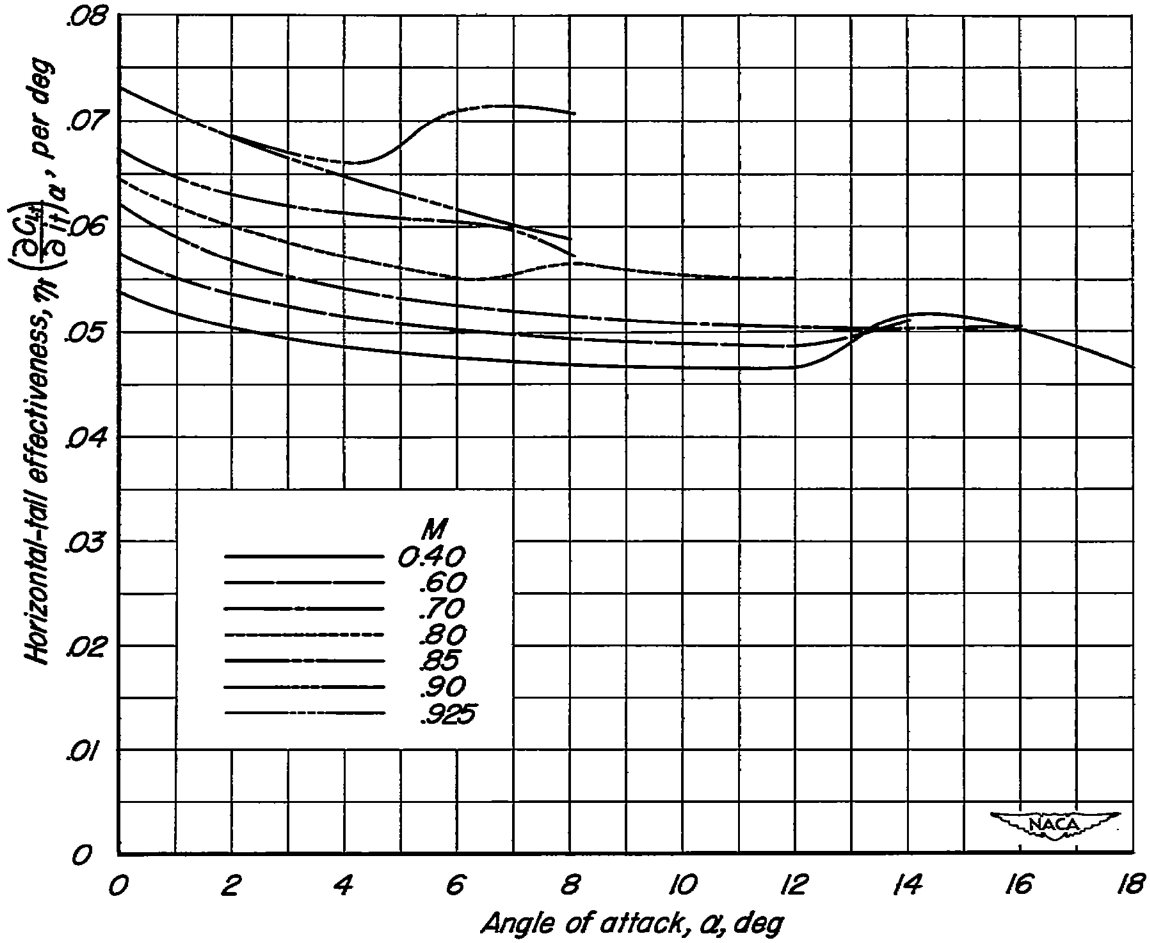

Figure 34.– The variation of horizontal-tail effectiveness with angle of attack for the MX-656 model with the nose fins in the normal position.

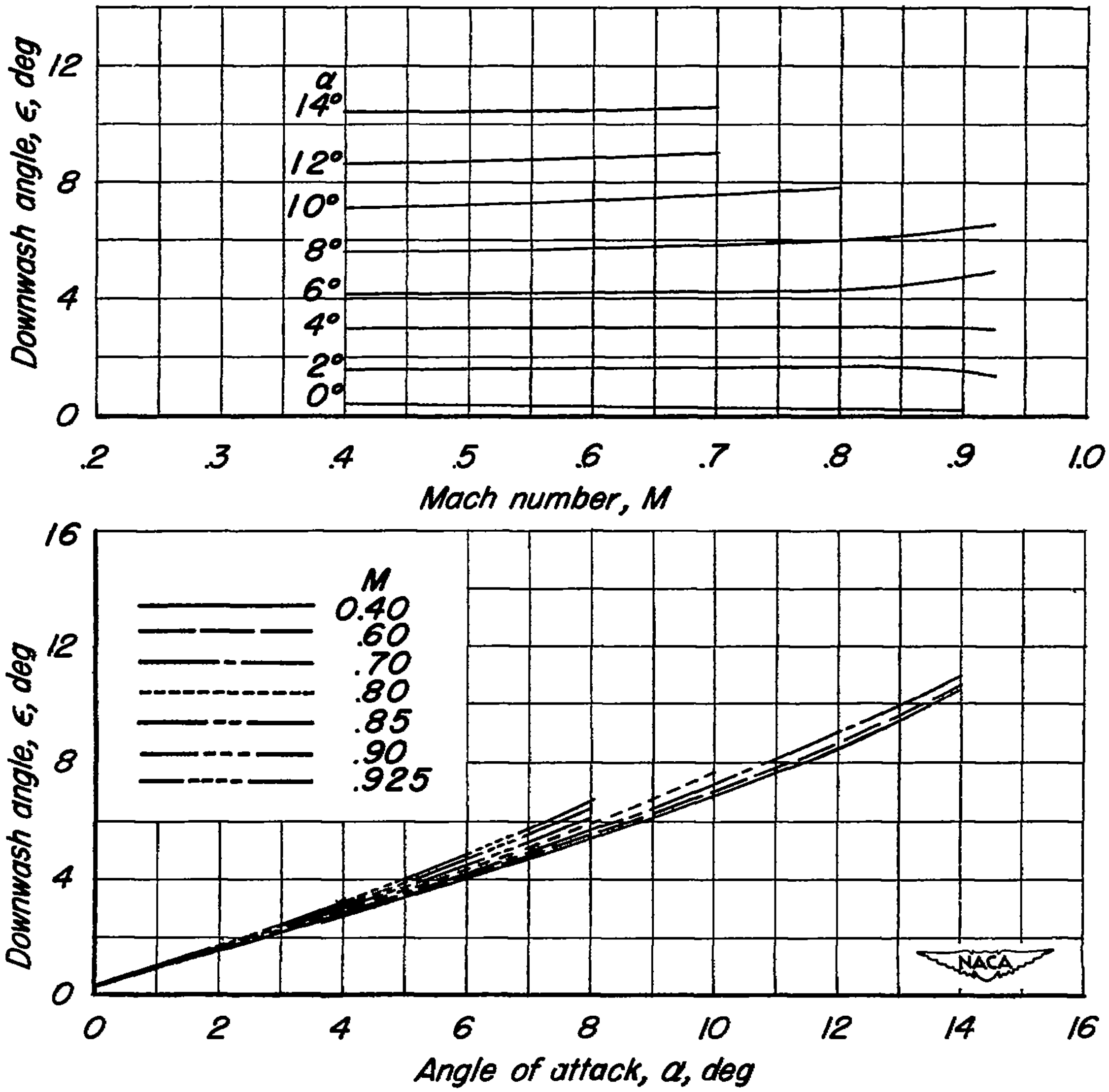

Figure 35.- The variation of the calculated downwash angle at the tail with Mach number and angle of attack for the MX-656 model without the nose fins.

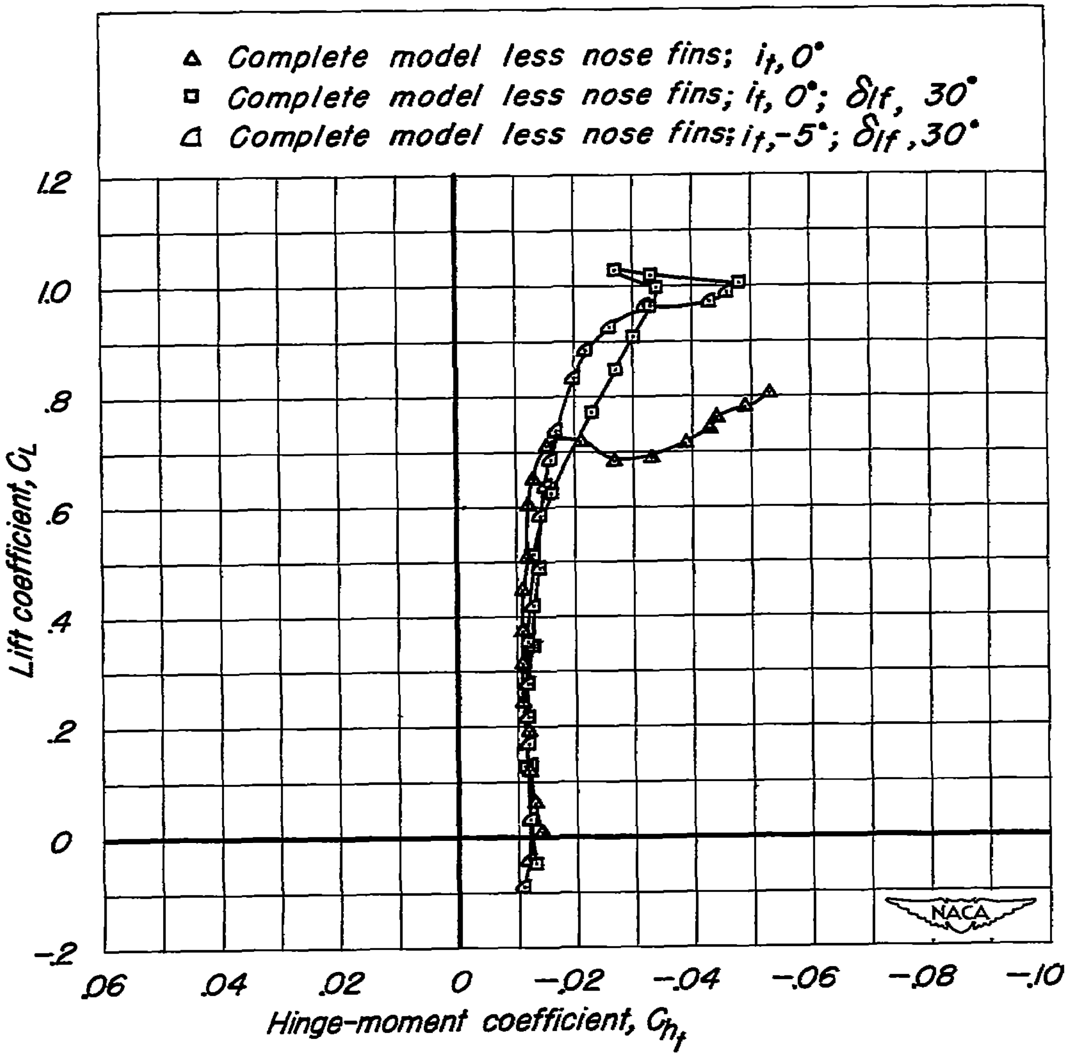

(a) Mach number, 0.40.

Figure 36.- The variation of horizontal-tail hinge-moment coefficient with lift coefficient for the MX-656 model without the nose fins.

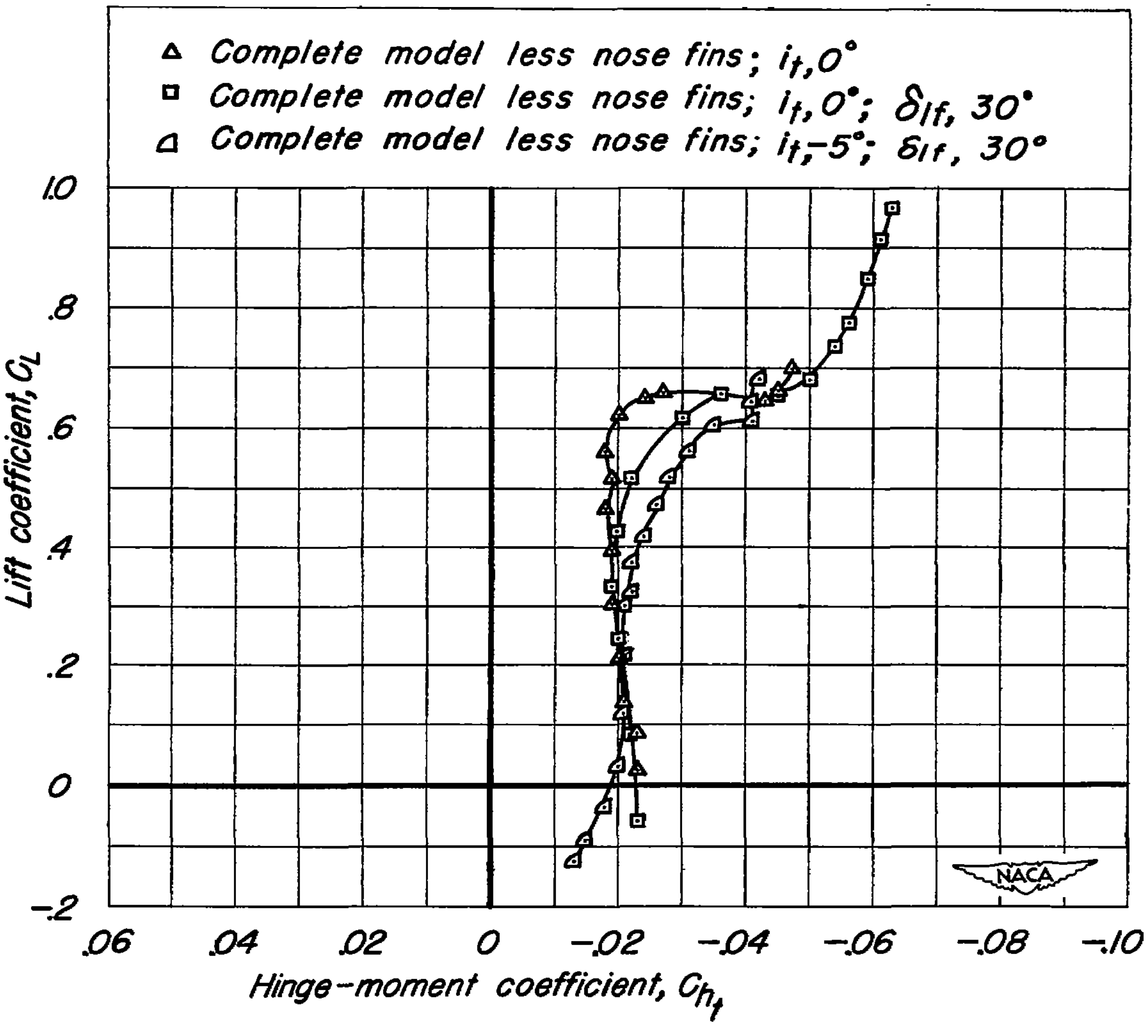

(b) Mach number, 0.80.

Figure 36.-Continued.

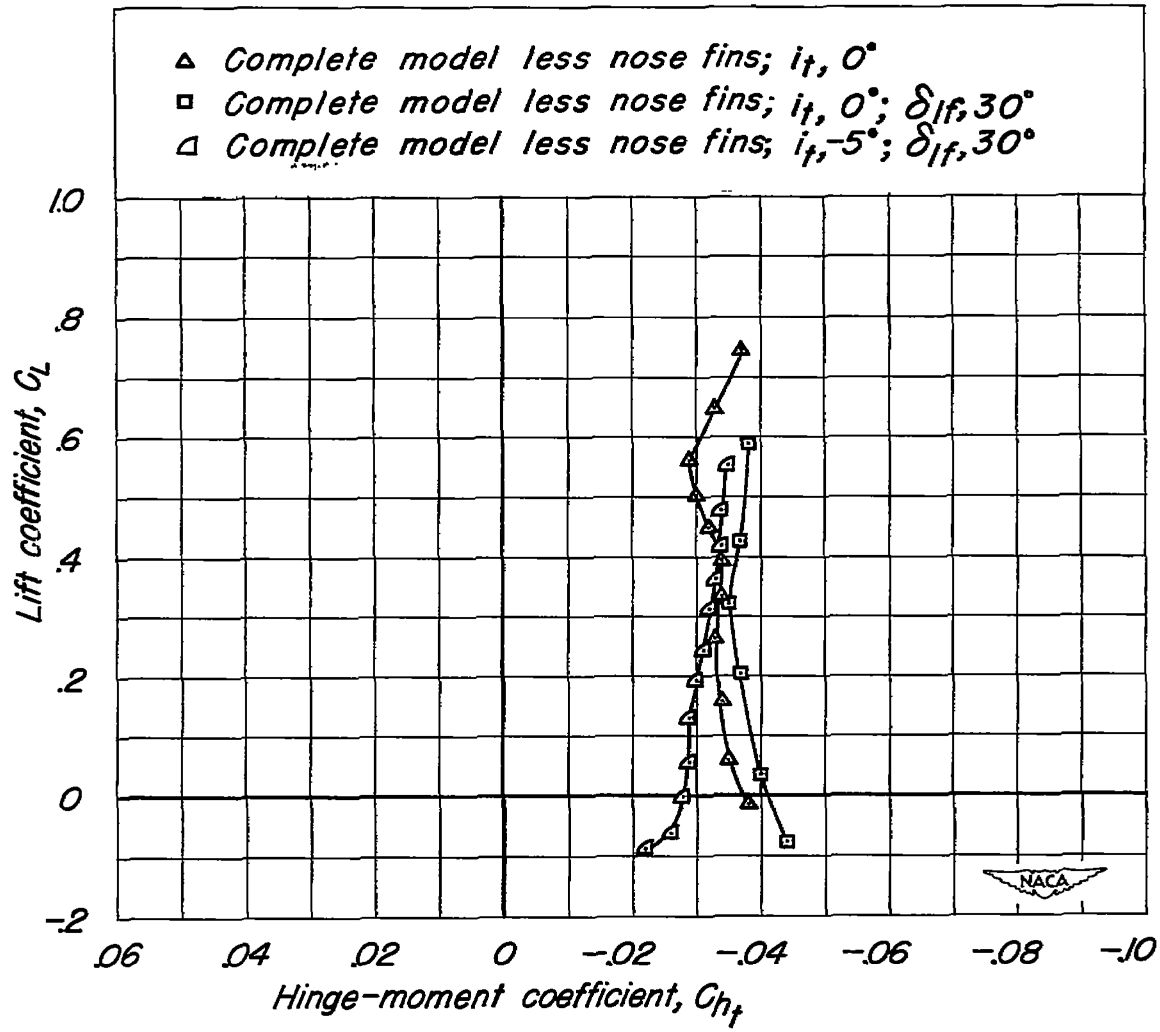

(c) Mach number, 0.90.

Figure 36.- Concluded.

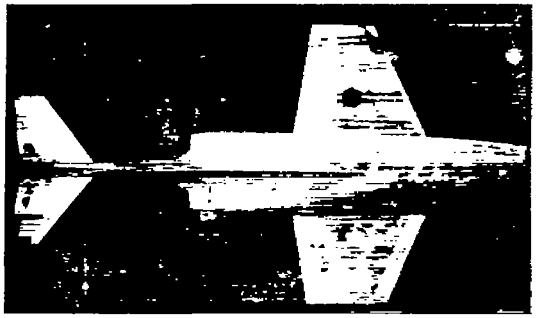

α, 0°

α, 3°

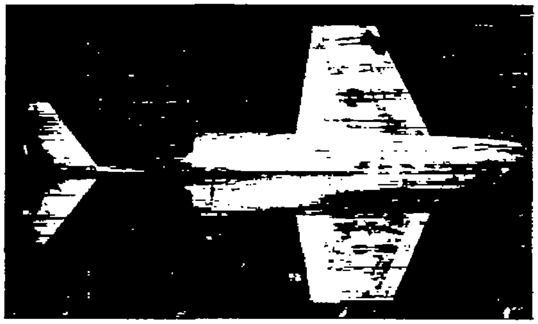

α, 4°

α, 5°

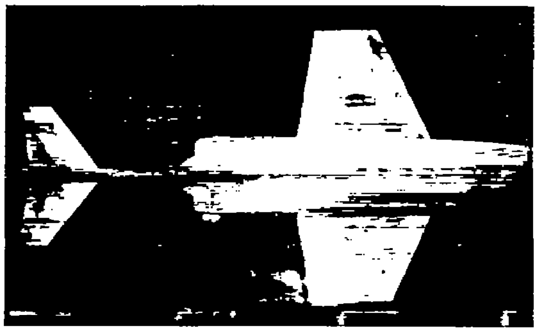

α, 6°

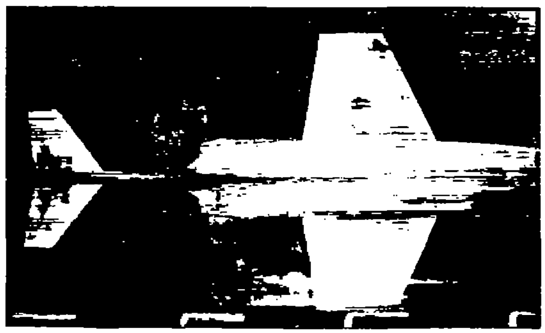

α, 7°

(a) Angles of attack, 0°, 3°, 4°, 5°, 6°, 7°.

NACA
A-13602

Figure 37.– Tufts on the MX-656 model without the nose fins at 0.40 Mach number and 0° yaw.

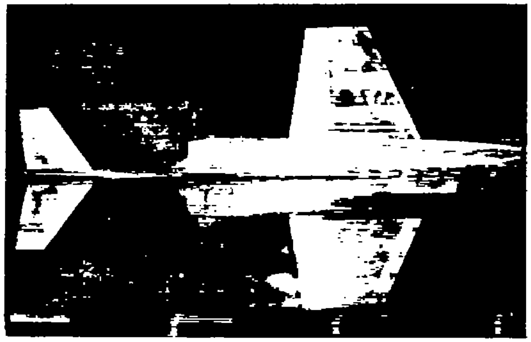

α, 8°

α, 9°

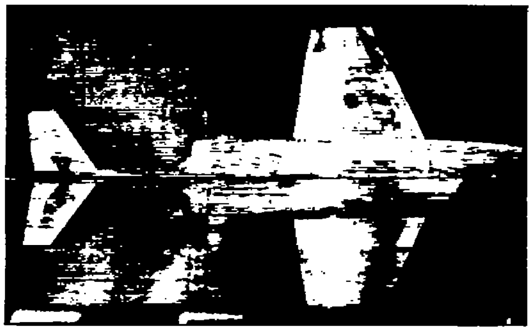

α, 12°

α, 15°

NACA
A-13603

(b) Angles of attack, 8°, 9°, 12°, 15°.

Figure 37.— Concluded.

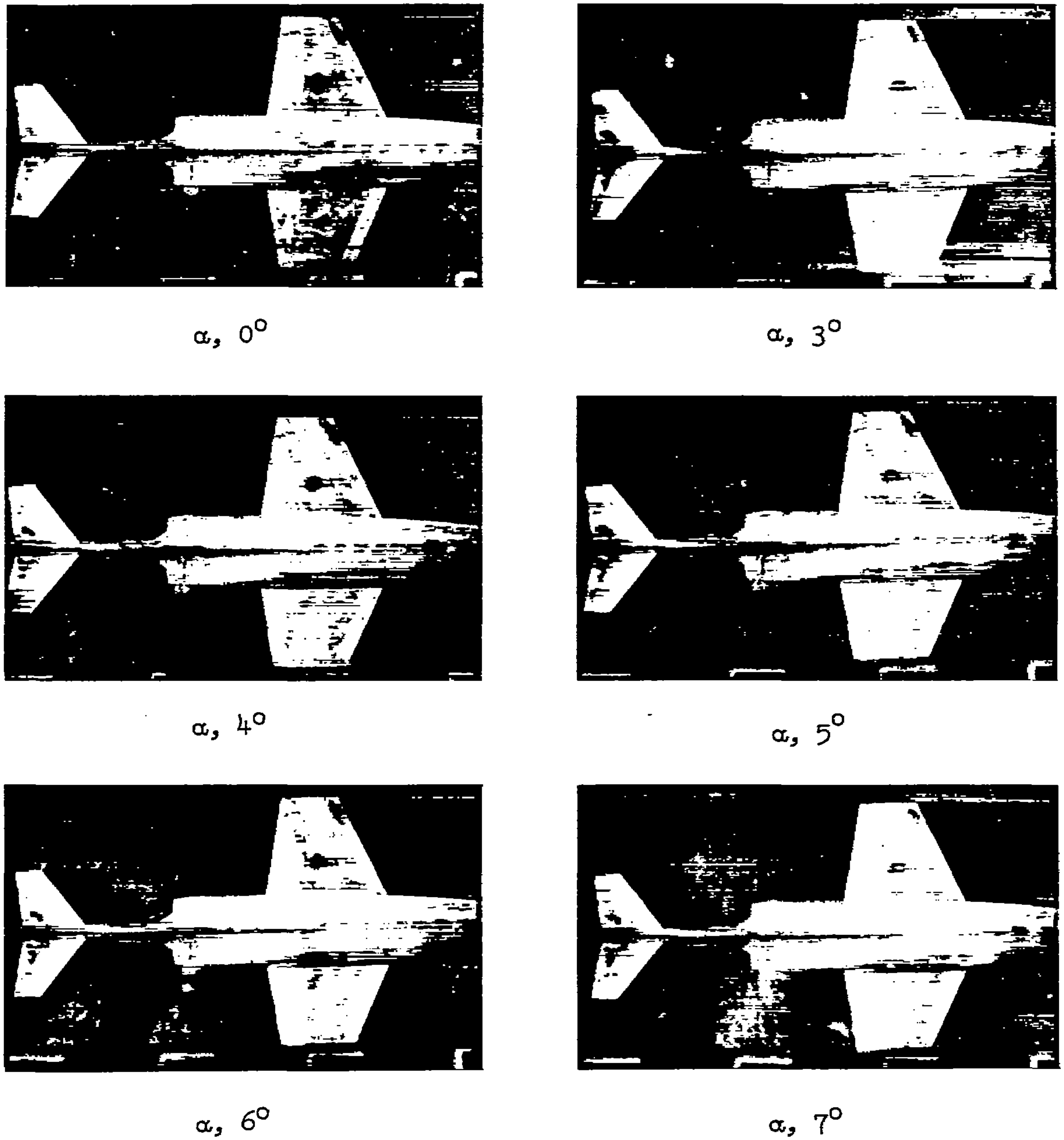

(a) Angles of attack, 0°, 3°, 4°, 5°, 6°, 7°.

NACA
A-13604

Figure 38.– Tufts on the MX-656 model without the nose fins at 0.80 Mach number and 0° yaw.

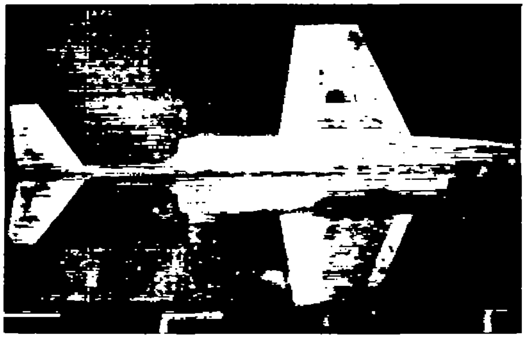

α, 8°

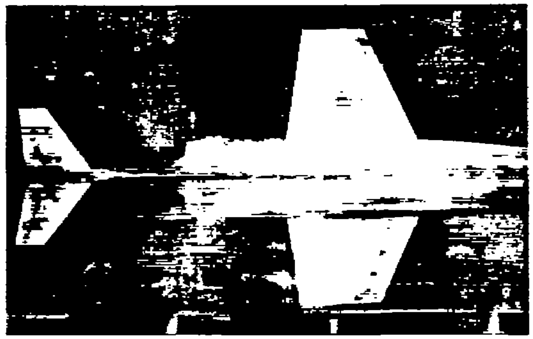

α, 9°

α, 12°

(b) Angles of attack, 8°, 9°, 12°.

A-13605

Figure 38.– Concluded.

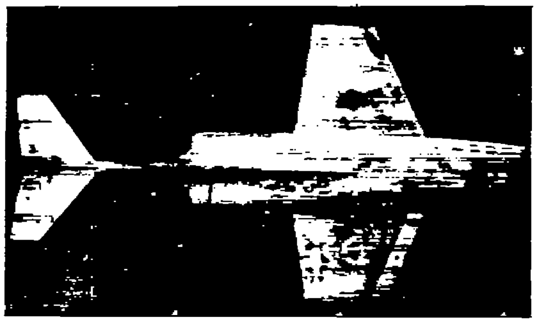

α, 0°

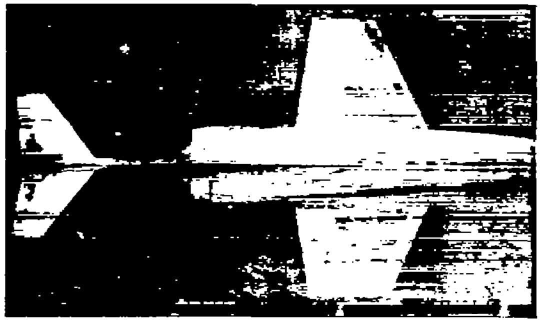

α, 2°

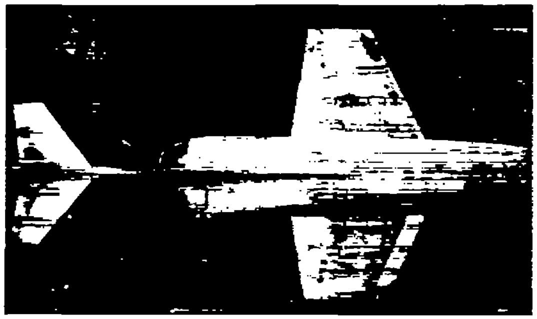

α, 4°

α, 6°

α, 8°

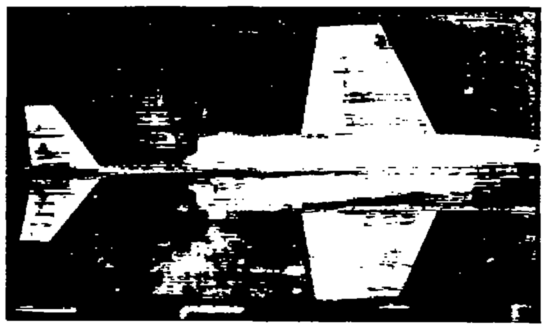

α, 9°

A-13606

Figure 39.– Tufts on the MX-656 model without the nose fins at 0.90 Mach number and 0° yaw.

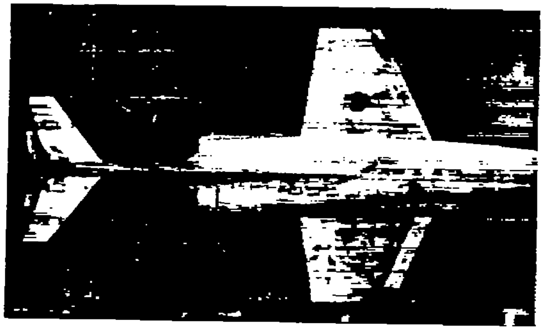

α, 0°

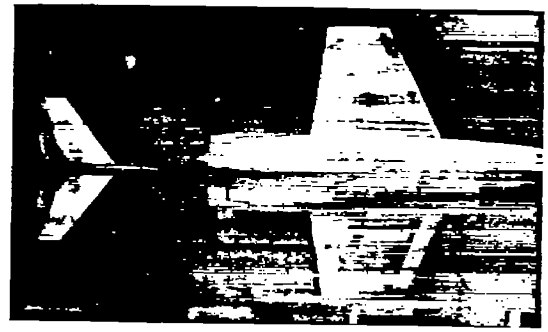

α, 2°

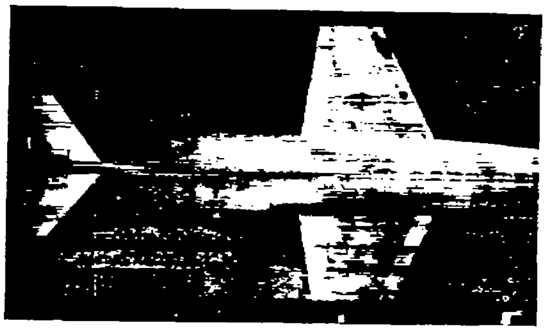

α, 4°

α, 6°

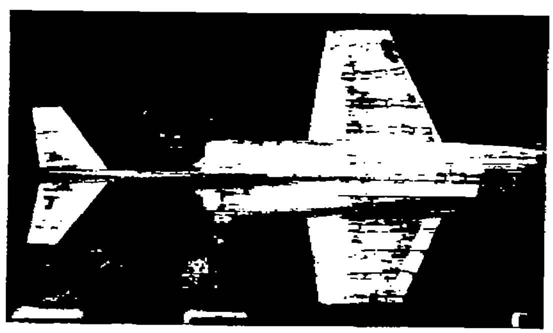

α, 8°

NACA
A-13607

Figure 40.– Tufts on the MX-656 model without the nose fins at 0.925 Mach number and 0° yaw.

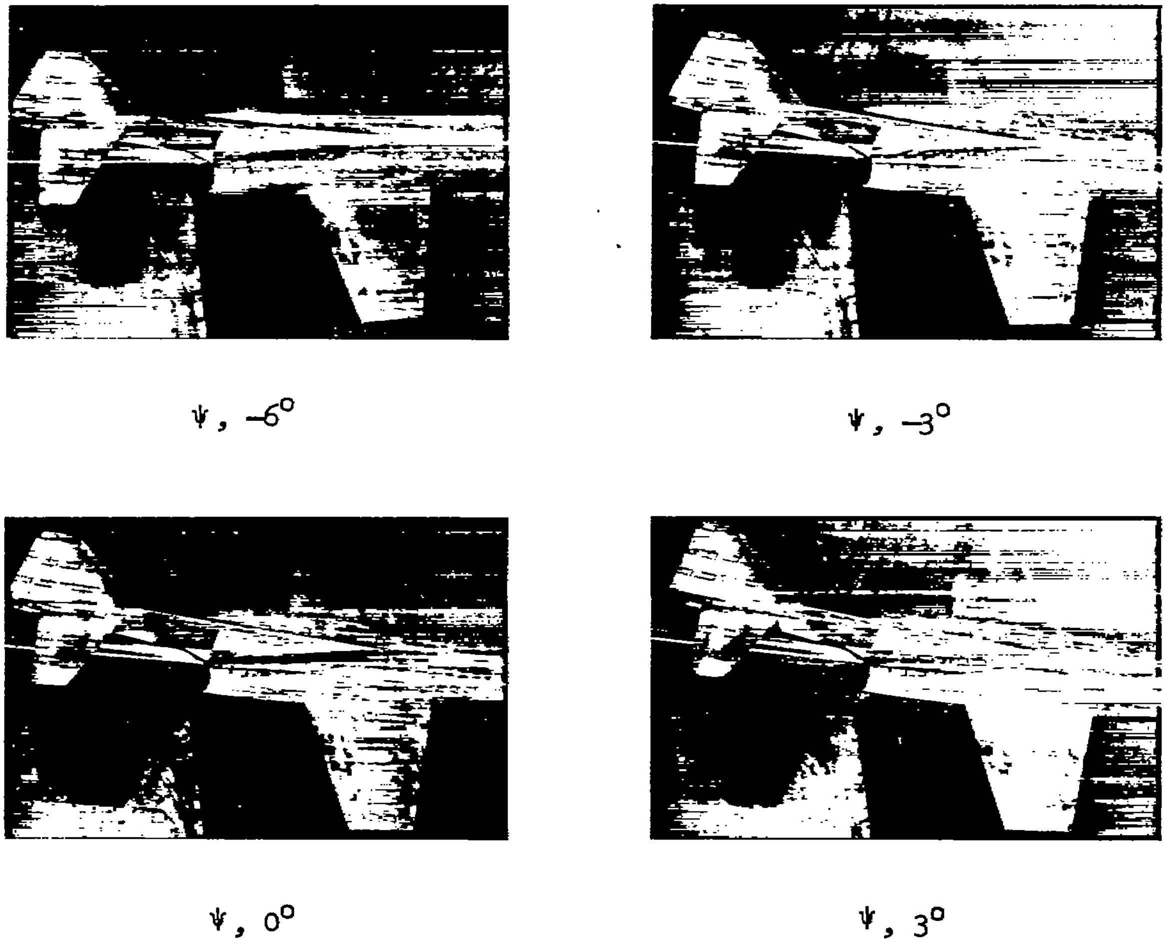

NACA
A-13608

(a) Angles of yaw, −6°, −3°, 0°, 3°.

Figure 41.– Tufts on the MX-656 model without the nose fins at 0.40 Mach number and 6.2° angle of attack.

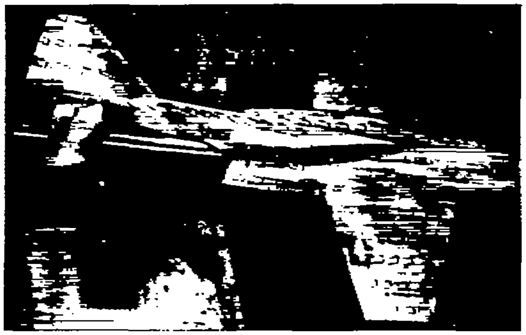

ψ, 6°

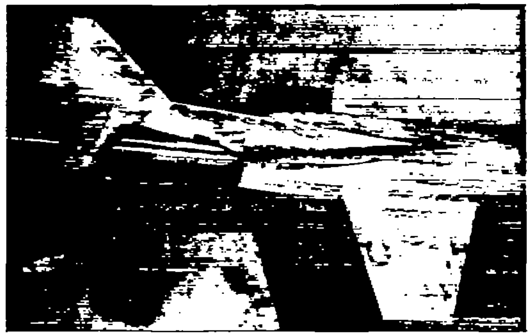

ψ, 9°

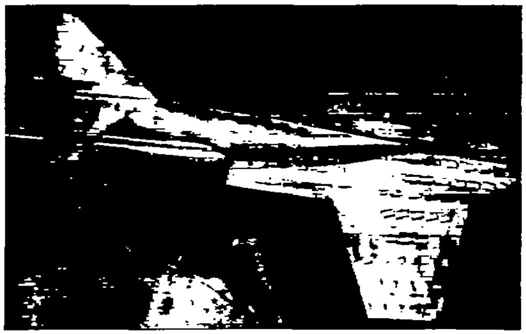

ψ, 12°

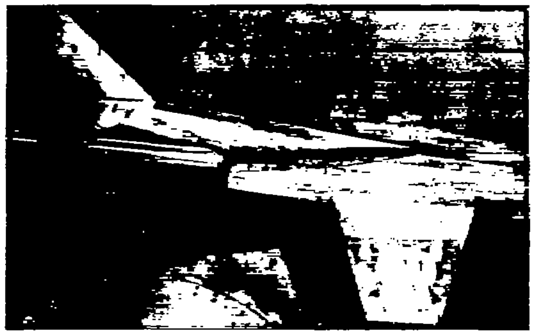

ψ, 15°

NACA
A-13609

(b) Angles of yaw, 6°, 9°, 12°, 15°.

Figure 41.– Concluded.

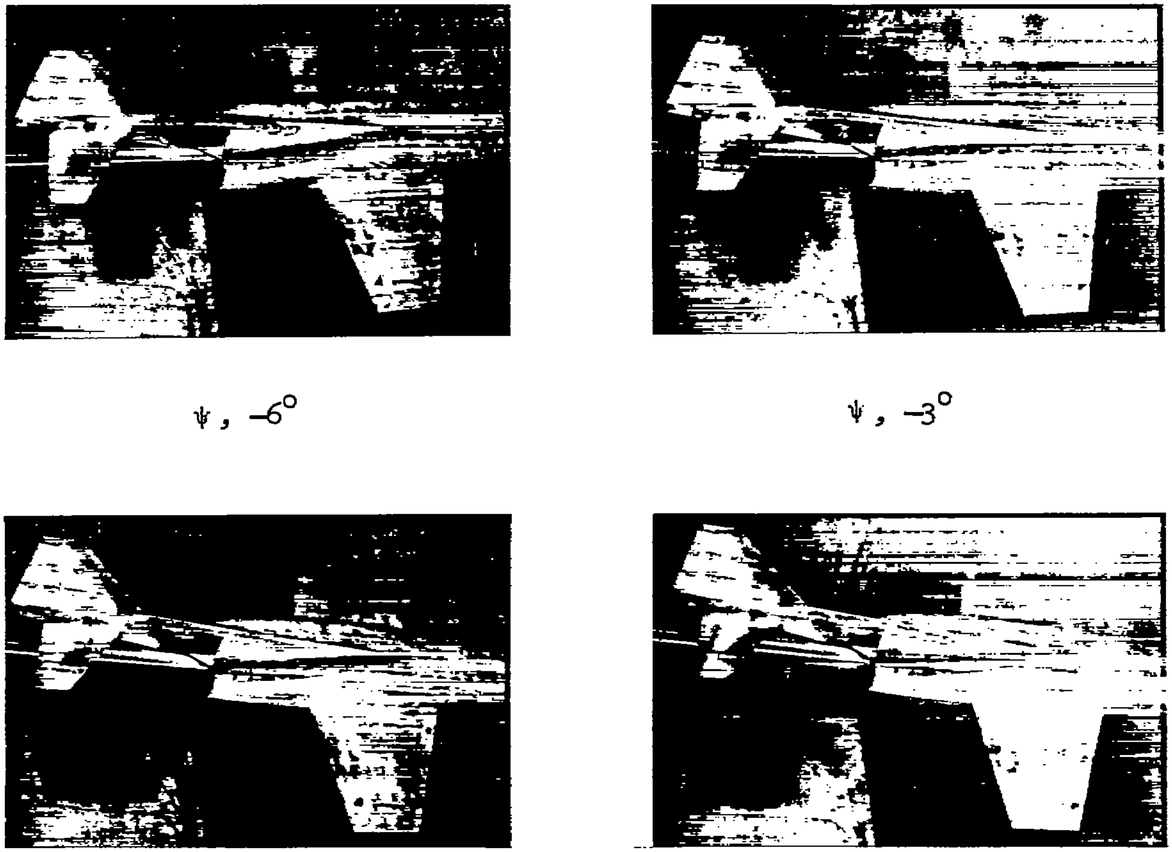

ψ, −6°   ψ, −3°

ψ, 0°   ψ, 3°

NACA
A-13610

(a) Angles of yaw, −6°, −3°, 0°, 3°.

Figure 42.– Tufts on the MX-656 model without the nose fins at 0.80 Mach number and 6.2° angle of attack.

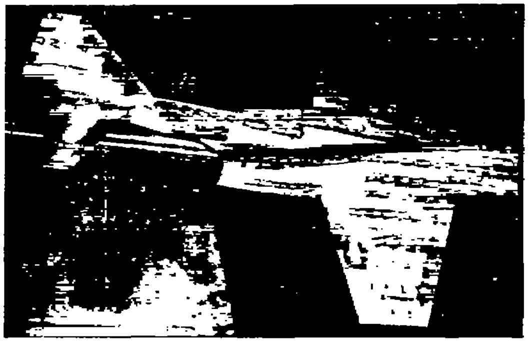

ψ, 6°

ψ, 9°

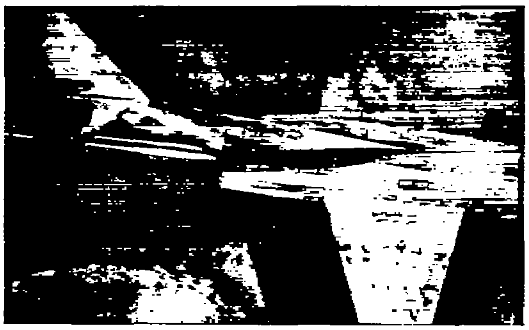

ψ, 12°

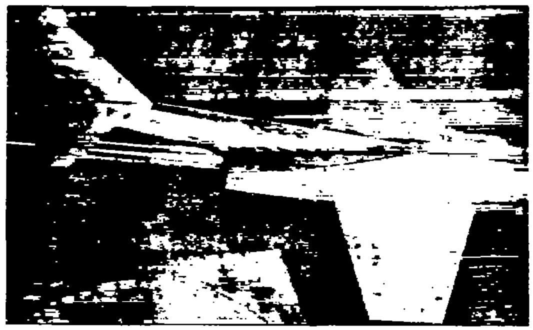

ψ, 15°

NACA
A-13611

(b) Angles of yaw, 6°, 9°, 12°, 15°.

Figure 42.– Concluded.

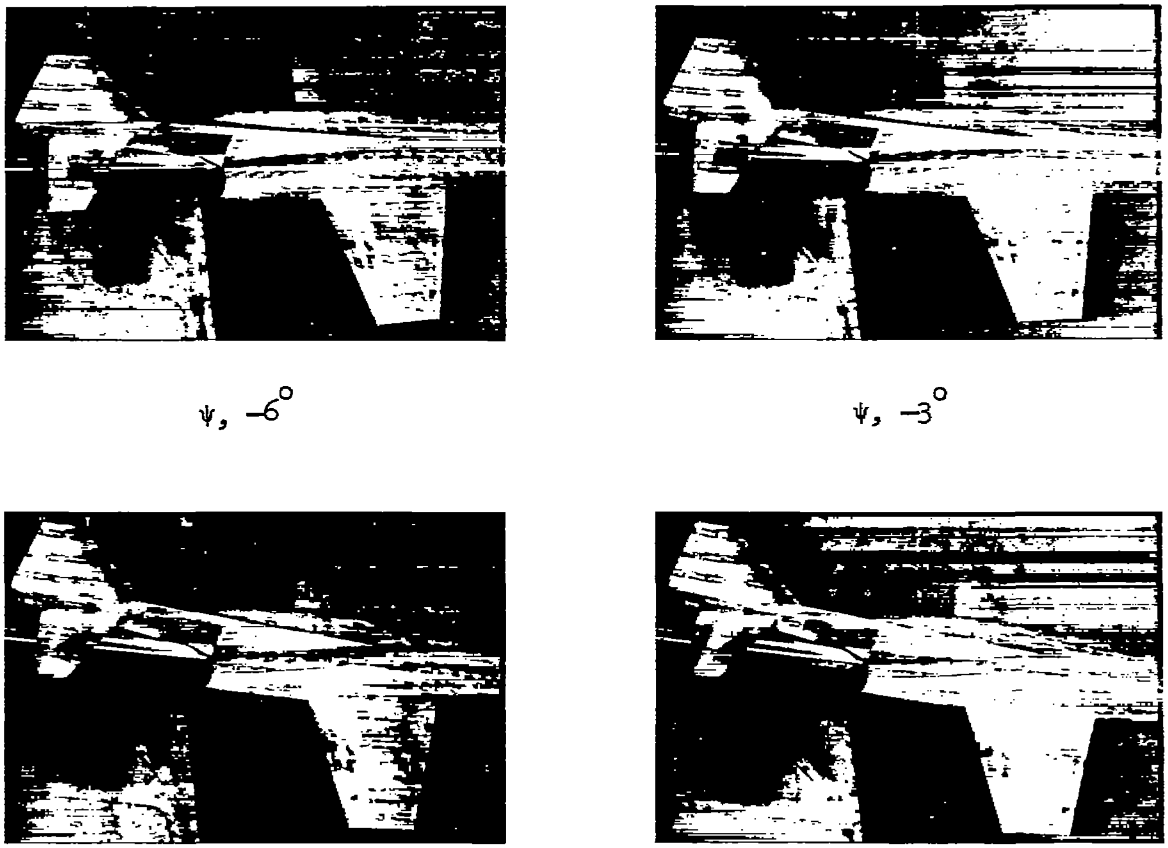

ψ, -6° ψ, -3°

ψ, 0° ψ, 3°

NACA
A-13612

(a) Angles of yaw, -6°, -3°, 0°, 3°.

Figure 43.— Tufts on the MX-656 model without the nose fins at 0.90 Mach number and 6.2° angle of attack.

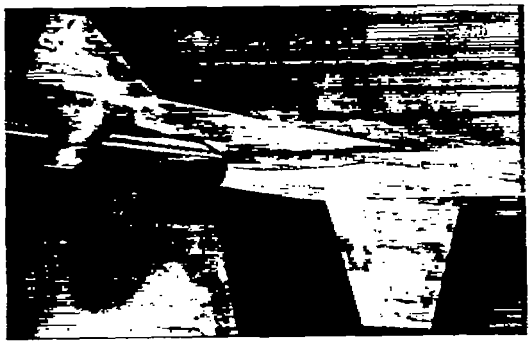

ψ, 6°

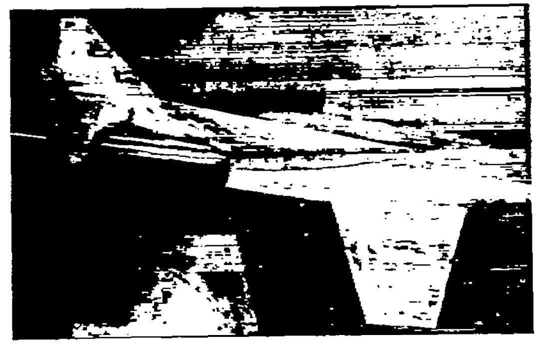

ψ, 9°

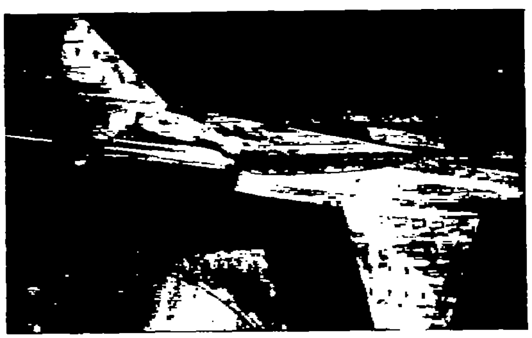

ψ, 12°

ψ, 15°

NACA
A-13613

(b) Angles of yaw, 6°, 9°, 12°, 15°.

Figure 43.— Concluded.

NACA - Langley Field, Va.